NORTHWESTERN UNIVERSITY

# Phase-Field Crystal Model Development

A DISSERTATION

SUBMITTED TO THE GRADUATE SCHOOL

IN PARTIAL FULFILLMENT OF THE REQUIREMENTS

for the degree

DOCTOR OF PHILOSOPHY

Field of Chemical and Biological Engineering

By

Eli Alster

EVANSTON, ILLINOIS

September 2018

# ABSTRACT

Phase-Field Crystal Model Development

Eli Alster

The phase-field crystal (PFC) model is an exciting new method for simulating crystalline materials with atomic resolution over diffusional time scales. Unfortunately, applications of the model have been severely limited by the requirement that novel free energies must be constructed for each new material of interest. This thesis describes three different methods by which the basic PFC model has been extended to simulate additional materials and also demonstrates that these new models capture some of the physics of real materials.

The first extension is the development of a PFC model for a multicomponent ordered crystal. As a test case, a generic B2 compound is investigated. This model produces a line of either first-order or second-order order-disorder phase transitions, depending on parameters. This B2 model is then used to study antiphase boundaries (APBs), which are shown to reproduce classical mean field behavior. Lastly, we found through dynamical simulations of ordering across small-angle grain boundaries that the model predicts that dislocation cores pin the evolution of APBs.

The second extension is a method that, utilizing a numerically tractable three-point correlation function, creates an array of new complex three- and two-dimensional crystal structures. The three-point correlation function is designed in order to energetically favor the principal interplanar angles of a target crystal structure. This is achieved via an analysis performed by examining the crystal's structure factor. This approach successfully yields energetically stable simple cubic, diamond cubic, simple hexagonal, graphene layers, and $CaF_2$ crystals. To illustrate the ability of the method to yield a particularly complex and technologically important crystal structure, this three-point correlation function method is used to generate perovskite crystals.

The last extension is for a two-component PFC model that undergoes displacive phase transitions. When the intercomponent free energy in the model is a simple polynomial, the crystal undergoes displacive transitions in $\langle 10 \rangle$ and $\langle 11 \rangle$ directions. When the interaction is a correlation function however, displacements in any direction can occur. This displacive phase-field crystal (DPFC) model also maps to Landau-Ginzburg-Devonshire (LGD) theories for ferroelectrics, and the DPFC and LGD models are compared in terms of phase transitions and domain walls. The DPFC model also displays stable quadrijunctions and pinning of domain wall evolution by dislocation cores.

## Acknowledgements

I owe the completion of my PhD to many individuals. Foremost, I would like to thank Peter Voorhees, for his support, kindness, and assistance throughout my years at Northwestern. I am fortunate to have you as an advisor. I also want to express enormous gratitude to Ken Elder, not only for sharing his thoughts and insights that were instrumental to much of my research, but also for his continual friendliness.

Additional thanks to Kevin McReynolds for introducing me to the PFC model, and Zhi-Feng Huang, Nana Ofori-Opuku, Katsuyo Thornton, David Montiel, Jeffrey Hoyt, Boaz Haberman, Edwin Schwalbach, Jason Luce, and all the members of the Voorhees Group for answering my random questions. I would also like to thank Randall Snurr and Monica Olvera de la Cruz for serving on my committee. This work was supported by a NSF Graduate Research Fellowship and NSF DMR-3003700315.

# Table of Contents

# List of Tables

# List of Figures

CHAPTER 1

# Introduction

A fundamental problem in science is understanding multiscale phenomena. As a result of decades of research, molecular dynamics (MD) is now powerful enough to accurately predict the structure of quickly folding proteins [**2**] and the faceting of asymmetrical grain boundaries [**3**] with atomic resolution. However, MD is fundamentally constrained by the fastest vibrational frequency of the system, so time scales beyond a microsecond are normally inaccessible. Unfortunately, most interesting phenomena in materials science take longer than a microsecond.

One method that can simulate longer timescales is the phase-field (PF) method. The PF method postulates that the free energy of the system is a functional of various order parameters, which are statistically averaged over short time and length scales [**4**]. The simplest PF model is the Cahn-Hilliard free energy,

$$F[\phi] = \int_V \left[ f(\phi) + \frac{K}{2} |\nabla \phi|^2 \right] d\boldsymbol{r} \ , \tag{1.1}$$

where $\phi(\boldsymbol{r})$ is an order parameter, $f(\phi)$ is the bulk free energy function, and $K$ is a constant describing the interfacial energy. To go from a static free energy to an equation for evolution dynamics, Fick's First Law is employed for conserved order parameters, namely

$$\boldsymbol{J} = -M\nabla\frac{\delta F}{\delta\phi}, \tag{1.2}$$

where $M$ is the mobility, $\frac{\delta F}{\delta\phi}$ is related to the chemical potential, and $\boldsymbol{J}$ is the flux. Accordingly, Fick's second law is

$$\frac{\partial\phi}{\partial t} = M\nabla^2\frac{\delta F}{\delta\phi}. \tag{1.3}$$

Surprisingly, even this simple free energy makes reasonable predictions for dynamics, at time and length scales inaccessible to MD. Unfortunately, by coarse-graining over short length scales, atomic features such as grain boundaries and dislocation structures are lost.

The phase-field crystal (PFC) method operates in between the regimes of MD and PF. Like traditional PF models, PFC theory involves a free energy functional, and it averages over rapid fluctuations in time to give a time scale of evolution on the order of diffusion rather than atomic vibration. However, unlike traditional PF, the free energy does not average over atomic distances, resulting in pattern formation at equilibrium. The simplest such free energy is

$$F = \int_V \left[\frac{\phi}{2}(-\epsilon + (1+\nabla^2)^2)\phi + \frac{\phi^4}{4}\right] d\boldsymbol{r} \ , \tag{1.4}$$

which is known as the Swift-Hohenberg model [**5**].

Although originally phenomenologically motivated, the Swift-Hohenberg model can been derived from classical density functional theory. Like the PFC model, classical

density-functional theory (CDFT) postulates that the free energy of a system is a functional of its density. If the Helmholtz free energy of a system is expanded around a constant (e.g., liquid) state to second order then

(1.5)
$$F[\rho(\boldsymbol{r})] \approx F[\rho_0] + \int_V \left.\frac{\delta F[\rho]}{\delta\rho(\boldsymbol{r})}\right|_{\rho=\rho_0} \Delta\rho(\boldsymbol{r})d\boldsymbol{r} + \frac{1}{2!}\int_V\int_{V_1} \left.\frac{\delta^2 F[\rho]}{\delta\rho(\boldsymbol{r})\delta\rho(\boldsymbol{r}_1)}\right|_{\rho=\rho_0} \Delta\rho(\boldsymbol{r})\Delta\rho(\boldsymbol{r}_1)d\boldsymbol{r}_1 d\boldsymbol{r},$$

where $\rho$ is the density, $\rho_0$ is the reference density, and $\Delta\rho = \rho - \rho_0$. The first variation in Eq. (1.5) does not depend on interactions and is consequently just the entropic ideal free energy [**6**], and the second term is the isotropic two-particle direct correlation function [**7**]. With these changes and ignoring constants in energy, the one component free energy is

$$F[\rho(\boldsymbol{r})] = kT\int_V \left(\rho\ln\frac{\rho}{\rho_0} - \Delta\rho\right)d\boldsymbol{r} - \frac{1}{2}\int_V \Delta\rho(C_2 * \Delta\rho)d\boldsymbol{r} \tag{1.6}$$

where $C_2 * \Delta\rho = \int_{V_1} C_2(|\boldsymbol{r}_1 - \boldsymbol{r}|)\Delta\rho(\boldsymbol{r}_1)d\boldsymbol{r}_1$ and $C_2$ is the two-point direct correlation function. Performing the substitution $\phi = \frac{\rho-\rho_0}{\rho_0}$ and expanding the logarithm to fourth-order gives

$$F[\phi] = \rho_0 kT\int_V \left[\frac{1}{2}\phi^2 - \frac{1}{6}\phi^3 + \frac{1}{12}\phi^4 - \frac{1}{2}\phi C_2 * \phi\right]d\boldsymbol{r}, \tag{1.7}$$

the starting point for many PFC models. If the correlation function itself is expanded to fourth-order, i.e.

$$C_2 \approx (\tilde{C}_0 + \tilde{C}_2\nabla^2 + \tilde{C}_4\nabla^4)\delta(\boldsymbol{r} - \boldsymbol{r}_1), \tag{1.8}$$

and the result non-dimensionalized, Eq. (1.4) arises. Surprisingly, the simple PFC model in Eq. (1.4) gives accurate descriptions of elasticity—it reproduces both Read-Shockley grain boundary energies and Matthews and Blakeslee misfit dislocation behavior during epitaxy [**5**]. Further, this model with minor modifications has been quantitatively fit to body-centered cubic (bcc) iron [**8**, **9**].

Unfortunately, Eq. (1.4) can only produce stripes, triangular rods, and bcc patterns in any reasonable parameter range [**10**], and derivations from CDFT have been unsuccessful for deriving any structures beyond bcc [**11**]. Although the classical density functional theory community has claimed to correctly predict the structure of face-centered cubic (fcc) Al and hexagonal close packed (hcp) Mg [**12**], this result has never been successfully reproduced in the PFC community. The problem is that the liquid correlation function does not seem to contain enough information to determine the solid state crystal structure (Fig. 1.1).

Consequently, progress in the PFC community has largely been made by considering various phenomenological forms for the Fourier transform of the two-point correlation function, $\hat{C}_2$ [**11**, **13**, **14**]. For a $\hat{C}_2$ containing up to three peaks, there exist two-dimensional (2D) PFC models for all five Bravais lattices [**15**] and various chiral phases [**16**]. In three-dimensions, PFC models with this $\hat{C}_2$ can form simple cubic [**14**], fcc [**14**], hcp [**17**], and diamond cubic structures [**18**]. These phenomenological two-point correlation functions have generally been in the form of polynomial expansions or Gaussians. Gradient expansion models are simply generalizations of Eq. (1.8), where the expansion is to higher order than fourth-order, for example eighth or twelfth. In Gaussian models, known as structural PFC models (XPFC), the two-point correlation function

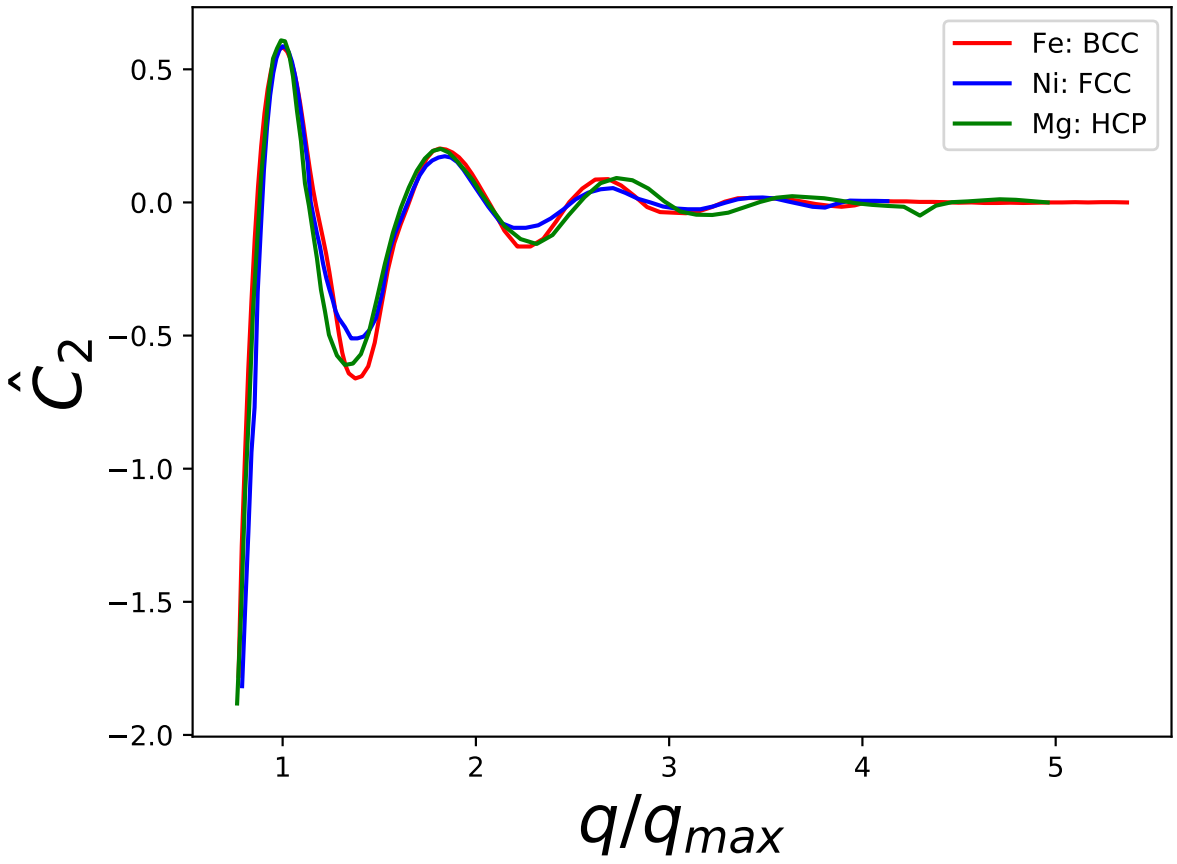


Figure 1.1. Experimental direct two-point correlation functions for a bcc, fcc, and hcp liquid metal slightly above melting point, with $q$ normalized so that the maximum of $\hat{C}_2(q)$ occurs at $q = 1$ [**1**]. Because the correlation functions for each metal are so similar, and in fact are well-approximated by a hard-sphere model, the liquid two-point correlation function alone seems unlikely to be sufficient to determine the solid crystal structure.

is

$$\hat{C}_2(q) = \max_j \left( b_j e^{\frac{-(q-q_j)^2}{2\sigma_j^2}} \right) \tag{1.9}$$

instead. Others have suggested functional forms such as rational functions [**19**] and Bessel functions [**20**] but have failed to gain traction.

Although the vast majority of PFC models truncate the free energy at the two-point correlation function, some recent work has included higher-order interactions. For example, if a three-point interaction is added, then

$$F[n] = F_1[n] + F_2[n] + F_3[n] \tag{1.10}$$

where $F_1 + F_2$ is Eq. (1.7) and

$$F_3[n] = -\frac{1}{6}\iiint n(\boldsymbol{r})C_3(\boldsymbol{r}-\boldsymbol{r}', \boldsymbol{r}-\boldsymbol{r}'')n(\boldsymbol{r}')n(\boldsymbol{r}'')d\boldsymbol{r}d\boldsymbol{r}'d\boldsymbol{r}'', \tag{1.11}$$

where $C_3$ is the three-point correlation function. Unlike the two-point correlation function, it is not trivial to express this correlation function in a form that is numerically efficient, rotationally invariant, and useful. For example, Tupper and Grant suggested a three-point correlation function early-on to create a two-dimensional square structure, but their form was of computational complexity $O(N^3)$, unlike the $O(N \log N)$ speed for the two-point correlation enabled by the fast-Fourier transform. Lavrskyi *et al.* were able to form highly complex crystal structures using the closely related atomic density field model [**21**], but they relied on a free-energy function that was not rotationally invariant [**22**]. In fact, Wang *et al.* recently proved that no gradient expansion for a three-point correlation function is rotationally invariant [**23**].

Seymour *et al.* made some progress by considering three-point correlations of the form [**20**]

$$C_3(\boldsymbol{r}_1, \boldsymbol{r}_2) = \sum_i C_3^{(i)}(\boldsymbol{r}_1)C_3^{(i)}(\boldsymbol{r}_2), \tag{1.12}$$

where $\boldsymbol{r}_1 \equiv \boldsymbol{r} - \boldsymbol{r}'$ and $\boldsymbol{r}_2 \equiv \boldsymbol{r} - \boldsymbol{r}''$. In this case, the free energy and evolution equations simplify into a number of convolutions of $O(N \log N)$ computational complexity that are easily computed via the fast-Fourier transform, and the isotropic theorem of Wang *et al.* is not a problem since the corresponding gradient expansion is of infinite order. Unfortunately, Seymour's proposal for the $C_3^{(i)}$ functions only yields two-dimensional equilibrium states with a specified bond angle where the bond angle, $\theta$, satisfies the relation

$$360^\circ \ mod\ \theta = 0, \tag{1.13}$$

for example 60°, 90°, and 120° [**20**]. Although this yields an improved 2D graphene model [**24**], this method is not flexible enough to generate any new crystal structures in either two or three dimensions [**20**].

In addition to the crystal structure limitations of Eq. (1.4) just discussed, another downside of the Swift-Hohenberg model is that it is for a single component material while most materials are multicomponent. The first multicomponent PFC model dealt with substitutional and intermetallic alloys. In this case, instead of the free energy being a function of the normalized atomic density of a single component, $F[n]$, the free energy is a function of the *total* normalized density and a long wavelength concentration order parameter, $F[n, c]$ [**6**, **25**, **26**]. In contrast to substitutional alloys, in intermetallic alloys the "concentration" order parameter varies on the length scale of the unit cell, and the long wavelength approximation is invalid. Instead, intermetallic PFC models utilize an additional correlation function to cause the "concentration" order parameter to vary on the length scale of the unit cell [**27**, **28**]. When the intermetallics have exact stoichiometries

that do not readily permit substitutions though, models are typically constructed as explicit functions of the separate component densities, $F[n_A, n_B]$ [**29**, **30**].

Despite this progress, these models permit simulations of only a small fraction of extant crystalline materials, and most applications of three-dimensional (3D) PFC models have been dominated by simulations of bcc [**8**, **9**, **27**, **31**, **32**] and fcc [**11**, **31**, **33**–**35**] elements or alloys. The challenge of producing complex crystal structures in PFC models is similar to that faced by the self-assembly community. Their goal is to solve the so-called "inverse" statistical mechanics problem: how to design interaction potentials between discrete particles such that a given structure is a global energy minimum. They have also found this task to be non-trivial [**36**–**39**].

A class of materials that exemplifies the limitations of PFC models are perovskites, which are of interest due to applications ranging from solar cells [**40**, **41**] to light-emitting diodes [**42**]. However, ferroelectric perovskites have multiple complex crystal structures, are made of multiple types of atoms, and exhibit both first- and second-order displacive phase transitions. Furthermore, a free energy that gives a ground state crystal structure with a particular symmetry is far from sufficient for a model to be useful, and perovskites demonstrate complex physics including coupling between electrodynamics, temperature, strain, composition, and boundary conditions.

Although a PFC model for displacive phase transitions does not exist, there does exist a plethora of phase-field models for modeling ferroelectrics. These models, also known as Landau-Ginzburg-Devonshire (LGD) models, postulate a free energy as a function of a polarization vector, gradients in the polarization vector, and elastic strain [**43**]. This theory has been used to predict topological phase transitions in ferroelectric nanoparticles

[**44**], understand ferroelectric switching and domain wall profiles in perovskites [**45**–**47**], and much more [**48**]. As PFC models naturally incorporate elasticity without requiring an explicit elastic field, Seymour *et al.*, based off of similar work in magnetic systems by Faghihi *et al.* [**49**, **50**], introduced a model [**51**] where the free energy is a function not only of the normalized atomic density but also the polarization vector and its gradient. This was accomplished by adding the polarization terms of LGD models onto a normal PFC functional [Eq. (1.4)], and then introducing appropriate coupling terms between the polarization and PFC terms in order to recover the traditional LGD models in the phase-field limit. As might be apparent from the descriptions alone, both Seymour's model and LGD models are quite complex. There are numerous remaining challenges for a simple and realistic perovskite model, and this thesis focuses on solving just a few of them.

Chapter 2 develops an equimolar binary PFC model that allows for sublattice ordering and that can be used to model a wide class of compounds. Section 2.1 derives the model directly from classical density functional theory, describes the general procedure for modeling any compound of interest, and implements a more appropriate temperature dependence of the Debye-Waller factor than used in the original XPFC models [**13**, **14**]. Section 2.2 examines the analytical behavior, elasticity, and numerical phase diagram for the specific case of a B2 compound, giving rise to both first- and second-order phase transitions. Section 2.3 applies this B2 model to the study of antiphase boundaries and their dynamical interactions with grain boundaries.

Chapter 3 develops a generalization of Seymour's three-point correlation model. This is done by introducing a form for $C_3$ that stabilizes angles between specified crystallographic planes and can include multiple length scales, multiple preferred angles, and angles not restricted by Eq. (1.13). Furthermore, an in-depth explanation for how to derive parameters for new energy-minimizing single-component crystal structures is given. We show that this method can produce a wide array of energy-minimizing crystal structures, from simple cubic (e.g., Po [**52**]) and diamond cubic (e.g., C-diamond, Si, $\alpha$-tin [**53**]), to graphene layers and disordered $CaF_2$ (e.g., the structure of the $\theta_c'$ phase of $Al_2Cu$, which is commercially very important for strengthening in aluminum alloys [**54**]). Additionally, it produces an unnamed crystal structure corresponding to the $X$ atoms in $ABX_3$ perovskite (a structure we will call $X_3$). Finally, as a capstone demonstration of the method, the $X_3$ and simple cubic models are combined to generate a perovskite crystal structure.

Chapter 4 develops a square two-component two-dimensional PFC model that spontaneously undergoes displacive phase transitions. Using a simple free energy, the crystal can undergo displacive transitions in $\langle 10 \rangle$ and $\langle 11 \rangle$ directions, and with a little more complexity, displacements in any direction are possible, in agreement with eighth-order Landau theory. This displacive phase-field crystal (DPFC) model also maps to Landau-Ginzburg-Devonshire (LGD) theories for ferroelectrics, and the DPFC and LGD models are compared in terms of phase transitions and domain walls. The DPFC model also displays stable quadrijunctions and pinning of domain wall evolution by dislocation cores.

CHAPTER 2

# Order-Disorder Model

This chapter describes a method to model order-disorder transitions in the PFC model. Prior to the publication of this chapter's contents in 2017, sublattice ordering modeling was not possible in the PFC framework, despite these compounds being of significant scientific interest. Interesting B2 CsCl-type compounds include the highly ductile rare earth intermetallics (YAg, YCu, DyCu) [**55**] and metal aluminides with high-temperature structural stability (FeAl, CoAl, NiAl) [**56**]. Further, because nearly all existing PFC models focus on solid-liquid coexistence, the only example of a second-order transition line in PFC theory was Seymour *et al.*'s paramagnetic to ferromagnetic transition [**51**]. However, order-disorder transitions can be both first order, for example $Cu_3Au$ ($L1_2$) and DyCu (B2) [**57**], or second order, for example CuZn (B2) and $Fe_3Al$ ($D0_3$) [**58**]. Second-order transitions are interesting as not only do they exhibit their namesake discontinuity in the second derivative of the free energy, but they also do not form wetted domain boundaries, instead exhibiting correlation lengths between antiphase boundaries (APBs) that diverge as the phase boundary is approached [**59**].

## 2.1. Ordered Binary PFC Model

### 2.1.1. Derivation from CDFT

As explained in Chapter 1, the free energy of a single component system from classical density function theory is

$$F_A[\rho_A] = \int_V \left( \rho_A \ln \frac{\rho_A}{\rho_{A0}} - \Delta\rho_A - \frac{1}{2}\Delta\rho_A C^{(2)}_{AA} * \Delta\rho_A \right) d\mathbf{r}, \tag{2.1}$$

where $C^{(2)}_{AA}$ is the two-particle correlation function for component $A$. For the case of a two component system,

$$F = F_A + F_B - kT \int \Delta\rho_A C^{(2)}_{AB} * \Delta\rho_B d\mathbf{r} \tag{2.2}$$

since $C^{(2)}_{AB} = C^{(2)}_{BA}$, where $C^{(2)}_{AB}$ is a partial correlation function between A and B [**6**]. Performing the substitutions $\rho = \rho_A + \rho_B$, $c = \rho_A/\rho$, and $\rho_0 = \rho_{A0} + \rho_{B0}$ results in

(2.3)

$$F = kT \int \left\{ \rho \ln \frac{\rho}{\rho_0} - (\rho - \rho_0) - \frac{1}{2}\rho \Big[ c C^{(2)}_{AA} c + (1-c) C^{(2)}_{BB} (1-c) + 2c C^{(2)}_{AB} (1-c) \Big] \rho + \right.$$
$$\left. \rho \Big[ (1-c)\ln(1-c) + c \ln c \Big] + \rho c \Big[ (C^{(2)}_{AA} - C^{(2)}_{AB})\rho_{A0} + (C^{(2)}_{AB} - C^{(2)}_{BB})\rho_{B0} + \ln \frac{\rho_{B0}}{\rho_{A0}} \Big] \right\} d\mathbf{r}$$

as in [**60**], where $\int \phi_1 C^{(2)} * \phi_2 d\mathbf{r} = \int \phi_2 C^{(2)} * \phi_1 d\mathbf{r}$ is written as $\int \phi_1 C^{(2)} \phi_2 d\mathbf{r}$ for brevity. For an $AB$ compound, using the following substitutions, [**61**]

(1) $\psi = 2c - 1 = \frac{\rho_A - \rho_B}{\rho_A + \rho_B}$

(2) $n = \frac{\rho - \rho_0}{\rho_0}$

(3) $\Delta C = \frac{\rho_0}{4}(C^{(2)}_{AA} + C^{(2)}_{BB} - 2C^{(2)}_{AB})$

(4) $\delta C = \frac{\rho_0}{4}(C^{(2)}_{AA} - C^{(2)}_{BB})$

(5) $\overline{C} = \frac{\rho_0}{4}(C^{(2)}_{AA} + C^{(2)}_{BB} + 2C^{(2)}_{AB})$

expanding $n$ and $\psi$ to fourth order, and ignoring linear terms as is customary [**6**] results in

$$F = kT\rho_0 \int_V \left\{ \frac{n}{2}\Big[1 - (\overline{C} + 2\delta C\psi + \psi\Delta C\psi)\Big]n - \frac{1}{6}n^3 + \frac{1}{12}n^4 + + \frac{1}{2}\psi(1-\Delta C)\psi \right.$$
$$\left. \frac{1}{2}\psi\Big[\ln\frac{\rho_{B0}}{\rho_{A0}} + \frac{2\Delta C}{\rho_0}(\rho_{A0} - \rho_{B0})\Big](n+1) + \frac{1}{12}\psi^4 - n\delta C\psi - n\psi\Delta C\psi + \frac{1}{2}n\psi^2 \right\} d\mathbf{r}. \tag{2.4}$$

As is typical in PFC models, $n$ is interpreted as the normalized atomic density and $\psi$ as the normalized difference in composition. Because the $\psi$ expansion is performed around $\psi = 0$, this model is only appropriate for systems where $c \simeq 1/2$. Of course, a more general model could be derived by expanding around a generic concentration, at the cost of increased complexity. In the random binary alloy case, $\psi$ is assumed to vary on a length scale much larger than the atomic unit cell. In this limit, Eq. (2.4) reduces to the free energy of the binary alloy [**60**]. However, drawing inspiration from the theory of concentration waves, our model regards $\psi$ as a field that specifies the chemical identity of atoms inside a unit cell [**62**].

Two additional simplifying assumptions are now made in order to make Eq. (2.4) more tractable. First, the fourth-order convolution term, $n\psi\Delta Cn\psi$, is neglected for numerical ease. Second, it is assumed that $C^{(2)}_{AA} = C^{(2)}_{BB}$ and $\rho_{A0} = \rho_{B0}$. This assumption treats pure A and B as equivalent and yields a phase diagram that is symmetric about a 50-50

stoichiometry. With these assumptions, Eq. (2.4) simplifies to

(2.5)
$$F = kT\rho_0 \int_V \left[\frac{1}{2}n^2 - \frac{1}{6}n^3 + \frac{1}{12}n^4 - \frac{1}{2}n\overline{C}n + \frac{1}{2}\psi^2 + \frac{1}{12}\psi^4 - \frac{1}{2}\psi\Delta C\psi + \frac{1}{2}n\psi^2 - n\psi\Delta C\psi\right] d\mathbf{r}.$$

In a situation where the effect of the ordering on the free energy is considered minor in comparison to the overall crystal structure, we phenomenologically add a factor of $\epsilon$ to all terms that involve ordering,

$$\begin{aligned}\tilde{F} = \int_V \Bigg[&\frac{1}{2}n^2 - \frac{1}{6}n^3 + \frac{1}{12}n^4 - \frac{1}{2}n\overline{C}n + \\ &\epsilon\Big(\frac{1}{2}\psi^2 + \frac{1}{12}\psi^4 - \frac{1}{2}\psi\Delta C\psi + \frac{1}{2}n\psi^2 - n\psi\Delta C\psi\Big)\Bigg] d\boldsymbol{r}\end{aligned} \tag{2.6}$$

where $\tilde{F} = F/(kT\rho_0)$. This $\epsilon$ factor will be further explained in Sec. 2.2.

### 2.1.2. Correlation Function Determination

In order to construct $\Delta C$ and $\overline{C}$, we adapt a methodology similar to Greenwood *et al.* by considering their form in Fourier space [**14**]. In this section, we demonstrate a method to determine where the peaks of the correlation function in Fourier space should be for a given target structure.

In the case of a bulk crystal, we can exactly express the density as a Fourier series over all the reciprocal lattice vectors, namely

$$\rho_A = \bar{\rho}_A + \sum_{\mathbf{k}} A_A(\mathbf{k}) e^{i\mathbf{k}\cdot\mathbf{r}} \ . \tag{2.7}$$

In the limit where $\rho_A$ consists of delta functions weighted by $f_A$ at each atomic position, then orthogonality gives easily calculable values for the amplitudes in terms of structure factors, namely

$$A_A(\mathbf{k}) = \frac{f_A}{V} \sum_{j \in \text{cell}} e^{-i\mathbf{k}\cdot\mathbf{r}_j} = \frac{1}{V} S_A(\mathbf{k}) \tag{2.8}$$

where $V$ is the volume of the unit cell, $j$ indexes through all atoms in the unit cell, and $S_A \equiv f_A \sum e^{-i\mathbf{k}\cdot\mathbf{r}_j}$ is the structure factor of $A$, consistent with the definition by Cullity and Kittel [**63**, **64**] (this definition is not universal [**65**, **66**]). Fourier expanding $n$ and $\psi$ using the same reciprocal lattice vectors as A and B results in

$$A_n = \frac{1}{\rho_0}(A_A + A_B) \tag{2.9}$$

and

$$A_\psi \simeq \frac{1}{\rho_0}(A_A - A_B), \tag{2.10}$$

where the approximation $\rho_A(\mathbf{r}) + \rho_B(\mathbf{r}) \simeq \rho_0$ (equivalent to assuming $n(\mathbf{r})$ is small) is used for deriving the latter expression.

Because the exact values calculated from Eq. (2.9) and Eq. (2.10) depend on the delta function assumption, these values will never occur in the numerical model. What is more important than the exact value calculated is whether the amplitude for a given $\mathbf{k}$ value is zero or nonzero, since the free energy is only affected by the value of the correlation function at $\mathbf{k}$ values when the amplitude for that same $\mathbf{k}$ is nonzero. This is because after

Fourier expanding $n$,

$$\int_V n\overline{C}nd\mathbf{r} = V\sum_{\mathbf{k}} |A_n(\mathbf{k})|^2\hat{\overline{C}}(|\mathbf{k}|), \tag{2.11}$$

where the hat denotes the Fourier transform. Since the amplitude for each individual component is proportional to its structure factor, we define $S_n \equiv S_A + S_B$ and $S_\psi \equiv S_A - S_B$, and we expect the underlying symmetries of these "structure factors" to preserve the symmetries in the amplitudes as is the case for experimental structure factors [**63**]. In order to calculate $S_n$ and $S_\psi$, the simplifying assumption that $f_A = f_B = f$ is employed, consistent with assuming $\rho_{A0} = \rho_{B0}$.

As an example, let us calculate the peak locations for the B2 system explicitly (Fig. 2.1). Practically, the relation $\Delta\phi(\mathbf{k}) = \mathbf{k}\cdot\mathbf{x}_0$ is helpful, where $\Delta\phi(\mathbf{k})$ is the change in phase in the structure factor as a result of moving the origin of the coordinate system by $\mathbf{x}_0$. Denoting $\mathbf{k} = h\mathbf{b}_1 + k\mathbf{b}_2 + l\mathbf{b}_3$, where $b_i$ is the $i$th reciprocal lattice vector, then

$$S_A = f \text{ for all h, k, l} \tag{2.12}$$

$$S_B = \begin{cases} f & \text{if } h+k+l = 2m \\ -f & \text{if } h+k+l = 2m+1 \end{cases}$$

and

$$\begin{aligned} S_n &= 2f \text{ if } h+k+l = 2m \text{ and} \\ S_\psi &= 2f \text{ if } h+k+l = 2m+1 \end{aligned} \tag{2.13}$$

where $m$ is an integer. Thus, the only $\mathbf{k}$ that are non-zero are

$$n: \quad \tfrac{2\pi}{a}\{110\}, \tfrac{2\pi}{a}\{200\}, \tfrac{2\pi}{a}\{211\}, ... \tag{2.14}$$

$$\psi: \quad \tfrac{2\pi}{a}\{100\}, \tfrac{2\pi}{a}\{111\}, \tfrac{2\pi}{a}\{210\}, ... \tag{2.15}$$

where $\{\}$ denotes a family of reciprocal lattice vectors created by the permutation of the internal elements (for example, $\{110\}$ includes 12 vectors: $\hat{x}+\hat{y}$, $\hat{x}-\hat{y}$, $\hat{x}+\hat{z}$, ...). The structure factor [Eq. (2.13)] for $n$ is consistent with the missing reflections for a BCC lattice. Because the first nonzero $\mathbf{k}$ for $n$ has magnitude $2\pi\sqrt{2}/a$, and the first nonzero $\mathbf{k}$ for $\psi$ has magnitude $2\pi/a$, the ratio of the first peak in $\overline{C}$ in reciprocal space to the first in $\Delta C$ must be $\sqrt{2}$. This same procedure can be easily performed to construct correlation functions for other 50-50 stoichiometry compounds, with the results for the locations of the first three peaks for $n$ and $\psi$ for various compounds listed in Table 2.1. All compounds listed in Table 2.1 can produce (at least) metastable structures using at most three peaks. However, many, such as B2, can exist with fewer, with the exact stability regimes depending on parameter choices. The model can be extended to other compounds without 50-50 stoichiometry through this same method, but as explained in Sec. 2.1.1, rigorously the free energy should also be derived with that additional complication—an extension left for future work. Although the values of the correlation function at specific $|\mathbf{k}|$ values are the only quantities that determine equilibrium structure, the exact functional form of the correlation function is important for properties such as elastic constants, defect structures, and dynamics.

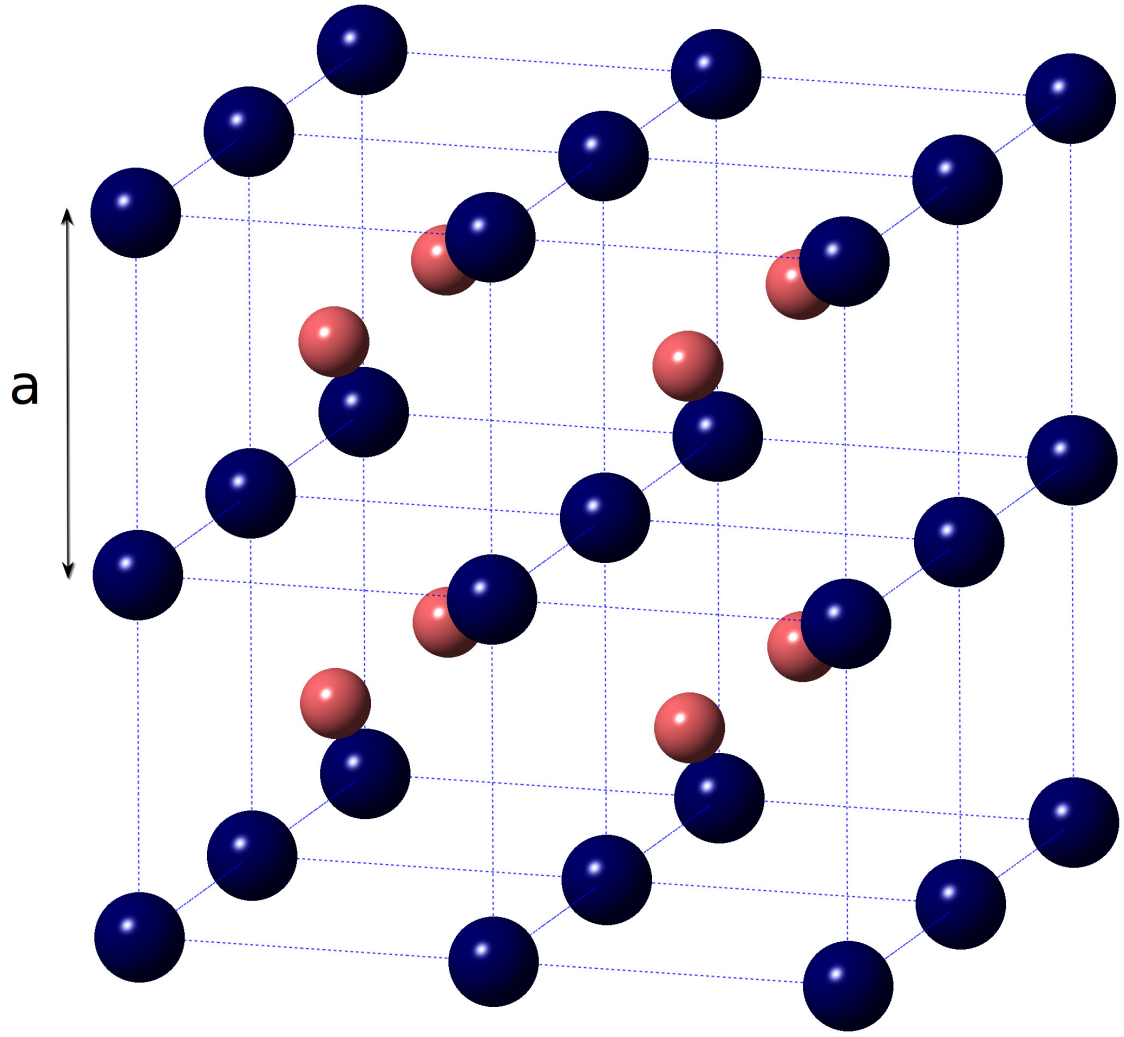


Figure 2.1. Structure for a B2 crystal. The origin used for calculating the structure factor is at the center of a dark blue atom.

### 2.1.3. XPFC Model

In this study, the XPFC formalism was employed [**13**, **14**]. In the case of a single peak for $n$ and $\psi$,

$$\hat{\overline{C}} = B_x e^{-T/T_n} e^{-\frac{(k-k_n)^2}{2\alpha_n^2}} \text{ and } \Delta\hat{C} = D_x e^{-T/T_\psi} e^{-\frac{(k-k_\psi)^2}{2\alpha_\psi^2}}, \tag{2.16}$$

Table 2.1. Table of peak locations, $|\mathbf{k}|_i \equiv k_i$, for the $n$ and $\psi$ correlation functions in reciprocal space for various crystal structures. The $k_i$ values for each structure were calculated using a square/cubic unit cell with side lengths of $2\pi$, except p3m1 whose calculation was performed using a rectangular unit cell with dimensions $2\pi \times 2\sqrt{3}\pi$. Because the calculations are performed on nonprimitive unit cells for convenience, the total atoms per cell are listed in order to uniquely identify the unit cell geometry.

| Space Group | Example | Atoms/Cell | $k_n$ | $k_\psi$ |
|---|---|---|---|---|
| p4gm | {100} NaCl | 4 | 2, $\sqrt{8}$, 4 | $\sqrt{2}$, $\sqrt{10}$, $\sqrt{18}$ |
| p3m1 | 2d h-BN | 4 | $2/\sqrt{3}$, 2, $4/\sqrt{3}$ | $2/\sqrt{3}$, $4/\sqrt{3}$, $\sqrt{28/3}$ |
| $Pm\bar{3}m$ (B2) | CuZn | 2 | $\sqrt{2}$, 2, $\sqrt{6}$ | 1, $\sqrt{3}$, $\sqrt{5}$ |
| $Fd\bar{3}m$ (B32) | NaTl | 16 | $\sqrt{8}$, 4, $\sqrt{24}$ | $\sqrt{3}$, $\sqrt{11}$, $\sqrt{19}$ |
| P4/mmm ($L1_0$) | CuAu | 4 | $\sqrt{3}$, 2, $\sqrt{8}$ | 1, $\sqrt{2}$, $\sqrt{5}$ |

where $k \equiv |\mathbf{k}|$, $B_x$ and $D_x$ are phenomenological constants, $T$ is a temperature-like parameter, $T_n$ controls the solid-liquid transition temperature, and $T_\psi$ controls the ordering temperature. The one-peak XPFC model has the advantage compared to polynomial PFC models in that the former does not exhibit significant changes in the equilibrium lattice constant with changes in average density or temperature, simplifying phase diagram construction. In polynomial PFC models, such as Eq. (1.4), the equilibrium lattice constant is determined by a competition between the energies of the primary frequency and the higher order harmonics; the primary frequency energy is minimized by a lattice constant that corresponds to the extremum of the correlation function while the higher frequencies decrease in energy by increasing the lattice constant [**67**]. However, the correlation function in XPFC quickly goes to zero for large $k$. Consequently, changing the lattice constant only negligibly affects the energetic contributions of higher frequency modes, and so the lattice constant is chosen purely so that the primary frequency of the structure coincides with the correlation function's maximum. Because the peak location in the

correlation function is independent of temperature and composition, the lattice constant is not affected by these parameters.

This particular computational advantage of XPFC comes at the price of a less accurate one mode approximation however. Because polynomial correlation functions diverge for large $k$, their correlation functions strongly penalize higher order harmonics, resulting in free energies dominated by only the primary frequency [**6**, **11**, **15**]. In contrast, the XPFC correlation function vanishes for large $k$, rather than negative, so higher order harmonics play a larger role.

Unlike that shown in Eq. (2.16), previous XPFC models have assumed that the temperature is proportional to $\sigma$, using a temperature factor $\exp(\sigma^2/\sigma_M^2)$, equivalent to treating $\sqrt{T}$ as the temperature in Eq. (2.16) [**13**, **14**, **35**, **68**, **69**]. However, this relation is inconsistent with the usual temperature dependence of the Debye-Waller factor observed in diffraction experiments. When temperatures are much higher than the Debye temperature of the crystal, which is the case for PFC models [**63**], the atomic structure factor can be approximated as [**64**]

$$f = f_0 e^{-T/T_0} \ . \tag{2.17}$$

Assuming $\hat{C}(k) \propto f^\nu$, meaning the correlation function peak height scales with the atomic structure factor to some power, then in the case $T \ll T_0$, $\hat{C}(k)$ decreases linearly with $T$. Note that this is exactly the temperature dependence of the correlation function in PFC models with polynomial correlation functions and is consistent with the linear temperature dependence of the quadratic term in Landau models. For example, in Eq. (1.4), $\varepsilon$ is considered the variable proportional to the temperature, and it decreases the effective

correlation function linearly. Because the original XPFC model goes as $\exp(\sigma^2/\sigma_M^2)$, in the limit $\sigma \ll \sigma_M$ the correlation function decreases quadratically with $\sigma$. Although understanding that in the original XPFC terminology $\sigma^2$ is the temperature parameter rather than $\sigma$ does not matter when fitting data at a particular temperature, nor does it matter when calculating the shape of phase diagrams qualitatively, it does affect the values of critical exponents (see Sec. 2.3).

## 2.2. B2 Ordering

In the remainder of this chapter, three B2 models based on Eq. (2.6) will be examined. The first model considers the limit $\epsilon \to 0$ in Eq. (2.6). Namely, the density field is considered completely independent of the composition field, but the composition field is dependent on the density field. This assumption is analytically equivalent to separating the free energy into two separate equations,

$$\mathcal{F}_n = \int_V \left[\frac{1}{2}n^2 - \frac{1}{6}n^3 + \frac{1}{12}n^4 - \frac{1}{2}n\overline{C}n\right] d\mathbf{r}$$

$$\text{and } \mathcal{F}_\psi = \int_V \left[\frac{1}{2}\psi^2 + \frac{1}{12}\psi^4 - \frac{1}{2}\psi\Delta C\psi + \frac{1}{2}n\psi^2 - n\psi\Delta C\psi\right] d\mathbf{r} \tag{2.18}$$

with $\tilde{F} = \mathcal{F}_n + \epsilon\mathcal{F}_\psi$. For dynamical behavior, evolution follows the typical simplified conserved Cahn-Hilliard equations [**6**]

$$\frac{\partial n}{\partial t} = M_n\nabla^2\frac{\delta\mathcal{F}_n}{\delta n} \tag{2.19}$$

$$\frac{\partial \psi}{\partial t} = M_\psi\nabla^2\frac{\delta\mathcal{F}_\psi}{\delta \psi}. \tag{2.20}$$

This approach, which we will call the "uncoupled" case, is both computationally cheaper compared to the "coupled" case (i.e. nonzero $\epsilon$) and is also significantly simpler with respect to phase diagram construction because the $n$ field in isolation has already been described by the original XPFC papers [**13**, **14**].

Similar to the uncoupled model is the "weakly coupled" model, which uses a finite $\epsilon \ll 1$. For simplicity, the evolution equations for the coupled case simply replaces $\mathcal{F}_n$ and $\mathcal{F}_\psi$ with $\tilde{F}$ rather than the rigorously derived evolution equations described by Jugdutt [**70**] although both methods result in the same equilibrium states. Assuming $\epsilon \ll 1$ is physically reasonable because the energy associated with order-disorder transitions is significantly less than that for atomic rearrangements. For example, in the FeAl system at 0 K, the free energies of ordered B2 and disordered A2 structures are within 0.001 eV/atom of each other [**71**, **72**]. In contrast, $B_h$, the FeAl ordered structure with the next lowest energy, is 0.125 eV/atom higher in energy [**71**]. Both the weakly coupled and uncoupled models result in phase diagrams with a line of second-order transitions.

The last model, the "strongly coupled" case, considers when $\epsilon = 1$, or equivalently Eq. (2.5). In this case, there are very different $n$ fields in the B2 versus A2 (disordered) phases, giving rise to first-order transitions. Further, because this model strongly couples the $n$ and $\psi$ fields, a disordered hexagonal rod phase is in competition with the B2 and A2 phases. For all parameter regimes tested with a single peak, B2-hexagonal rod coexistence occurred rather than B2-A2 coexistence. Consequently, an additional $k = 0$ peak was added to $\Delta C$ in order to preferentially stabilize the A2 phase over the hexagonal

rod phase. Namely,

$$\Delta\hat{C} = D_0 e^{-\frac{k^2}{2\alpha_\psi^2}} + D_x e^{-T/T_\psi} e^{-\frac{(k-k_\psi)^2}{2\alpha_\psi^2}}, \tag{2.21}$$

where $D_0$ was phenomenologically chosen.

### 2.2.1. Analytic Phase Diagram

Because the structure factors for $n$ and $\psi$ for the B2 system (Eq. 2.13) are real and only dependent on $|\mathbf{k}|$, a one mode approximation for $n$ and $\psi$ is

$$n = \bar{n} + A_n \sum_{j\in\{110\}} e^{i\mathbf{k}_j\cdot\mathbf{r}} \text{ and } \psi = \bar{\psi} + A_\psi \sum_{j\in\{100\}} e^{i\mathbf{k}_j\cdot\mathbf{r}}, \tag{2.22}$$

where, $\vec{k}_j = \frac{2\pi}{a}(h,k,l)$, $A_n$ and $A_\psi$ are constant real numbers, and $A_\psi$ is the system's order parameter. Substituting equations 2.16 and 2.22 into Eq. (2.18) and integrating with the equilibrium lattice parameter results in

$$\mathcal{F}_n = 6\bar{n}^2A_n^2 + 16\bar{n}A_n^3 - 6\bar{n}A_n^2 + \frac{\bar{n}^4}{12} - \frac{\bar{n}^3}{6} + \frac{\bar{n}^2}{2} + 6A_n^2(1 - B_x e^{-\frac{T}{T_n}}) + 45A_n^4 - 8A_n^3, \tag{2.23}$$

$$\mathcal{F}_\psi = -6\bar{n}A_\psi^2 D_x e^{-\frac{T}{T_\psi}} + 3\bar{n}A_\psi^2 + 3\bar{\psi}^2A_\psi^2 + \frac{1}{2}\bar{n}\bar{\psi}^2(1-2D_0) + \frac{\bar{\psi}^4}{12} + \frac{\bar{\psi}^2}{2} + A_\psi^2\left[12A_n(1-2D_x e^{-\frac{T}{T_\psi}}) - 3D_x e^{-\frac{T}{T_\psi}} + 3\right] + \frac{15A_\psi^4}{2} - \frac{D_0}{2}\bar{\psi}^2. \tag{2.24}$$

The phase diagram was constructed using four methods using the parameters shown in Table 2.2, which was also used for the numerical phase diagram (Fig. 2.5 and 2.6). The

first and simplest method used the uncoupled free energy. These calculations were performed at $\bar{n} = 0$ by both a common tangent construction and by solving $\partial^2 \mathcal{F}_\psi^{\text{order}} / \partial A_\psi^2 = 0$ (Fig. 2.2). Both techniques yielded the same result, implying a second-order transition. The second method was similar, except that it investigated the weakly coupled model with $\epsilon = 0.05$. Unsurprisingly, it gave a similar result. Although constructing the phase diagram at $\bar{n} = 0$ is a common approximation for a constant pressure phase diagram [**25**], it is known to not be thermodynamically consistent [**70**, **73**]. For the third method, the phase boundary was calculated for the weakly coupled model using the true two-phase equilibrium conditions

$$\mu_{eq} = \left(\tfrac{1}{\bar{n}+1}\tfrac{\partial \bar{F}}{\partial \bar{\psi}}\right)\Big|_{B2} = \left(\tfrac{1}{\bar{n}+1}\tfrac{\partial \bar{F}}{\partial \bar{\psi}}\right)\Big|_{A2} \tag{2.25}$$

$$\left(\tfrac{\partial \bar{F}}{\partial \bar{n}} - \bar{\psi}\mu_{eq}\right)\Big|_{B2} = \left(\tfrac{\partial \bar{F}}{\partial \bar{n}} - \bar{\psi}\mu_{eq}\right)\Big|_{A2} \tag{2.26}$$

$$p = \left((\bar{n}+1)\tfrac{\partial \bar{F}}{\partial \bar{n}} - \bar{F}\right)\Big|_{B2} = \left((\bar{n}+1)\tfrac{\partial \bar{F}}{\partial \bar{n}} - \bar{F}\right)\Big|_{A2} \tag{2.27}$$

where $\bar{n}$ and $\bar{\psi}$ can differ between the two phases and $\bar{F} \equiv \tilde{F}/V$ [**73**]. Notice that using these equilibrium conditions, the densities of the two phases can differ. However, for the weakly coupled model, the solution within numerical resolution is coexistence at the same densities and compositions, implying a second-order transition. For a judicious choice of pressure ($p = -0.063$), $\bar{n} \simeq 0$ at all temperatures, and the phase boundary is very similar to those calculated by the previous techniques.

The last phase diagram construction was done for the strong coupling case with $p = -0.063$, $\epsilon = 1$, and $D_0 = 0.5$ (Fig. 2.3). Unlike weak coupling, this results in first-order transitions with two-phase coexistence. Calculating the order parameter of the B2 phase

for increasing temperatures at $\bar{\psi} = 0$, where $\bar{n}$ is the B2 coexistence value, results in a discontinuity in the order parameter at the point where the two phase boundaries meet (Fig 2.4). Consequently, this point is a congruent point. In contrast, the order parameter would go continuously to zero if it was a critical point with a second-order transition.

In order to use Eq. (2.23) and Eq. (2.24) to describe a real compound such as FeCo [**74**], one can simply match properties such as the temperature and second derivative of the phase boundary at the critical point measured from an experimental phase diagram to the corresponding values at the critical point in the analytic (or numeric) model.

### 2.2.2. Elasticity

Since $\rho_A$ and $\rho_B$ ought to undergo identical strains, the $\psi$ field is strained identically to the $n$ field. Substituting in Eq. (2.22) into Eq. (2.6) and applying isotropic, biaxial, and simple shear strains at $\bar{n} = \bar{\psi} = 0$ as described by Pisutha-Arnond [**75**] results in the "traditional" elastic constants

$$C_{11}^t = \frac{A_n^2 B_x e^{-\frac{T}{T_n}}}{\alpha_n^2} + \frac{\epsilon \left(8A_n + 1\right) A_\psi^2 D_x e^{-\frac{T}{T_\psi}}}{2\alpha_1^2} \tag{2.28}$$

$$C_{12}^t = C_{44}^t = \frac{A_n^2 B_x e^{-\frac{T}{T_n}}}{2\alpha_n^2} \ . \tag{2.29}$$

Note that the strains only couple to the correlation terms in the free energy and are not affected by the ideal entropy of mixing terms. Spatschek and Karma ( [**76**], Eq. 59) make two related predictions for a free energy consisting of a single peak in the correlation

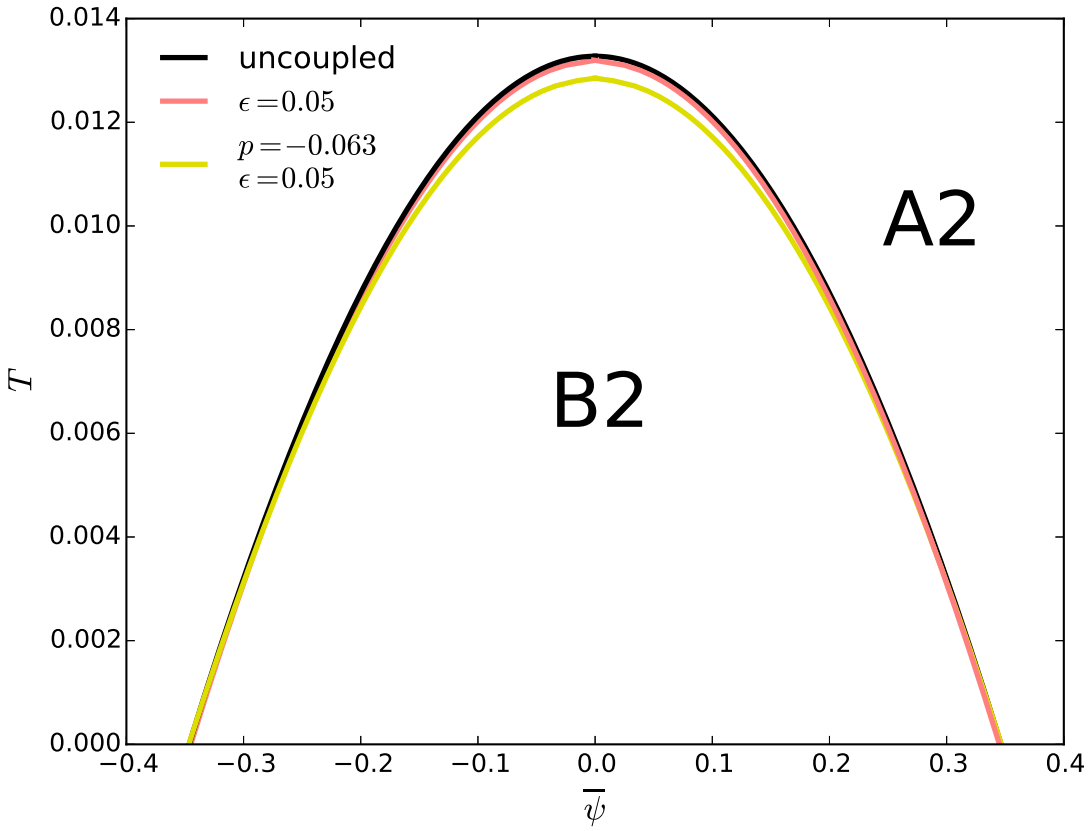


Figure 2.2. Phase diagram for analytical model. The uncoupled and coupled models using a common tangent equilibrium condition are compared to a constant pressure phase diagram. As all phase diagrams are very similar, including constant pressure and weak coupling complications appear to have little effect.

function. First, they predict that

$$\frac{C^t_{11}}{2} = C^t_{12} = C^t_{44} = -\frac{1}{2}C''(q_0)q_0^2 A^2_{110} \ , \tag{2.30}$$

which, using Eq. (2.14), agrees with Eqs. (2.28) and (2.29) in the limit $\epsilon = 0$. Second, they predict that $C^t_{12}$ and $C^t_{44}$ depend on neither $\{100\}$ nor $\{200\}$ amplitudes. This

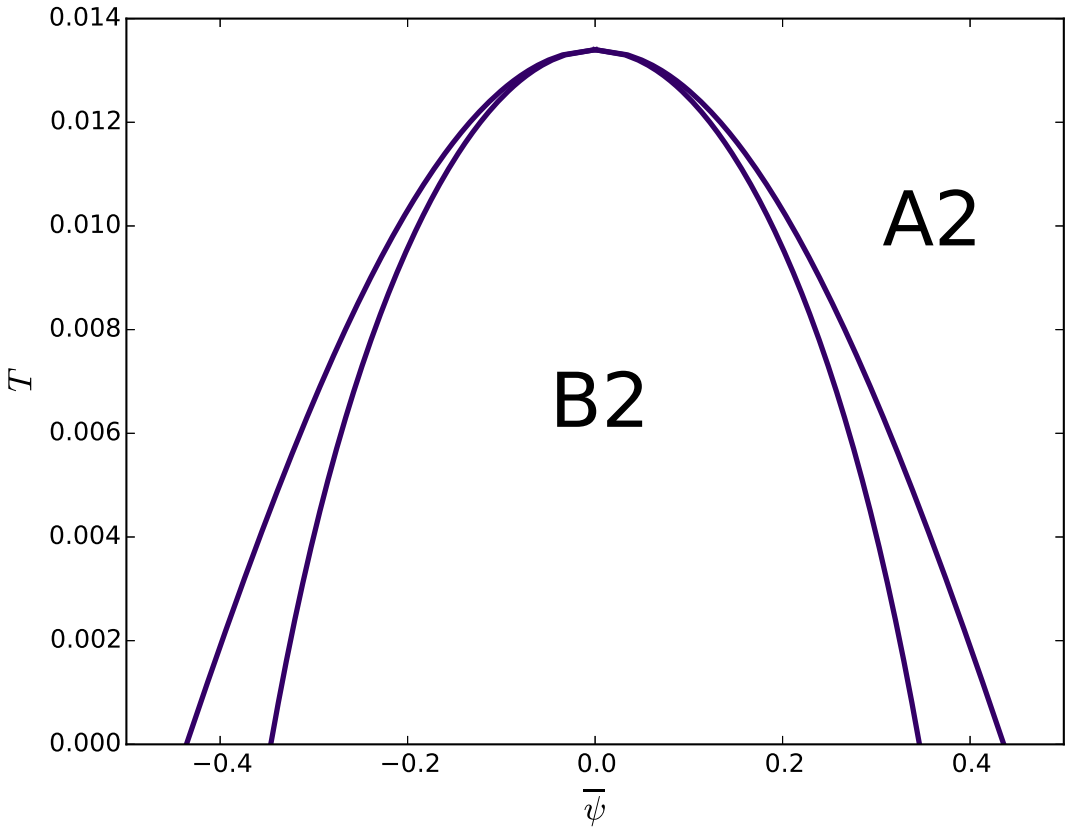


Figure 2.3. Phase diagram for analytical model in strongly coupled case, $\epsilon = 1$, at pressure = -0.063.

explains why only $C_{11}^t$ depends on the ordering amplitude, since the ordering wave is a $\{100\}$ mode.

Another way to help rationalize the lack of ordering dependence of the $C_{44}^t$ elastic constant is that $C_{44}$ physically represents shear on $\{100\}$ planes. These planes are of a single atom type, however, and thus not really dependent on ordering (to lowest order). The shear mode on the $\{110\}$ planes is proportional to $C_{11} - C_{12}$, and as expected does depend on $A_\psi$.

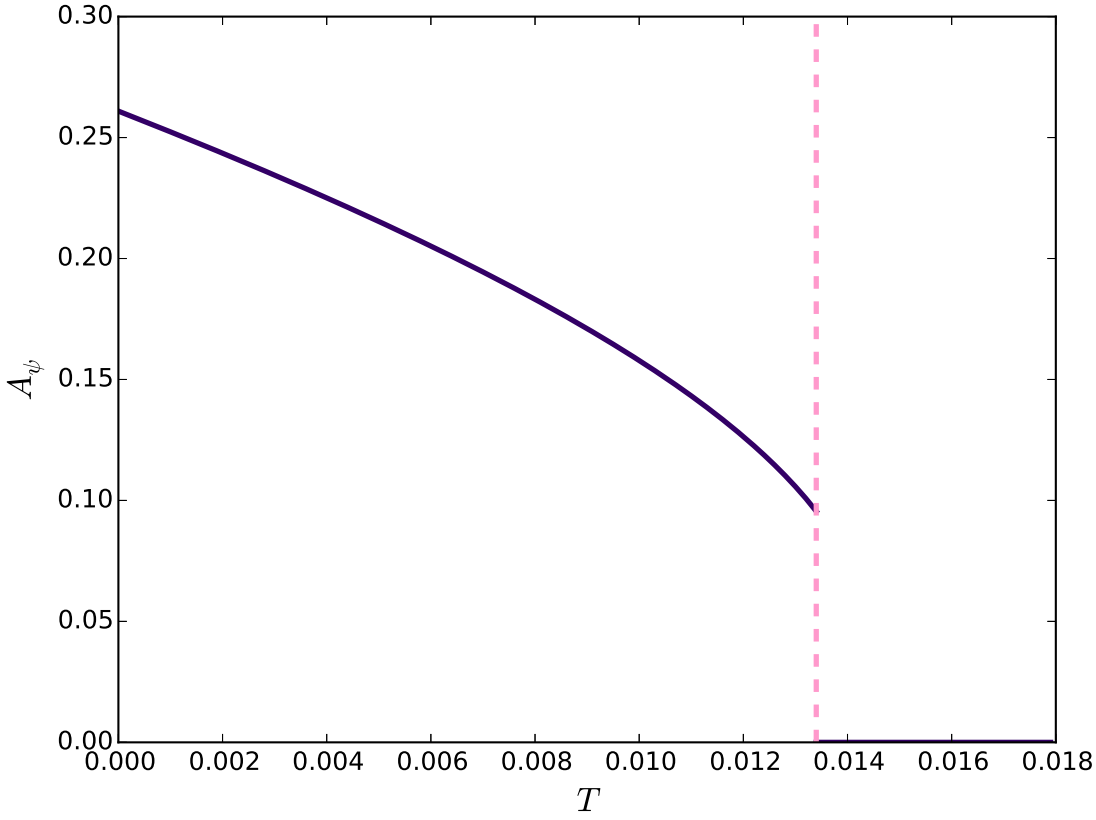


Figure 2.4. Plot of the order parameter as a function of $T$ for $\bar{\psi} = 0$. Because of the discontinuity of the order parameter from nonzero to zero, the transition is first-order with a congruent point at $T \simeq 0.0134$.

Equations (2.28) and (2.29) also agree with the Monte Carlo simulations of a B2 compound by Castan and Planes who found that the shear modulus, $(C_{11} - C_{12})/2$, is linearly proportional to the long-range order parameter squared [**77**]. However, Eqs. (2.28) and (2.29) are inconsistent with experimental data for CuZn as McManus found no anomalous behavior near the critical temperature for $C_{11}$, but an abrupt change in $\frac{dC_{44}}{dT}$ shortly before the critical temperature [**78**]. This is possibly because the discrepancy

between the "traditional" elastic constants, $C_{ij}^t$ and the true elastic constants, $C_{ij}$, as recently discussed by Wang [**79**].

### 2.2.3. Numerical Phase Diagram

To confirm the behavior of the one-mode model phase diagram in the case where all frequencies were included, the phase diagram was calculated numerically at $\bar{n} = 0$ for the uncoupled (Fig. 2.5), weakly coupled ($\epsilon = 0.05$, Fig. 2.5), and strongly coupled ($\epsilon = 1, D_0 = 0.5$) cases (Fig. 2.6). Because the constant pressure condition was unimportant when constructing the analytic phase diagrams, only the $\bar{n} = 0$ method was employed for ease when constructing the numerical phase diagrams. Numerical construction of the phase diagrams validated the qualitative behavior of a curve of second-order and first-order transitions seen previously. Quantitative disagreement with analytical results are explained by the fact that the XPFC model permits high frequency modes, so the one mode approximation provides poor quantitative estimates of free energies (see Sec. 2.1.3).

The free energies for the phase diagram were calculated by minimizing the free energy in a $2 \times 2 \times 2$ set of unit cells using the parameters found in Table 2.2. Each system was initialized by either a prior equilibrated structure for different parameters or by a single mode approximation. Each system was then evolved using Eq. (2.19) and Eq. (2.20) using the standard semi-implicit integral spectral method [**60**]. Conditions near the phase transition were tested carefully to ensure that the order of the transition was determined correctly. The amplitude of the $\{100\}$ peak from the numerical Fourier transform of $\psi$ was treated as the order parameter in the numerical model (Fig. 2.7). In the case of first-order transitions, the coexistence region was determined by fitting a fourth-order polynomial

through a set of free energies for B2 and A2, and then finding the convex hull. The phase transition in the simulations can be understood as follows: At $\bar{\psi} = 0$, the ordered state for $\psi$ consists of only the ordering modes ($\{100\}$, $\{111\}$, ...). For $\bar{\psi} \neq 0$, the disordering modes ($\{110\}$, $\{200\}$, ...) appear and gradually increase in magnitude while the ordered reflections diminish (see Sec. 2.1.2). At the phase transitions, only the disordered modes remain.

The first-order transition was also confirmed by equilibrating a $2 \times 2 \times 128$ simulation box of B2-A2 using $\bar{\psi} = 0.265$ and $T = 0.0144$. As predicted, B2 and A2 were found to coexist at equilibrium. Although the two phases had different average densities as suspected, $\bar{n}_{B2} \simeq 0.052$ and $\bar{n}_{A2} \simeq -0.027$, both densities were still close to zero. In order to speed up this large calculation, simple conserved global dynamics were used for both the $n$ and $\psi$ fields in this calculation [**70**, **80**], namely

$$\frac{\partial n}{\partial t} = -\frac{\delta \tilde{F}}{\delta n} + \frac{1}{V}\int_V \frac{\delta \tilde{F}}{\delta n} d\mathbf{r} \tag{2.31}$$

$$\frac{\partial \psi}{\partial t} = -\frac{\delta \tilde{F}}{\delta \psi} + \frac{1}{V}\int_V \frac{\delta \tilde{F}}{\delta \psi} d\mathbf{r}. \tag{2.32}$$

## 2.3. Applications

### 2.3.1. Antiphase Boundaries

As a test case for a system with a second-order transition, antiphase boundaries (APB) were investigated using the uncoupled model. Experimental evidence and Landau-Ginsburg

Table 2.2. Table of parameter values for phase diagrams.

| Quantity | Value |
|---|---|
| $M_n$ | 1 |
| $M_\psi$ | 1 |
| $T_n$ | 1 |
| $T_\psi$ | .2 |
| $k_n$ | 1 |
| $k_\psi$ | $1/\sqrt{2}$ |
| $D_x$ | 0.8 |
| $D_0$ | 0.5 (strongly coupled)<br>0 (otherwise) |
| $B_x$ | 1 |
| $\alpha_n$ | 0.08 |
| $\alpha_\psi$ | 0.08 |
| $a_0$ | $2\pi\sqrt{2}$ |
| Mesh | 16 / unit cell dimension |
| $\Delta t$ | 0.015 |

theory predicts that the signed local order parameter, $\eta$, across the APB boundary is [**58**]

$$\eta(z;T) = A_\psi(T)\tanh\left(\frac{z-z_0}{2\xi(T)}\right) \tag{2.33}$$

where $A_\psi$ is the unsigned bulk order parameter, $\xi$ is the correlation length, z is the coordinate perpendicular to the APB, and $z_0$ is the position of the interface. $A_\psi$, the APB energy $\gamma$, and $\xi$ all exhibit critical exponents. Meaning, near the critical point they are of the form $\sim \left(\frac{T_c-T}{T_c}\right)^{\nu_i}$, for some corresponding critical exponent $\nu_i$. This result was verified in the uncoupled B2 PFC model by initializing with a single mode approximation for two domains with opposite order parameters in a single grain, and the free energy was minimized using Eq. (2.19). The parameters in Table 2.2 were used except $\alpha_\psi = 0.25$ in order to reduce the width of the APB so that the simulation could be performed in a smaller domain. This change in $\alpha_\psi$ gave a new $T_c \simeq 0.01750$. A box size of $2 \times 2 \times 24$

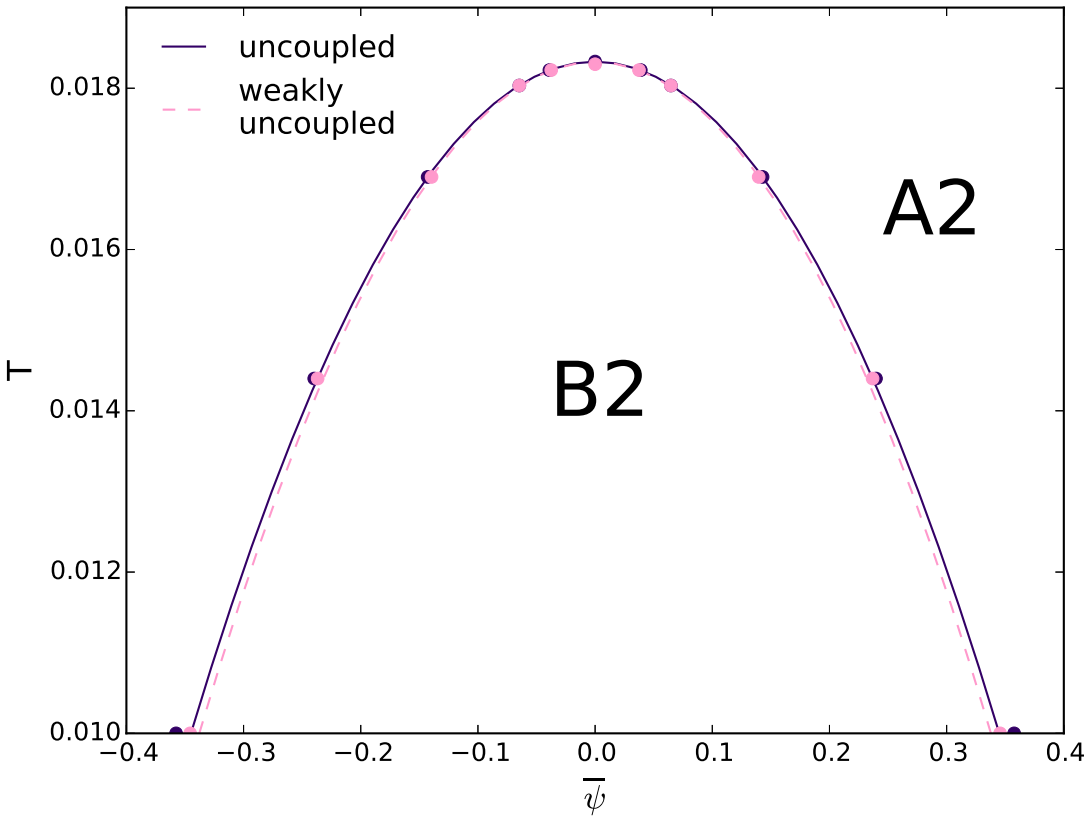


Figure 2.5. Numerical phase diagram for the B2 system, with the uncoupled case (solid violet line) and weakly coupled case (dashed pink line). Consistent with the analytic results, the weakly coupled and uncoupled cases nearly overlap with second-order transitions. The curves are parabolic fits through the numerically determined points.

unit cells was used with periodic boundary conditions (i.e. two identical APBs). A comparison of a typical numerical result and a hyperbolic tangent profile fit is shown in Fig. 2.8. Because the local order parameter, $\eta$, is a function of position in this case, the amplitude of $\psi$ along a unit cell edge was used as a proxy for the order parameter. The measured critical exponent for $A_\psi$ was 0.51 with $R^2 \simeq 1.0 \times 10^{-6}$. The critical exponent

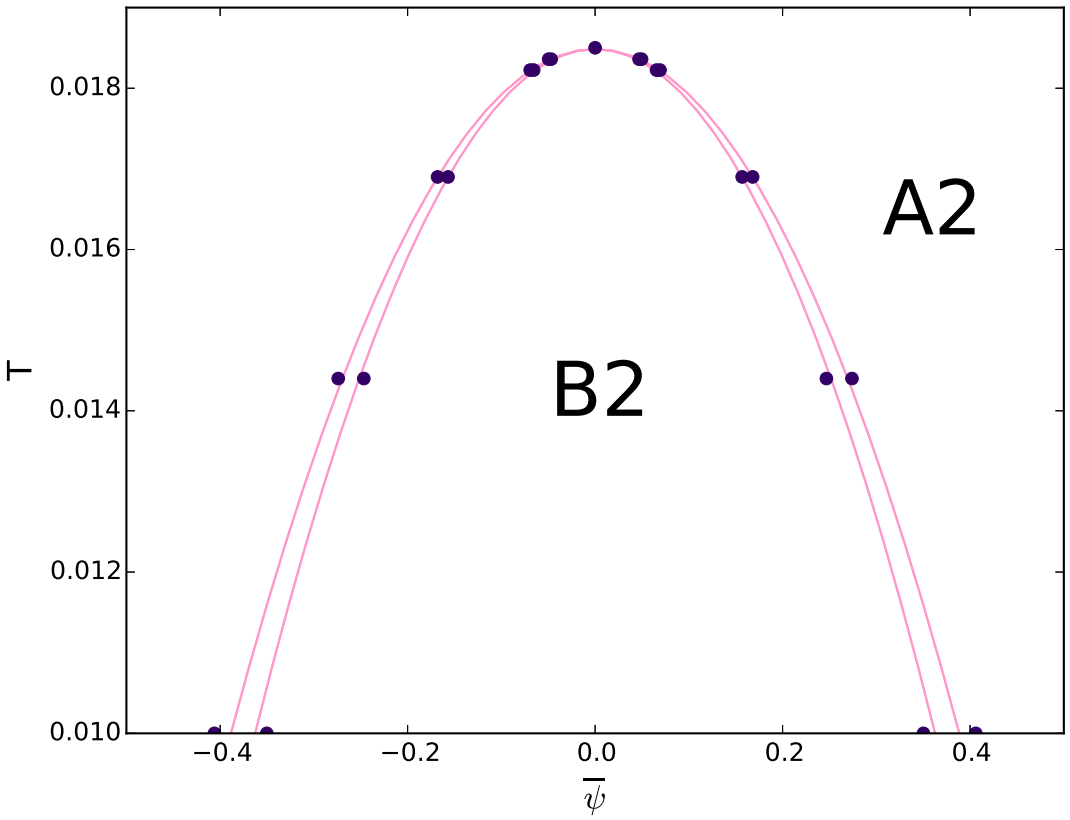


Figure 2.6. Numerical phase diagram for the B2 system in the strongly coupled case. Consistent with the analytic results, the transition is always first-order, and the region between the phase boundaries is coexisting B2 and A2. The curves are parabolic fits through the numerically determined points.

for the APB energy calculated using the typical form

$$\gamma = \frac{l_\perp}{2}(\bar{\mathcal{F}}_{\psi,\,\mathrm{APB}} - \bar{\mathcal{F}}_{\psi,\,\mathrm{eq}}), \tag{2.34}$$

was 1.53 with $R^2 \simeq 2.7 \times 10^{-5}$ (Fig. 2.9), where $l_\perp$ is the length of the simulation box in the $z$ direction, $\bar{\mathcal{F}}_{\psi,\,\mathrm{APB}}$ is the free energy per volume measured with the APB, and $\bar{\mathcal{F}}_{\psi,\,\mathrm{eq}}$

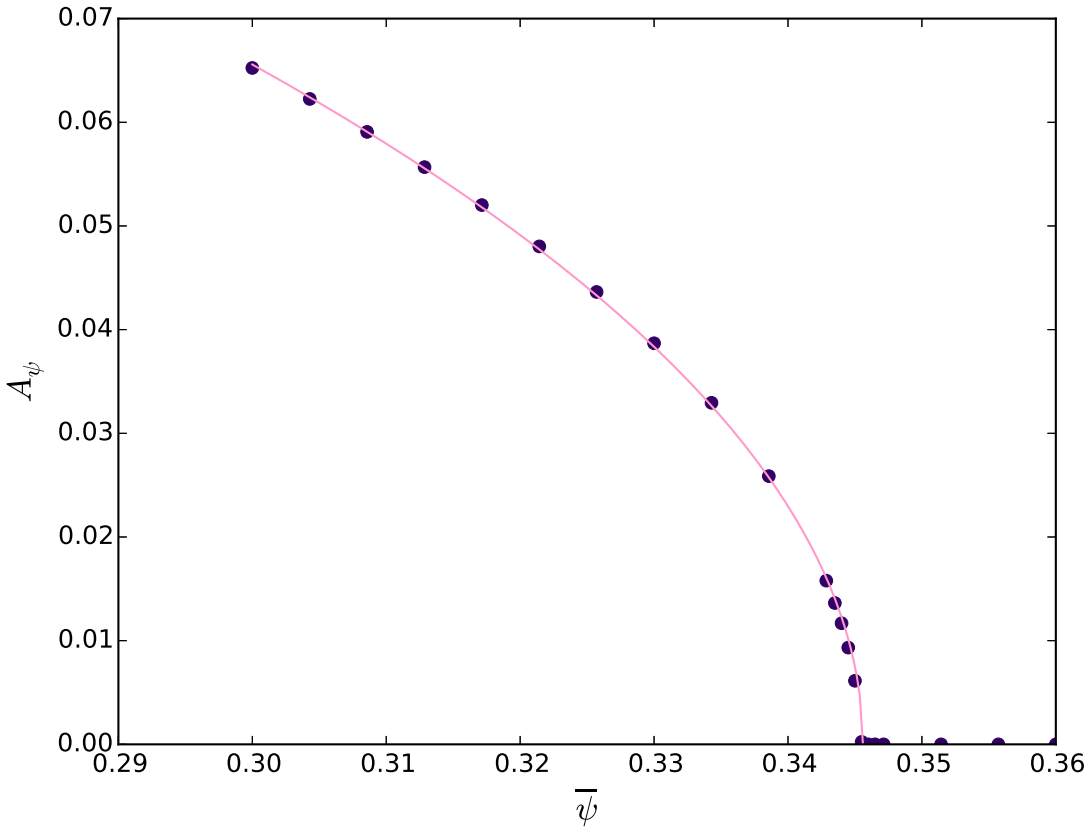


Figure 2.7. Plot of the order parameter for the uncoupled case as a function of $\bar{\psi}$ for $T = 0.01$ using parameters found in Table 2.2. The fit is to the function $A_\psi = A\sqrt{\bar{\psi}_c - \bar{\psi}}$, the function for a second-order mean-field transition as elaborated upon in section 2.3.

is the bulk free energy per volume. In order to ensure that the domain was sufficiently large compared to the APB correlation length, the critical exponents were also calculated by relaxation in a larger $2 \times 2 \times 96$ simulation domain, with critical exponents for $A_\psi$ and $\gamma$ only differing by $3.3 \times 10^{-3}$ and $1.4 \times 10^{-5}$ respectively compared to the smaller domain. Both of these exponents are consistent with the 1/2 and 3/2 exponents for $A_\psi$

and $\gamma$ respectively for an APB resulting from the simple Landau model

$$F = \int_V \left( \frac{r}{2}\eta^2 + \frac{u}{4}\eta^4 + \frac{K}{2}|\nabla\eta|^2 \right) d\mathbf{r}, \tag{2.35}$$

where $r \propto (T_c - T)$ and $u$ and $K$ are independent of temperature. This is not surprising, as the PFC method is a mean field model and has been shown to reduce to simple Landau models in appropriate limits [**81**]. Although comparison to this same Landau model would imply a critical exponent of -0.5 for $\xi$, unfortunately this exponent is difficult to determine. Because the critical exponent is highly sensitive to the method of fitting the $\psi$ profile, very small changes to the fitting methodology that only result in a few percent differences in the interface width give very different critical exponents. Because of a lack of a clear criteria for determining $\xi$, this critical exponent is left unreported.

As noted in section 2.1, all these results are dependent on the new definition of temperature. Using the original XPFC temperature parameter, both the critical exponents change, deviating more from mean field theory, and $R^2$ increases.

### 2.3.2. Grain Boundaries

As a further demonstration of the applicability of the this new method, ordering dynamics were investigated for symmetric tilt boundaries using the uncoupled model. The simulations were set up using the standard method for periodic grain boundaries [**80**]. The equilibrium density was determined by minimizing the energy with respect to $n$, and then initialized with Guassian noise for $\psi$ at T = 0.01 using the parameters in Table 2.2 except with $\alpha_\psi = 0.25$. The misorientation angle between the grains was 3.8°. The system first undergoes spinodal ordering. Then, domains grow and shrink in order to reduce the

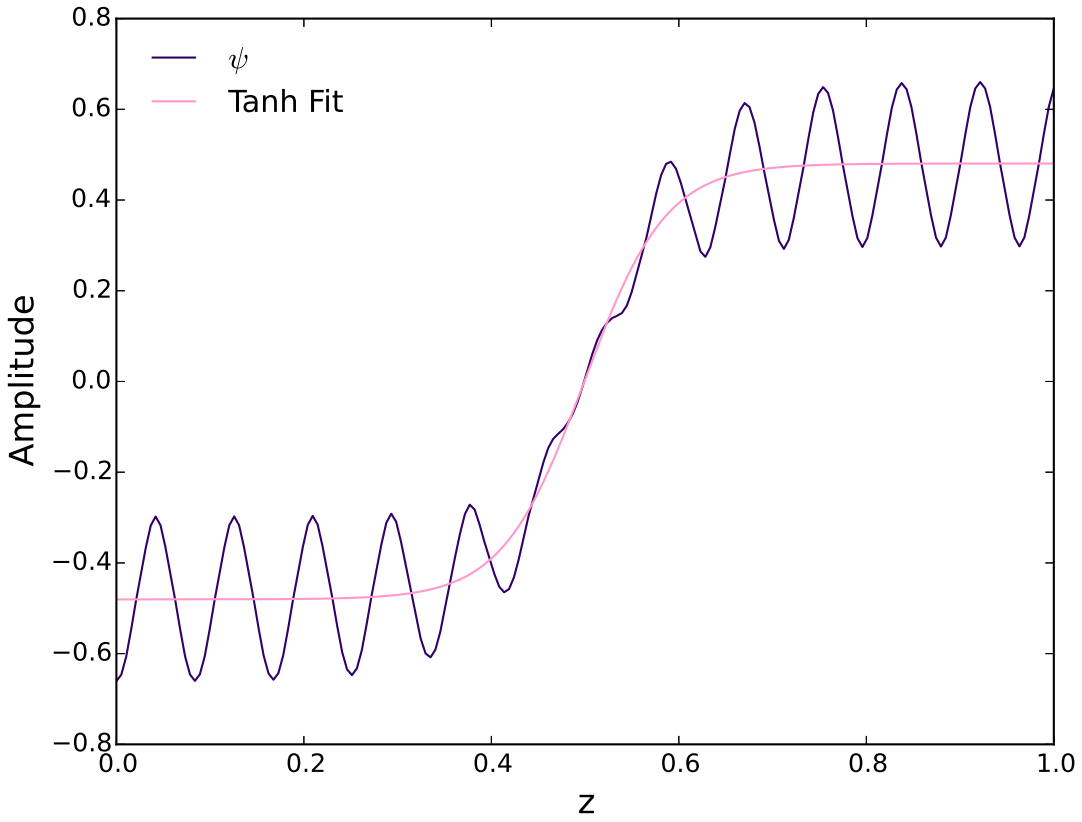


Figure 2.8. Demonstration of a tanh profile across an APB. The oscillating amplitude of $\psi$ along the edge of the unit cell (violet) and a tanh fit to Eq. (2.33) (pink) are plotted.

total APB energy. Interestingly, the model predicts that dislocation cores act as natural pinning points for APBs (Fig. 2.10). The dislocations pin the domain walls as excess disordered regions are created when a domain wall breaks free of the dislocation core.

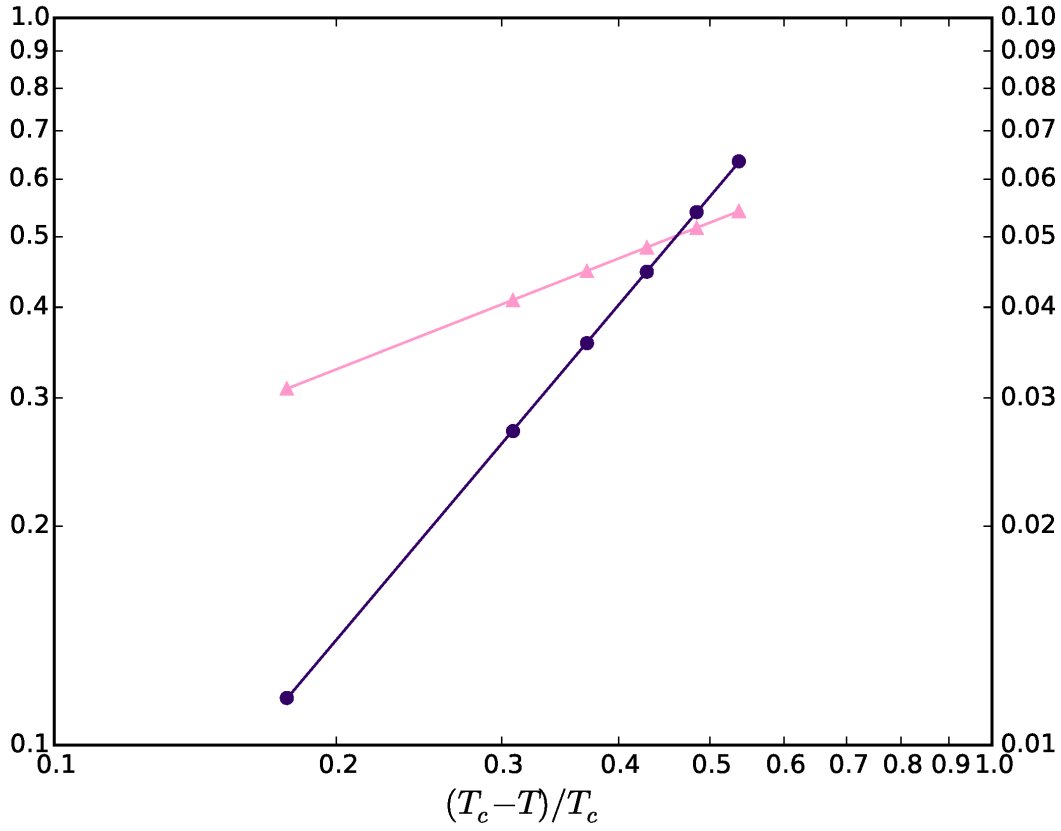


Figure 2.9. Scaling behavior of bulk order parameter, $A_\psi$ (left scale bar), and APB boundary energy, $\gamma$ (right scale bar), for temperatures near $T_c$.

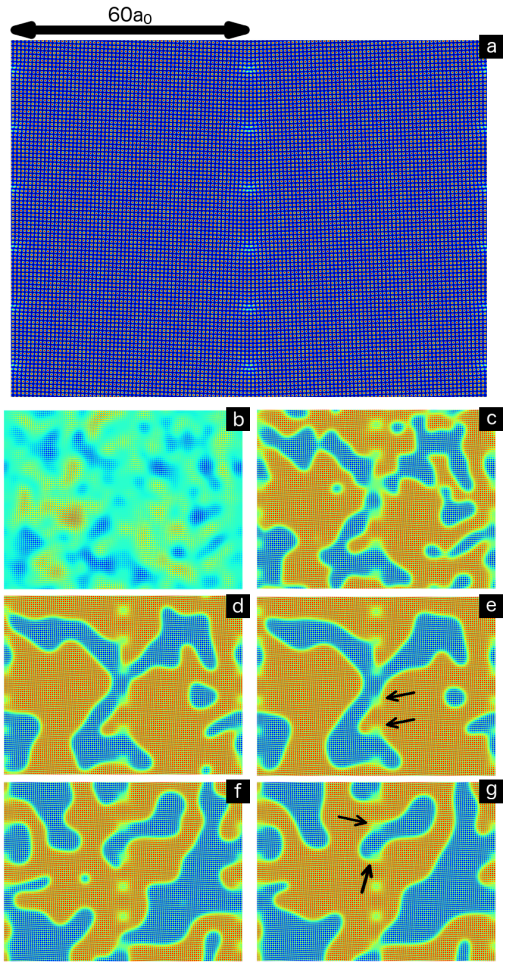


Figure 2.10. Images for dynamic ordering of a B2 crystal, showing an xy slice through the middle z coordinate. (a) shows the static $n$ field for the simulations with 3.8° misorientation between the two grains. After initializing the $\psi$ field with Gaussian noise, (b)-(e) show snapshots of $\psi$ at progressively later stages in the evolution. (b) shows spinodal ordering while (c)-(e) show coarsening. The green (white) disordered regions down the middle of (b)-(g) correspond to the edge dislocation cores in (a). Although much of the evolution can be understood through a simple reduction of mean curvature, the arrows point to examples of dislocation anchors that act to pin APB movement. The anchoring phenomenon was confirmed by initializing another simulation with the same conditions but a different set of random Gaussian noise to start, and two sample time steps from this second simulation are show in (f) and (g).

CHAPTER 3

# Complex Crystal Structures

In this chapter, we introduce a form for $C_3$ that stabilizes angles between specified crystallographic planes and can include multiple length scales, multiple preferred angles, and angles not restricted by Eq. (1.13).

## 3.1. Model

A free energy of the form

$$F[n] = F_1[n] + F_2[n] + F_3[n] \tag{3.1}$$

is assumed, where $F_1[n] + F_2[n]$ is Eq. (1.7), the XPFC model is used for the two-point correlation function, and $F_3$ is Eq. (1.11). The ansatz for $C_3$ is

$$\hat{C}_3(\boldsymbol{k}_1, \boldsymbol{k}_2) = \beta^2 R(k_1) R(k_2) \sum_{l=0}^{l_{\max}} \alpha_l P_l(\hat{\mathbf{k}}_1 \cdot \hat{\mathbf{k}}_2), \tag{3.2}$$

where $\hat{C}_3$ is the Fourier transform of the three-point correlation function, $k_i = |\boldsymbol{k}_i|$, $\hat{\mathbf{k}}_i = \boldsymbol{k}_i/|\boldsymbol{k}_i|$, $\beta$ is an interaction strength parameter, $R(k)$ is a real radial function, $P_l$ are the Legendre polynomials, and $\alpha_l$ are constant coefficients. As is explained later, $\alpha_l$ should be interpreted as determining the preferred interplanar angles. Because $\hat{C}_3(\mathcal{R}\boldsymbol{k}_1, \mathcal{R}\boldsymbol{k}_2) = \hat{C}_3(\boldsymbol{k}_1, \boldsymbol{k}_2)$ for any rotation matrix $\mathcal{R}$, $\hat{C}_3$ is rotationally invariant and so is $C_3$. By keeping the free energy rotationally invariant, it is possible to study phenomena such as solid-liquid

interfaces and grain boundary energies as a function of misorientation, which would be impossible otherwise.

This ansatz was chosen not only because it is rotationally invariant but also because the Legendre polynomials are both separable and form a complete orthogonal set. More explicitly, the separability of the Legendre polynomials means that

$$P_l(\hat{\mathbf{k}}_1 \cdot \hat{\mathbf{k}}_2) = \sum_{m=-l}^{l} \frac{4\pi}{2l+1} Y_{lm}(\hat{\mathbf{k}}_1) Y_{lm}(\hat{\mathbf{k}}_2), \tag{3.3}$$

where $Y_{lm}$ are the normalized real spherical harmonics [**82**]. Thus, $\hat{C}_3$ can be written as a sum of products of two-point correlation functions, i.e.,

$$\hat{C}_3(\boldsymbol{k}_1, \boldsymbol{k}_2) = \sum_{l=0}^{l_{\max}} \alpha_l (-1)^l \sum_{m=-l}^{l} \hat{C}^{(lm)}(k_1, \hat{\mathbf{k}}_1) \hat{C}^{(lm)}(k_2, \hat{\mathbf{k}}_2), \tag{3.4}$$

where

$$\hat{C}^{(lm)}(k, \hat{\mathbf{k}}) \equiv (-i)^l \sqrt{\frac{4\pi}{2l+1}} \beta R(k) Y_{lm}(\hat{\mathbf{k}}). \tag{3.5}$$

The factor of $(-1)^l$ in Eq. (3.4) was introduced to cancel the phase factors, $(-i)^l$, in Eq. (3.5) so that $C^{(lm)}$ is real (see Appendix B for details).

Substituting the inverse Fourier transform of Eq. (3.4) into Eq. (1.11) results in

$$F_3 = -\frac{1}{6} \sum_{l=0}^{l_{\max}} \alpha_l (-1)^l \sum_{m=-l}^{l} \int n(\boldsymbol{r}) \left( C^{(lm)} * n \right)^2 d\boldsymbol{r} \tag{3.6}$$

and

$$\frac{\delta F_3}{\delta n} = -\sum_{l=0}^{l_{\max}} \frac{\alpha_l (-1)^l}{6} \sum_{m=-l}^{l} \left\{ (C^{(lm)} * n)^2 + 2(-1)^l C^{(lm)} * [n (C^{(lm)} * n)] \right\}, \tag{3.7}$$

since $C^{(lm)}(-\boldsymbol{r}) = (-1)^l C^{(lm)}(\boldsymbol{r})$ by the parity property of real spherical harmonics (note the similarity between these expressions and Eq. 10 and Eq. 42 respectively from [**20**]).

Since the Legendre polynomials form a complete orthogonal set, if

$$B(x) \equiv \sum_{l=0}^{l_{\max}} \alpha_l P_l(x), \tag{3.8}$$

then each $\alpha_l$ is given by

$$\alpha_l = \frac{2l+1}{2} \int_{-1}^{1} B(x) P_l(x) dx. \tag{3.9}$$

This is convenient because it implies that the angular portion of Eq. (3.2) can represent any function through a series of Legendre polynomials.

The only task remaining is choosing $\beta$, $\hat{C}_2$, $R$, and $\alpha_l$ in order to produce the targeted structure. The $\beta$ constant is not strictly necessary since changing its value from unity is equivalent to modifying $R$. For convenience, however, $\beta$ was introduced in order to easily tune the relative strengths of the two- and three-point interactions. The parameters choices listed in Appendix A are motivated by considering diamond cubic and disordered $CaF_2$ as examples.

## 3.2. Structures

### 3.2.1. Diamond

First the diamond cubic crystal structure is considered. Since diamond cubic, like all crystal structures, is periodic, the density field can be expanded in a Fourier series, i.e.,

$$n(\boldsymbol{r}) = \bar{n} + \sum_j A_j e^{i\boldsymbol{k}_j \cdot \boldsymbol{r}}, \tag{3.10}$$

where $\bar{n}$, the average value of $n$, will be set to zero in all cases in this chapter for simplicity. When the diamond cubic structure is expressed on a simple cubic lattice, the atoms are located at both the fcc sites and the fcc sites translated by $(1/4, 1/4, 1/4)$, for a total of eight atoms per unit cell. If $\boldsymbol{k}$ is then expressed in terms of primitive reciprocal lattice vectors, i.e. $\boldsymbol{k} = \mathfrak{h}\hat{\mathbf{b}}_1 + \mathfrak{K}\hat{\mathbf{b}}_2 + \mathfrak{l}\hat{\mathbf{b}}_3$, the amplitudes for an atomic density represented by Dirac delta functions at the atomic positions are

$$A_{j(\mathfrak{h}\mathfrak{K}\mathfrak{l})} = \begin{cases} 8 & \text{if } \mathfrak{h} + \mathfrak{K} + \mathfrak{l} = 4N \\ & \text{and } \mathfrak{h},\ \mathfrak{K},\ \mathfrak{l} \text{ are all even} \\ 4(1+i) & \text{if } \mathfrak{h} + \mathfrak{K} + \mathfrak{l} = 4N + 1 \\ & \text{and } h,\ k,\ l \text{ are all odd} \\ 4(1-i) & \text{if } \mathfrak{h} + \mathfrak{K} + \mathfrak{l} = 4N + 3 \\ & \text{and } \mathfrak{h},\ \mathfrak{K},\ \mathfrak{l} \text{ are all odd} \\ 0 & \text{otherwise} \end{cases} \tag{3.11}$$

where $N$ is an integer.

The calculated amplitudes [Eq. (3.11)] are used to select the parameters of the model. First, the two-point correlation is discussed. Since the smallest set of reciprocal lattice vectors with nonzero amplitudes in Eq. (3.11) is the $\{111\}$ set,

$$\hat{C}_2(k) \equiv A_2 e^{-\frac{(k-q_1)^2}{2\sigma^2}}, \tag{3.12}$$

where $q_1 = 2\pi\sqrt{3}/a_0$, $A_2$ is a temperature-dependent parameter, $a_0$ is the lattice constant, and $\sigma$ is related to interfacial free energy, consistent with XPFC models [**13**, **14**, **18**, **27**].

To choose the parameters for the three-point correlation, consider the free energy resulting from it

$$F_3/V = -\frac{1}{6}\sum_{pqr} \hat{C}_3(k_p, k_q, \hat{\mathbf{k}}_p \cdot \hat{\mathbf{k}}_q) A_p A_q A_r \delta_{\boldsymbol{k}_p+\boldsymbol{k}_q+\boldsymbol{k}_r,\mathbf{0}}. \tag{3.13}$$

Notice that the only nonzero contributions to this energy come from groups of vectors, $[\boldsymbol{k}_p, \boldsymbol{k}_q, \boldsymbol{k}_r]$, that satisfy both $\hat{C}_3(k_p, k_q, \hat{\mathbf{k}}_p \cdot \hat{\mathbf{k}}_q) \neq 0$ and $\boldsymbol{k}_p + \boldsymbol{k}_q + \boldsymbol{k}_r = \mathbf{0}$. From Eq. (3.2), it is clear that $\hat{C}_3$ is nonzero only when both $R(k_p)$ and $R(k_q)$ are nonzero. Consequently, $R(k)$ can be interpreted as a weighting factor for wave vector magnitudes, like $\hat{C}_2$. Therefore, it is convenient to define $R$ in a similar manner as $\hat{C}_2$ was defined. For diamond and most other crystal structures, $R(k) = \hat{C}_2(k)$ [given by Eq. (3.12)] was found to work well. In the limit of small $\sigma$ for this choice of $R$, only groups where the first two wave vectors are of magnitude $q_1$ can contribute to the three-point term of the free energy. Since the $\boldsymbol{k}_p + \boldsymbol{k}_q + \boldsymbol{k}_r = \mathbf{0}$ condition must also be satisfied, only groups like $[(111), (111), (\bar{2}\bar{2}\bar{2})]$, $[(111), (11\bar{1}), (\bar{2}\bar{2}0)]$, and $[(111), (1\bar{1}\bar{1}), (\bar{2}00)]$ contribute to the free energy. However, wave vectors of type $(\bar{2}\bar{2}\bar{2})$ and $(\bar{2}00)$ have zero amplitude for the diamond structure [see Eq. (3.11)]. This leaves only groups equivalent to $[(111), (11\bar{1}), (\bar{2}\bar{2}0)]$ as contributors to the

three-point term (e.g., $[(1\bar{1}\bar{1}), (\bar{1}\bar{1}\bar{1}), (022)]$ would be another example of a contributing group). It can be shown that for these groups, $\hat{\mathbf{k}}_p \cdot \hat{\mathbf{k}}_q = 1/3$, or equivalently, the angle between the $p$ and $q$ planes is $\cos^{-1}(1/3) \simeq 70.5°$. Also note that, for these groups, the product $A_p A_q A_r$ is always positive [see Eq. (3.11)]. Consequently, by choosing the coefficients $\alpha_l$ in Eq. (3.2) in such a way that $\hat{C}_3$ is positive when $\hat{\mathbf{k}}_p \cdot \hat{\mathbf{k}}_q = 1/3$ and zero otherwise, we energetically promote the angle $\cos^{-1}(1/3)$, corresponding to the angle between $\{111\}$ planes. One simple way to do so is for $B$ in Eq. (3.9) to be a delta function centered at $x = 1/3$. Namely, we take

$$\alpha_l = \frac{2l+1}{2} \int_{-1}^{1} \delta(x - 1/3) P_l(x) dx = \frac{2l+1}{2} P_l(1/3). \tag{3.14}$$

Trial-and-error is required for determining how many terms are necessary. For this case, we found that $l_{\max} = 3$ was sufficient. To demonstrate that diamond cubic is likely the equilibrium structure, it was tested against bcc, fcc, simple cubic, hexagonal rods, hcp, disordered $CaF_2$, graphene rods, simple hexagonal, simple cubic rods, and stripes [**18**]. To test for the equilibrium phase, an initial condition is set up so that it approximates a possible structure in a unit cell of the appropriate size, and then the energy is minimized through standard conserved nonlocal dynamics [**80**],

$$\frac{\partial n}{\partial t} = -\frac{\delta F}{\delta n} + \frac{1}{V} \int_V \frac{\delta F}{\delta n} d\boldsymbol{r}. \tag{3.15}$$

Out of the structures that were tested, diamond cubic was the one with the lowest energy. However, because only a finite number of structures can be examined, this does not prove that the global minimum energy structure was found. Nonetheless, it was also observed that if a system of size $4 \times 4 \times 4$ unit cells is initialized with noise, a diamond cubic

structure forms. Although using purely the dynamics of Eq. (3.15) results in the structure becoming kinetically trapped in a high-energy, low-amplitude state (i.e., the evolution toward equilibrium is very slow), the dynamics can be accelerated by multiplying the amplitude of the high-energy structure by a large factor (on order of 500), after which the diamond cubic phase quickly appears when the system is relaxed, regardless of the seed used to generate the initial random condition. The formation of the diamond structure without any *a priori* information about the equilibrium state, except through the periodic boundary conditions, suggests that there are no unaccounted for lower energy phases.

### 3.2.2. $CaF_2$

As a second example, the case of a single-component $CaF_2$ model is presented. Consider a simple cubic lattice with atoms at the fcc positions and at the tetrahedral voids. The amplitudes for this structure are

$$A_{j(\mathfrak{hkl})} = \begin{cases} 12 & \text{if } \mathfrak{h}+\mathfrak{k}+\mathfrak{l}=4N \\ & \text{and } \mathfrak{h},\ \mathfrak{k},\ \mathfrak{l} \text{ are all even} \\ 4 & \text{if } \mathfrak{h},\ \mathfrak{k},\ \mathfrak{l} \text{ are all odd} \\ -4 & \text{if } \mathfrak{h}+\mathfrak{k}+\mathfrak{l}=4N+2 \\ & \text{and } \mathfrak{h},\ \mathfrak{k},\ \mathfrak{l} \text{ are all even} \\ 0 & \text{otherwise.} \end{cases} \tag{3.16}$$

Notice that this structure has nonzero amplitudes for the same ($\mathfrak{hkl}$) (i.e., has the same extinction symbol [**83**]) as fcc but with different amplitude values. Since the energy from

the two-point interaction term is a function of only the magnitudes of the amplitudes and not their phase, it is difficult, and maybe impossible, to generate a two-point correlation that is able to stabilize this structure over fcc and bcc. However, discerning between the fcc and $CaF_2$ structures is possible using a three-point correlation. Like for diamond cubic, $R(k) = A_2 e^{-\frac{(k-q_1)^2}{2\sigma^2}}$ where $q_1 = 2\pi\sqrt{3}/a_0$. This selects the first nonzero reciprocal lattice vector (the $\{111\}$ planes). Using this $R$, there are groups with two relevant angles, unlike the diamond cubic case: $[(111), (11\bar{1}), (\bar{2}\bar{2}0)]$ type groups with $\boldsymbol{k}_p \cdot \boldsymbol{k}_q = 1/3$ and $[(111), (1\bar{1}\bar{1}), (\bar{2}00)]$ groups with $\boldsymbol{k}_p \cdot \boldsymbol{k}_q = -1/3$. For the former, $A_p A_q A_r > 0$, and for the latter, $A_p A_q A_r < 0$. Consequently, Eq. (3.9) becomes

$$\alpha_l = \frac{2l+1}{2}(-P_l(-1/3) + P_l(1/3)). \tag{3.17}$$

For this case, $l_{\max} = 5$ was sufficient for $B(x)$ to produce a peak at $\pm 1/3$ (see Fig. 3.1). However, among the structures examined, the lowest energy state with this $l_{\max}$ was found to be an "inverse" bcc structure (i.e., $-n$ has a bcc structure), rather than the single-component $CaF_2$ structure. This occurs because inverse bcc has contributing groups equivalent to $[(110), (\bar{1}0\bar{1}), (0\bar{1}1)]$, like bcc, and these groups have $\boldsymbol{k}_p \cdot \boldsymbol{k}_q = -1/2$. When $l_{\max} = 5$, $B(x)$ has a broad peak and $B(-1/2) \simeq B(-1/3)$, so the same symmetry reasons that normally prefer bcc over fcc in this case prefer inverse bcc over the single-component $CaF_2$ structure [**84**]. Consequently, the peaks were narrowed with $l_{\max} = 13$, in which case the $CaF_2$ structure is the energy minimum among all structures examined. Although $l_{\max} = 13$ at first might appear computationally expensive, it can be evaluated efficiently because every convolution term can be computed in parallel.

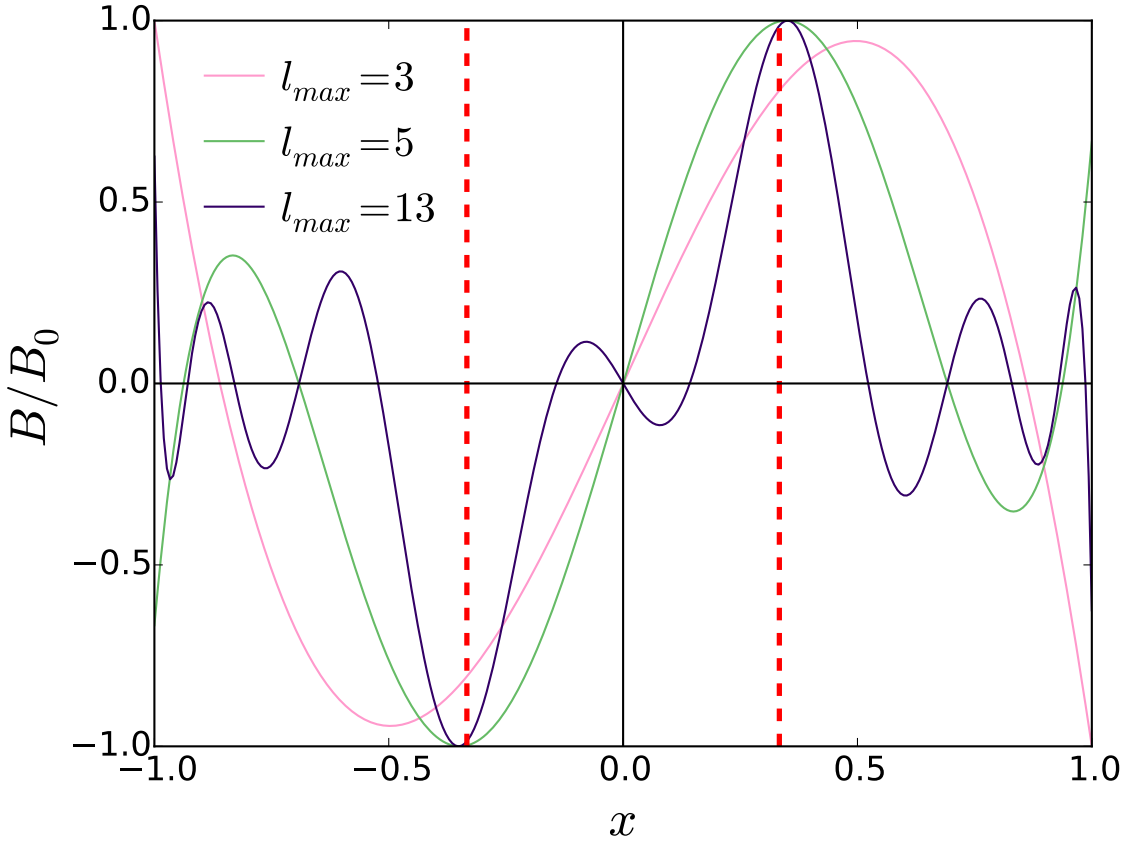


Figure 3.1. Plot of $B(x)$ for $l_{\max} = 3$, 5, and 13, normalized to their maximum values. For $l_{\max} < 5$, the functions' peaks are not close to $\pm 1/3$, marked by the vertical dashed lines. Although the peaks for $l_{\max} = 5$ are on target, the wide breadth of peaks includes the values $\pm 1/2$. In contrast, $l_{\max} = 13$ has sharp, centered peak with close to zero baseline.

A similar approach was employed to identify the parameters for the simple hexagonal, simple cubic, and $X_3$ structures, in addition to graphene layers. All crystal structures were found to be lower in energy than all the compounds listed previously in connection with diamond cubic. Additionally, $CaF_2$ spontaneously ordered from noise, and the rest (except $X_3$, which spontaneously ordered to a higher energy phase) ordered from noise

with the aforementioned method to accelerate the kinetics. A full listing of parameters used is contained in Appendix A.

### 3.2.3. Perovskite

As a capstone demonstration, the single-component three-point correlations are combined to construct a simple PFC model for perovskite (Fig. 3.2) where the only interaction coupling the components is an excluded volume term. Since the model does not include electrostatic interactions, the structure is equivalent to antiperovskite as well. The free energy of this model is given by

$$F[n_A, n_B, n_X] = F_A[n_A] + F_B[n_B] + F_X[n_X] + Z\int_V (n_A n_B + n_A n_X + n_B n_X) d\boldsymbol{r}, \tag{3.18}$$

where $F_A$ and $F_B$ are simple cubic single-component free energies, $F_X$ is the free energy for $X_3$, and $Z > 0$. Note that each of the single-component free energies are of the form given by Eq. (1.10). If the parameters for $A$ and $B$ are the same, there is no driving force for the $B$ atoms, rather than the $A$ atoms, to have a coordination number of six. To break this symmetry, the radii of the $B$ isosurfaces were made smaller (as in the actual perovskite structure). A small $Z$ was found to be sufficient for the perovskite structure to be an energy minimum and be able to spontaneously order from noise (parameters are given in Appendix A).

There are many potential ways in which the method introduced above can be applied in future research. For all of the particular structures described, information including their elastic properties, surface energies, and grain boundary morphologies are of interest. For example, the perovskite model could be used to model chemical vapor deposition

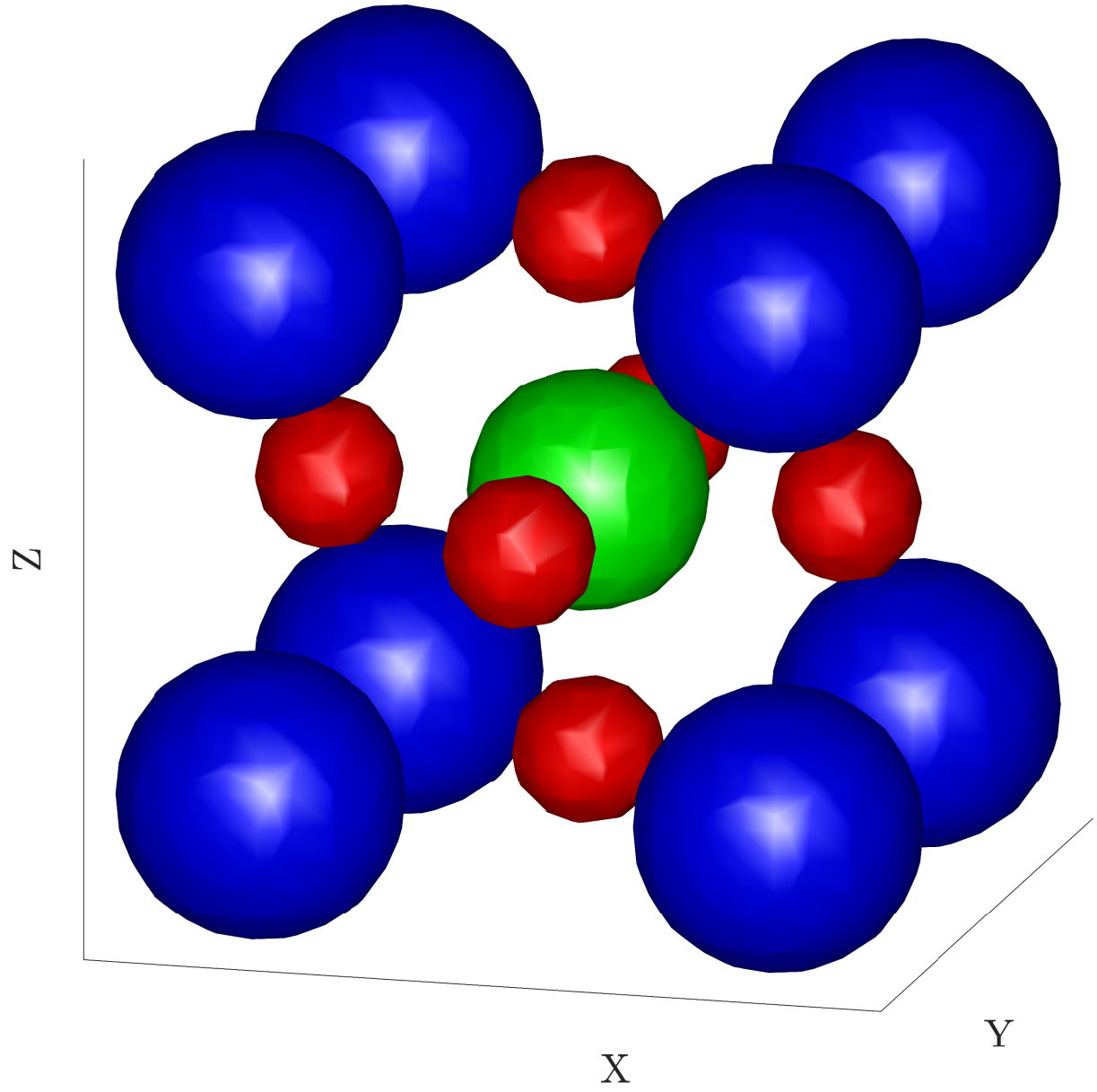


Figure 3.2. Three-dimensional isosurface plot of equilibrated cubic perovskite using Eq. (3.18). For the canonical $ABX_3$ perovskite, blue $A$ atoms are at the corners and a green $B$ atom is at the center surrounded by six red $X$ nearest-neighbors.

grown perovskite solar cells [**85**]. Other potential applications include combining this model with the PFC ordering model [**27**] to create a two-component $CaF_2$ model for

modeling $\theta'$ precipitates in Al-Cu alloys, combining it with a vapor phase model [**86**, **87**] to create a 3D single layer graphene model, and extending it to other complex phases such as Heusler alloys and Laves phases.

CHAPTER 4

# Displacive phase transitions

## 4.1. Introduction

A ferroelectric is a material whose spontaneous electric polarization is reversible upon application of an external electric field. Ferroelectricity can be modeled highly phenomologically with models such as Landau-Ginzburg-Devonshire (LGD) theory [**43**], as well as with more first-principles based approaches, such as quantum density functional theory [**88**]. As discussed in Sec. 1, previous ferroelectric PFC modeling followed the phenomological approach and included the LGD polarization terms in the free energy explicitly, i.e. $F[n, p]$ [**51**]. In contrast, this chapter introduces a more fundamental PFC ferroelectric model, where the polarization is not explicitly modeled but rather is an emergent property of a displacive phase transition.

Displacive phase transitions are phase transitions in which small motions of atoms change the symmetry of the crystal structure. Initially, the crystal has some particular symmetry, and then that symmetry is lost. For example in Fig. 4.1, the plane group is $p4mm$, but following a displacive phase transition, Fig. 4.2, the plane group is $p1m1$. The consequent polarization is then calculated from the amount of atomic displacement and is a coarse-grained property of the unit cell.

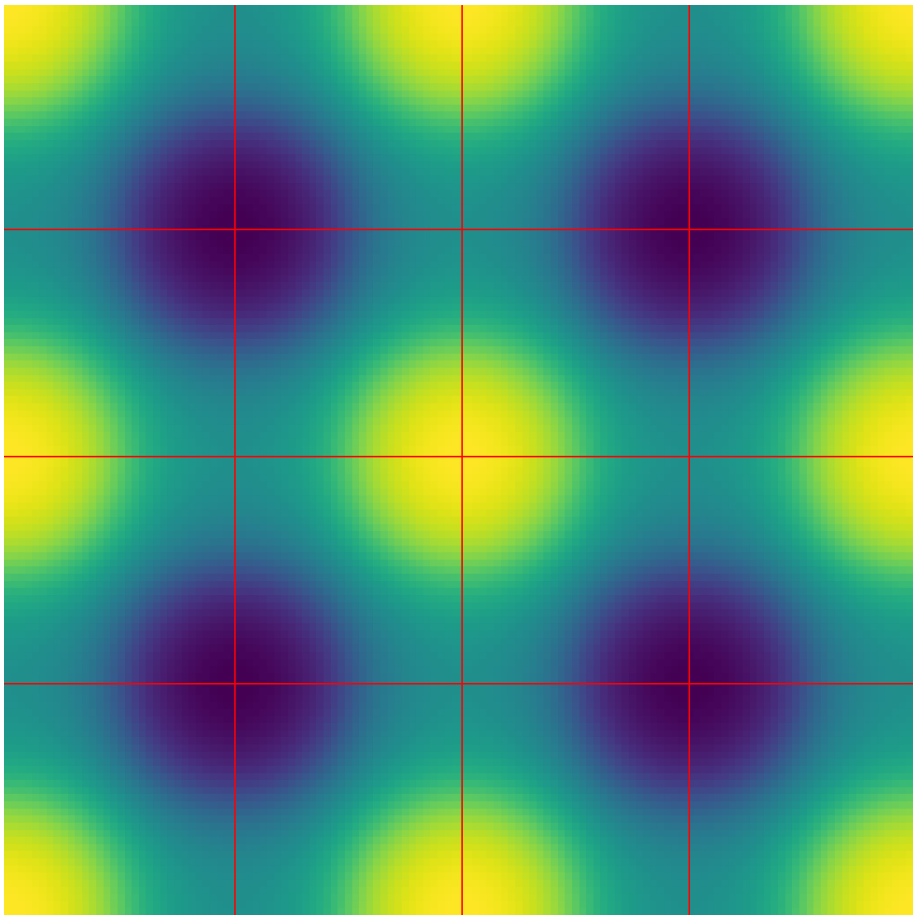

Figure 4.1. Plot of the unpolarized states in the two-component square crystal model. The yellow regions (corners and center) are sites for component $A$, and the dark-blue regions are sites for component $B$. The red lines are visual aids to show symmetries of the unit cell.

## 4.2. Model Formulation

In general, the free energy of a two-component system can be decomposed into the free energies of the individual components, $F_i$, plus an interaction correction, $F_{AB}$. Namely,

$$F[n_A, n_B] = F_A[n_A] + F_B[n_B] + F_{AB}[n_A, n_B] \tag{4.1}$$

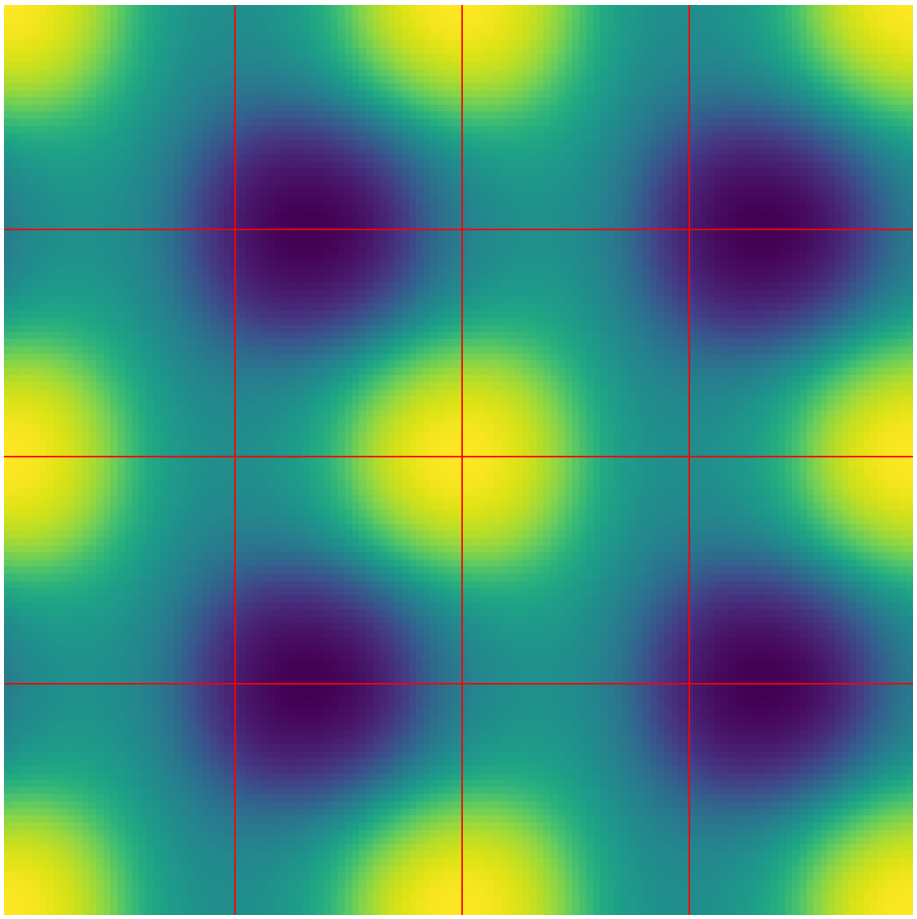

Figure 4.2. Plot of the [10] polarized state in the two-component square crystal model.

where $F$ is the total nondimensionalized free energy. The nondimensionalized atomic density for component $i$, $n_i$, is defined by

$$n_i = \frac{\rho_i - \rho_{i,0}}{\rho_{i,0}}, \tag{4.2}$$

where $\rho_i$ is the actual atomic number density and $\rho_{i,0}$ is the reference atomic number density. In general, $F_A$ and $F_B$ could be any one component free energy model, involving

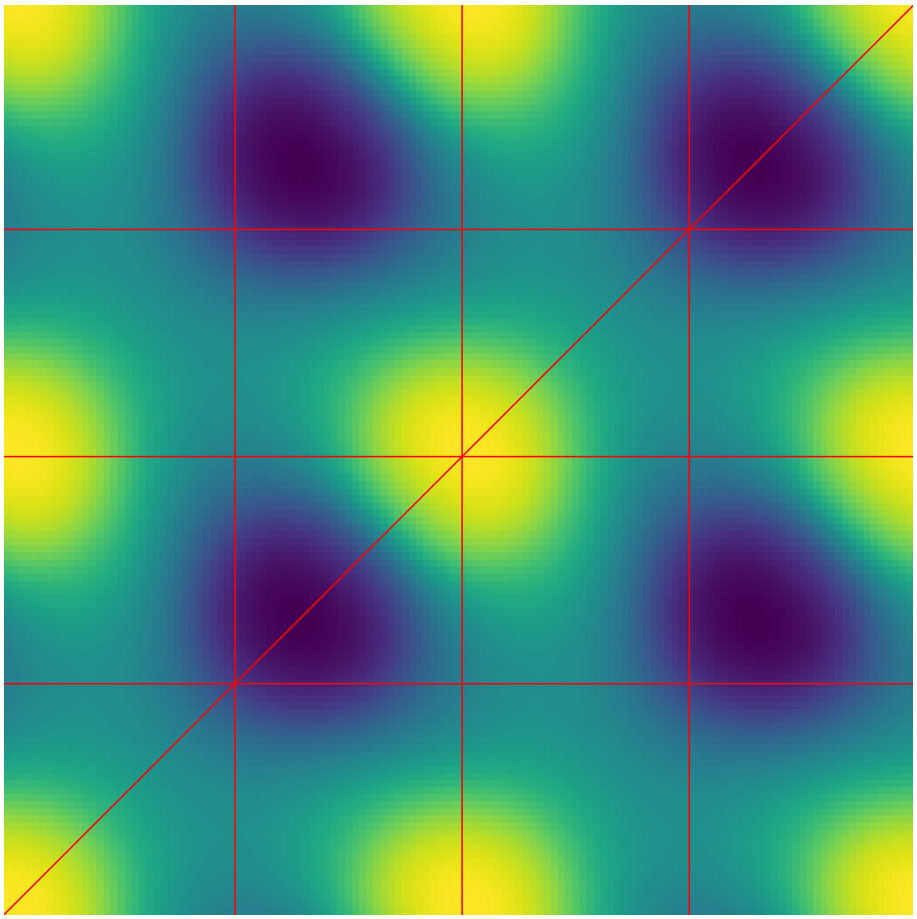

Figure 4.3. Plot of the [11] polarized state in the two-component square crystal model.

either only two-point [**6**, **14**] or also three-point [**20**, **23**, **27**] interactions. For simplicity, in this chapter $F_A[n_A]$ and $F_B[n_B]$ will be identical XPFC models in the form of Eq. (1.7) [**13**, **14**]. The correlation function itself is defined in Fourier space such that

$$\hat{C}_A(q) = \hat{C}_B(q) = \max_j \left( b_j e^{\frac{-(q-q_j)^2}{2\sigma_j^2}} \right) \tag{4.3}$$

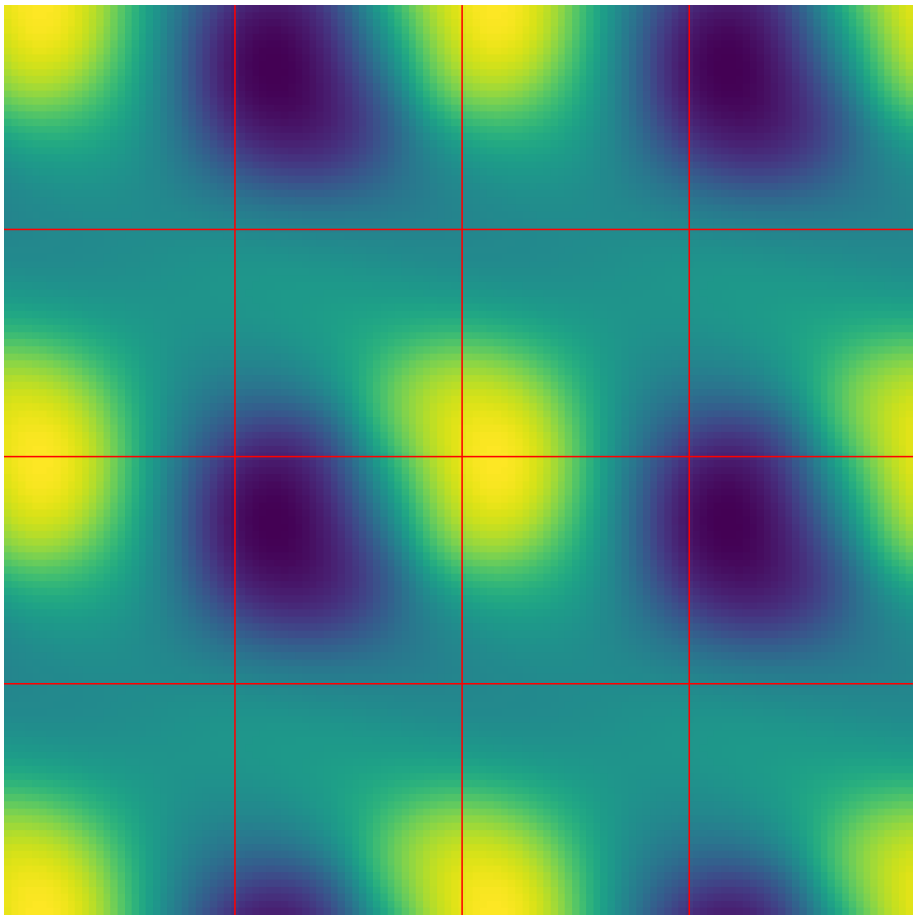

Figure 4.4. Plot of the "generic" polarized state in the two-component square crystal model.

where $\hat{C}_i$ is the Fourier transform of the isotropic two-point correlation function for component $i$, $q = |\boldsymbol{q}|$, $q_j$ are constants that determine the crystal structure, $\sigma_j$ are standard deviations that control the elastic constants, and $b_j$ are positive numbers connected to the system temperature [**14**].

### 4.2.1. Symmetric Transitions

The simplest method for modeling exact intermetallics is to, following Taha *et al.*, Taylor expand $F_{AB}$ in the variables $n_A$ and $n_B$. To fourth-order, for the symmetric $n_A$ and $n_B$ components

$$F_{AB} = \int_V [\alpha_2 n_A n_B + \alpha_3 (n_A n_B^2 + n_A^2 n_B) + \frac{\alpha_4}{2} n_A^2 n_B^2 + \alpha_5 (n_A^3 n_B + n_A n_B^3)] d\boldsymbol{r}. \tag{4.4}$$

For additional simplicity, $\alpha_5 = 0$ henceforth. To explain why Eq. (4.4) is sufficient for polarization, Landau models for the one-dimensional and two-dimensional cases will be explained.

**4.2.1.1. One-dimensional crystal.** Consider the case where the single-component correlation function [Eq. (4.3)] is only a single Gaussian with a peak at wavenumber $q_1 = 2\pi/a$, where $a$ is the lattice constant. In one dimension, the polarization imagined is shown in Fig. 4.5. The blue and red curves are the same shape but are phase shifted relative to each other. In the unpolarized state, the relevant phase shift, $\Delta x$, between the two waves is exactly $a/2$. In the polarized state on the other hand, the phase shift $\Delta x = a/2 + \delta$, where $\delta$ is the nonzero displacement from the centrosymmetric position.

The conditions for when a displacive phase transition occurs can be understand in terms of one-dimensional Landau theory. Since the single-component correlation function contains only a single peak, it is reasonable to use a one mode expansion for $n_i$. Namely,

$$n_A(x) = \bar{n}_A + A e^{iq_1 x} + A^* e^{-iq_1 x} \tag{4.5}$$

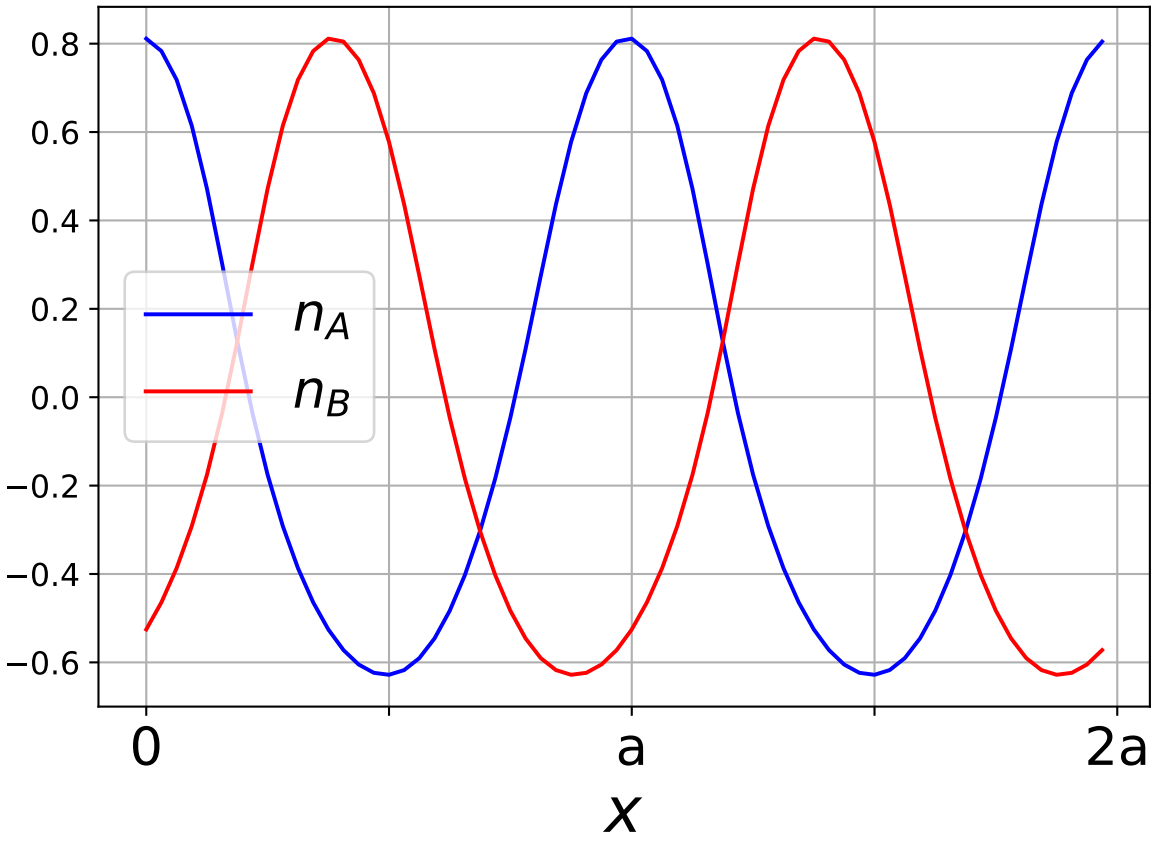


Figure 4.5. Numerical simulation demonstrating polarization in one dimension.

and

$$n_B(x) = \bar{n}_B + Be^{iq_1 x} + B^* e^{-iq_1 x}, \tag{4.6}$$

where $A$ and $B$ are the amplitudes, $A^*$ and $B^*$ are the complex conjugates of $A$ and $B$, and $\bar{n}_A = \bar{n}_B$ to ensure charge neutrality. For the duration of this article, $\bar{n}_A = 0$ for simplicity. Since $F[n_A, n_B] = F[n_B, n_A]$, it is assumed that $|A| = |B|$. This is equivalent

to assuming that $n_B$ is a phase shifted copy of $n_A$. Consequently, $B$ can be expressed as

$$B = Ae^{iq_1\Delta x}. \tag{4.7}$$

Since $F_A$ and $F_B$ are independent of $\Delta x$, only Eq. (4.4) must be minimized to find the conditions for polarization. Plugging in Eq. (4.5) and Eq. (4.6) into Eq. (4.4) in the simplified $\alpha_3 = 0$ case results in

$$\frac{F_{AB}}{a} = -2\alpha_2|A|^2\cos(q_1\delta) + \alpha_4|A|^4[2 + \cos(2q_1\delta)]. \tag{4.8}$$

From Eq. (4.8) it is clear why $\alpha_4$ is necessary; without it, $\delta = 0$ or $\delta = a/2$ (depending on the sign of $\alpha_2$). The polarization phenomena occurs because with $\alpha_2 > 0$, the $n_An_B$ term favors $\delta = 0$ while the $n_A^2n_B^2$ term favors $\delta = \pm a/4$. This competition drives a displacive phase transition. More precisely, there is polarization when $\alpha_2, \alpha_4 > 0$ and

$$\frac{\alpha_2}{\alpha_4|A|^2} < 2, \tag{4.9}$$

with the value of the displacement itself being

$$\delta = \frac{1}{q_1}\cos^{-1}\frac{\alpha_2}{2\alpha_4|A|^2}. \tag{4.10}$$

The polarization condition, Eq. (4.9), can also be derived by Taylor expanding Eq. (4.8)

$$\begin{aligned}\frac{F_{AB}}{a|A|^2} \approx &(-2\alpha_2 + 3\alpha_4|A|^2) + q_1^2(\alpha_2 - 2\alpha_4|A|^2)\delta^2 + \\ &q_1^4(-\frac{\alpha_2}{12} + \frac{2}{3}\alpha_4|A|^2)\delta^4.\end{aligned} \tag{4.11}$$

As usual for a single order parameter quartic Landau model, the equilibrium phase just depends on the sign of the quadratic term. The connection between the displacement $\delta$ and the polarization $p$ is discussed in Appendix C but is generally of the form

$$p = \tilde{Q}\delta. \tag{4.12}$$

**4.2.1.2. Two-dimensional polarization.** Unlike in one dimension, in two dimensions there are many possible polarization directions. In this work, only a square crystal is considered for simplicity. In the unpolarized state (Fig. 4.1), the phase shift, $\Delta\boldsymbol{r}$, between $n_A$ and $n_B$ is $(a/2, a/2)$. In the polarized state (Fig. 4.2–4.4), the $n_B$ peaks are off-center, i.e. $\boldsymbol{\delta} = \Delta\boldsymbol{r} - (a/2, a/2) = (\delta_x, \delta_y)$ is nonzero.

To understand the polarization process, Landau theory analysis like in 1D is performed. Unfortunately, it is more difficult. Since the square crystal structure is two-dimensional and cannot be stabilized by a single frequency [**13**, **14**], now $n_i$ are expressed as more general Fourier series. Namely,

$$n_A(\boldsymbol{r}) = \sum_{hk} A_{hk} e^{i\boldsymbol{q}_{hk}\cdot\boldsymbol{r}} \tag{4.13}$$

and

$$n_B(\boldsymbol{r}; \Delta\boldsymbol{r}) = \sum_{hk} A_{hk} e^{i\boldsymbol{q}_{hk}\cdot(\boldsymbol{r}+\Delta\boldsymbol{r})}, \tag{4.14}$$

where

$$\boldsymbol{q}_{hk} = h\hat{\mathbf{b}}_1 + k\hat{\mathbf{b}}_2 \tag{4.15}$$

is a reciprocal lattice vector of the crystal, $h$ and $k$ are integers, and $\hat{\mathbf{b}}_i$ is the $i$th primitive reciprocal lattice vector. It is worth noting that during numerical simulations, it was discovered that the approximation of Eq. (4.7) and Eq. (4.14) is not exactly true. Meaning, $n_B$ is not exactly a phase shifted copy of $n_A$, and given the numerical $n_A$, there is no $\Delta\boldsymbol{r}$ that exactly solves Eq. (4.14) for all amplitudes. For simplicity however, the approximation that a single parameter, the phase shift vector $\Delta\boldsymbol{r}$, can map $A_{hk}$ to $B_{hk}$ is made.

In addition to the phase shift approximation, there are other complications when converting this model into a Landau model like in one dimension. Since the unpolarized state is a member of the plane group $p4mm$, there are eight general Wyckoff positions denoting equivalent positions in the unit cell, and these real-space symmetries correspond to symmetries in the amplitudes [**83**]. If the Fourier series in Eq. (4.13) has its origin at the corner of a unit cell, one example equivalency is that

$$n_A(x,y) = n_A(x,-y) \implies A_{hk} = A_{h\bar{k}}, \tag{4.16}$$

This analysis for all Wyckoff positions implies that all $A_{\{hk\}}$ are equal, where $\{\cdot\}$ denotes a family of $hk$ pairs created by the permutation and negation of the internal elements (e.g., $\{12\}$ includes eight pairs: 12, $\bar{1}\bar{2}$, $1\bar{2}$, $\bar{1}2$, 21, $\bar{2}\bar{1}$, $2\bar{1}$, $\bar{2}1$). When the structure polarizes in the [10] direction however, the plane group changes to $p1m1$. This plane group has only two general Wyckoff positions, and the only amplitude symmetry is that $A_{hk} = A_{\bar{h}k}$. Consequently, $A_{10} = A_{\bar{1}0}$ but $A_{10} \neq A_{01}$ in general, which further complicates the analytical free energy expression. For simplicity however, this complication is neglected as $A_{10} \approx A_{01}$ still.

With these caveats, the bulk analytical free energy, $F_{AB}$, as a function of two modes $A_1 = A_{\{10\}}$ and $A_2 = A_{\{11\}}$ with $\alpha_3 = \alpha_4 = 0$ is

$$\frac{F_{AB}}{\alpha_2 \mathcal{A}} = -2A_1^2\Big(\cos(q_1\delta_x) + \cos(q_1\delta_y)\Big) + 2A_2^2\Big(\cos[q_1(\delta_x+\delta_y)] + \cos[q_1(\delta_x-\delta_y)]\Big), \tag{4.17}$$

or in Taylor expanded form

$$\begin{aligned}\frac{F_{AB}}{\alpha_2\mathcal{A}} =& 4(-A_1^2 + A_2^2) + q_1^2\tilde{Q}^2(A_1^2 - 2A_2^2)(p_x^2 + p_y^2) + q_1^4\tilde{Q}^4\Big(-\frac{1}{12}A_1^2 + \frac{A_2^2}{6}\Big)(p_x^4 + p_y^4) \\ &+ q_1^4\tilde{Q}^4 A_2^2 p_x^2 p_y^2 \qquad (4.18)\\ &= F_{AB,0} + \frac{1}{2}\alpha(p_x^2 + p_y^2) + \frac{1}{4}[\gamma_{11}(p_x^4 + p_y^4) + \gamma_{12}p_x^2 p_y^2]. \qquad (4.19)\end{aligned}$$

Equation (4.18) is exactly the fourth-order Landau free energy for a two-component spin system with cubic anisotropy [**89**]. This is interesting because in general when constructing phenomenological Landau models, one must be careful to only include terms that have the same symmetries as the crystal under study. Because the PFC model has the crystal structure built-in, the resulting Landau model automatically contains only the terms with the correct symmetries.

Landau theory can be used to understand not only the existence of displacive phase transitions but also their direction. In Eq. (4.18), if $\gamma_{12} > 2\gamma_{11}$, then if polarization occurs it will be in the $\langle 10\rangle$ direction (Fig. 4.2) [**89**]. (N.B., $\langle\cdot\rangle$ denotes a family of real variables in the same manner that $\{\cdot\}$ denotes a family of reciprocal space variables.) If $\gamma_{12} < 2\gamma_{11}$ on the other hand, then any polarization will be in the $\langle 11\rangle$ direction (Fig. 4.3) [**89**]. Parameters were found such that both $\langle 11\rangle$ and $\langle 10\rangle$ polarizations occur in numerical simulation, using $\alpha_3 = 0$ and $\alpha_3 \neq 0$ respectively (Fig. 4.3 and 4.2). In the normal

Table 4.1. Table of parameter values for {10} polarizing model.

| Quantity | Value |
|---|---|
| $b_1$ | 1.0 |
| $b_2$ | 0.98 |
| $q_1$ | $2\pi$ |
| $q_2$ | $2\pi\sqrt{2}$ |
| $\sigma_1$ | 2.0 |
| $\sigma_2$ | 2.0 |
| $\alpha_2$ | 0.01 |
| $\alpha_3$ | 0.05 |
| $\alpha_4$ | 0.05 |
| $\alpha_5$ | 0 |
| $a_0$ | 1.0 |
| $\bar{n}$ | 0 |

parameter space of the single component PFC model, the quadratic coefficient $\alpha$ in Eq. (4.18) is always positive, so polarization does not occur. Parameters that analytically minimize the free energy and give $\langle 10 \rangle$ polarizations do exist but require $\alpha_3, \alpha_4 \neq 0$ and an $A_{\{20\}}$ mode. For brevity, this full expression is emitted.

### 4.2.2. Generic Polarization

In order to model polarization in an arbitrary direction, the free energy

$$F_{AB} = \int_V n_A^m C_{AB} * n_B^m d\boldsymbol{r}, \tag{4.20}$$

where $m$ is a positive integer, is used in place of Eq. (4.4). The possibility of a displacive phase transition to an "arbitrary" direction is motivated by the fact that although such a polarization is impossible in fourth-order Landau theory, it is possible in eighth-order

Landau theory [**89**]. Equation (4.20) itself is phenomenologically motivated, and presumably, additional terms where the powers for $n_A$ and $n_B$ are not the same could give rise to additional behavior. In the simple case of a displacive transition in the square crystal, this term is sufficient to describe *all* possible polarization states consistent with the plane group. Plugging in Eqs. (4.13) and (4.14) into Eq. (4.20) gives

$$\frac{F_{AB}(\Delta \boldsymbol{r})}{\mathcal{A}} = \sum_{h_1 k_1, \ldots, h_m k_m, \mathfrak{h}_1 \mathfrak{K}_1, \ldots, \mathfrak{h}_m \mathfrak{K}_m} \prod_{\alpha=1}^{m} A_{h_\alpha k_\alpha} A_{\mathfrak{h}_\alpha \mathfrak{K}_\alpha} \hat{C}_{AB}(s) e^{i\boldsymbol{s}\cdot\Delta\boldsymbol{r}} \delta_{-\boldsymbol{s},\boldsymbol{t}} \tag{4.21}$$

where the $n_A$ sum has $hk$ indices, the $n_B$ sum has $\mathfrak{h}\mathfrak{K}$ indices,

$$\boldsymbol{s} = \sum_{l=1}^{m} \boldsymbol{q}_{\mathfrak{h}_l \mathfrak{K}_l}, \; \boldsymbol{t} = \sum_{l=1}^{m} \boldsymbol{q}_{h_l k_l}, \tag{4.22}$$

and $s = |\boldsymbol{s}|$. If $n_i$ are Fourier expanded with two amplitudes as in Sec. 4.2.1.2, then Eq. (4.21) simplifies to

$$\frac{F_{AB}(\Delta \boldsymbol{r})}{\mathcal{A}} = \sum_{\boldsymbol{s}} c_{\boldsymbol{s}} e^{i\boldsymbol{s}\cdot\Delta\boldsymbol{r}}, \tag{4.23}$$

where

$$c_{\boldsymbol{s}} = \sum_{K=0}^{2m} A_1^K A_2^{2m-K} N_{\boldsymbol{s},K} \hat{C}_{AB}(|\boldsymbol{s}|) \tag{4.24}$$

and $N_{\boldsymbol{s},K}$ is the number of vector sums in Eq. (4.21) such that both $\boldsymbol{s} = -\boldsymbol{t}$ and exactly $K$ vectors of magnitude $q_1$ are terms in the sum $\boldsymbol{s}$. Because $N_{\boldsymbol{s},K}$ is an integer, it can be calculated exactly, albeit with computational assistance.

Observe that Eq. (4.23) is in the form of a Fourier series and has the same periodicity as $F_A$ and $F_B$. Since $\boldsymbol{s}$ is a sum of reciprocal lattice vectors, it is a reciprocal lattice vector as well and can be referenced with indices $hk$. Although for finite $m$ there are only a finite set of $\boldsymbol{s}$ vectors, as $m \to \infty$, $\boldsymbol{s}$ comes to include all reciprocal lattice vectors. Consequently, in order to create a desired $F_{AB}(\Delta \boldsymbol{r})$, one simply needs to control $c_{\boldsymbol{s}}$, which is accomplished through modifying $\hat{C}_{AB}(s)$.

The fact that $\hat{C}_{AB}$ is isotropic limits $F_{AB}$ to functions with certain types of symmetries. Since $N_{\{hk\},K}$ are all equal, $c_{\{hk\}}$ are all equal as well. This implies that $F_{AB}$ must be a member of the $p4mm$ plane group, for similar reasons as explained in Sec. 4.2.1.2. Further, if vectors $\boldsymbol{s}_{hk}$ and $\boldsymbol{s}_{uv}$ are distinct but of the same magnitude, meaning $(uv) \notin \{hk\}$ but

$$h^2 + k^2 = u^2 + v^2, \tag{4.25}$$

then

$$\frac{c_{hk}}{c_{uv}} = \frac{\sum_{K=0}^{2m} A_1^K A_2^{2m-K} N_{hk,K}}{\sum_{K=0}^{2m} A_1^K A_2^{2m-K} N_{uv,K}} \tag{4.26}$$

since their correlation function terms must be equal. An example of coefficients that must satisfy Eq. (4.26) are $c_{\{34\}}$ and $c_{\{50\}}$, as well as any other Pythagorean triple. In technical terms, Eq. (4.25) is a Diophantine equation (whose general solution is known) [**90**]. However, given these restrictions on allowed $F_{AB}$ functions and ignoring the problematic terms that solve Eq. (4.25), $F_{AB}$ is controlled by setting $\hat{C}_{AB}$ according to

$$\hat{C}_{AB,set}(s) = \frac{c_s}{\sum_{K=0}^{2m} A_1^K A_2^{2m-K} N_{s,K}}. \tag{4.27}$$

In order to validate that this method can create arbitrary polarizations (Fig. 4.4), it is necessary to choose $c_s$ values. As a simple test, these coefficients were chosen to be the coefficients from an expansion of a sum of delta functions that have the eight-fold symmetry required by a generic position in the $p4mm$ plane group [**83**]. Namely,

$$\begin{aligned} c_{hk}(x_0, y_0) &= \cos[2\pi(hx_0 + ky_0)] + \cos[2\pi(hx_0 - ky_0)] \\ &+ \cos[2\pi(hy_0 + kx_0)] + \cos[2\pi(hy_0 - kx_0)] \end{aligned} \tag{4.28}$$

where $\Delta\boldsymbol{r} = (x_0, y_0)$ (in units of the lattice constant). Although in general $A_1$ and $A_2$ are functions of $F_{AB}$, this makes calculation of $\hat{C}_{AB,set}$ challenging. An example $F_{AB}$ plot for $(x_0, y_0) = (0.66, 0.84)$ is shown in Fig. 4.6, where the single-component amplitudes are used for $A_i$ as in approximation, which is reasonable when $F_{AB}$ is small.

Since Eq. (4.27) only specifies the value of $\hat{C}_{AB}$ at points, a simple extension of Eq. (4.3) is used for defining $\hat{C}_{AB}(q)$. Namely,

$$\begin{aligned} \hat{C}_{AB}(q) = \Omega \Bigg[ &\max_j \left( \hat{C}_{AB,set}(\mathfrak{q}_j) e^{\frac{-(q-\mathfrak{q}_j)^2}{2\varsigma^2}} \right) + \\ &\min_j \left( \hat{C}_{AB,set}(Q_j) e^{\frac{-(q-Q_j)^2}{2\varsigma^2}} \right) \Bigg] \end{aligned} \tag{4.29}$$

where $\hat{C}_{AB,set}(\mathfrak{q}_j) > 0$, $\hat{C}_{AB,set}(Q_j) < 0$, and $\Omega$ is a scale factor. In the limit where $\varsigma$ is small, Eq. (4.29) reduces to a sum. The parameters listed in Table 4.2 were successfully used to create the polarization in Fig. (4.4).

Table 4.2. Table of parameter values for crystal with $\boldsymbol{p} = (0.16, 0.34)$. The associated set of $\{hk\}$ pairs is given for each reciprocal wavevector magnitude.

| Quantity | Value | Vector Set |
|---|---|---|
| $\mathfrak{q}_1$ | $2\pi\sqrt{8}$ | $\{22\}$ |
| $\mathfrak{q}_2$ | $2\pi\sqrt{10}$ | $\{31\}$ |
| $\mathfrak{q}_3$ | $2\pi\sqrt{20}$ | $\{24\}$ |
| $Q_1$ | $2\pi\sqrt{2}$ | $\{11\}$ |
| $Q_2$ | $4\pi$ | $\{20\}$ |
| $Q_3$ | $8\pi$ | $\{40\}$ |
| $Q_4$ | $2\pi\sqrt{18}$ | $\{33\}$ |
| $m$ | 4 | |
| $\mathfrak{b}_1$ | $7.6531 \times 10^{-4}$ | |
| $\mathfrak{b}_2$ | $6.3636 \times 10^{-3}$ | |
| $\mathfrak{b}_3$ | $1.2671 \times 10^{-1}$ | |
| $B_1$ | $2.6224 \times 10^{-4}$ | |
| $B_2$ | $5.2784 \times 10^{-4}$ | |
| $B_3$ | $6.3886 \times 10^{-2}$ | |
| $B_4$ | $1.7314 \times 10^{-1}$ | |
| $\varsigma$ | 0.1 | |
| $a_0$ | 1.0 | |
| $\bar{n}$ | 0 | |

### 4.2.3. Dynamics

In order to create dynamic models out of these free energies, the standard conserved local dynamics equations were employed [**29**]. Namely,

$$\frac{\partial n_i}{\partial t} = \nabla^2 \frac{\delta F}{\delta n_i}. \tag{4.30}$$

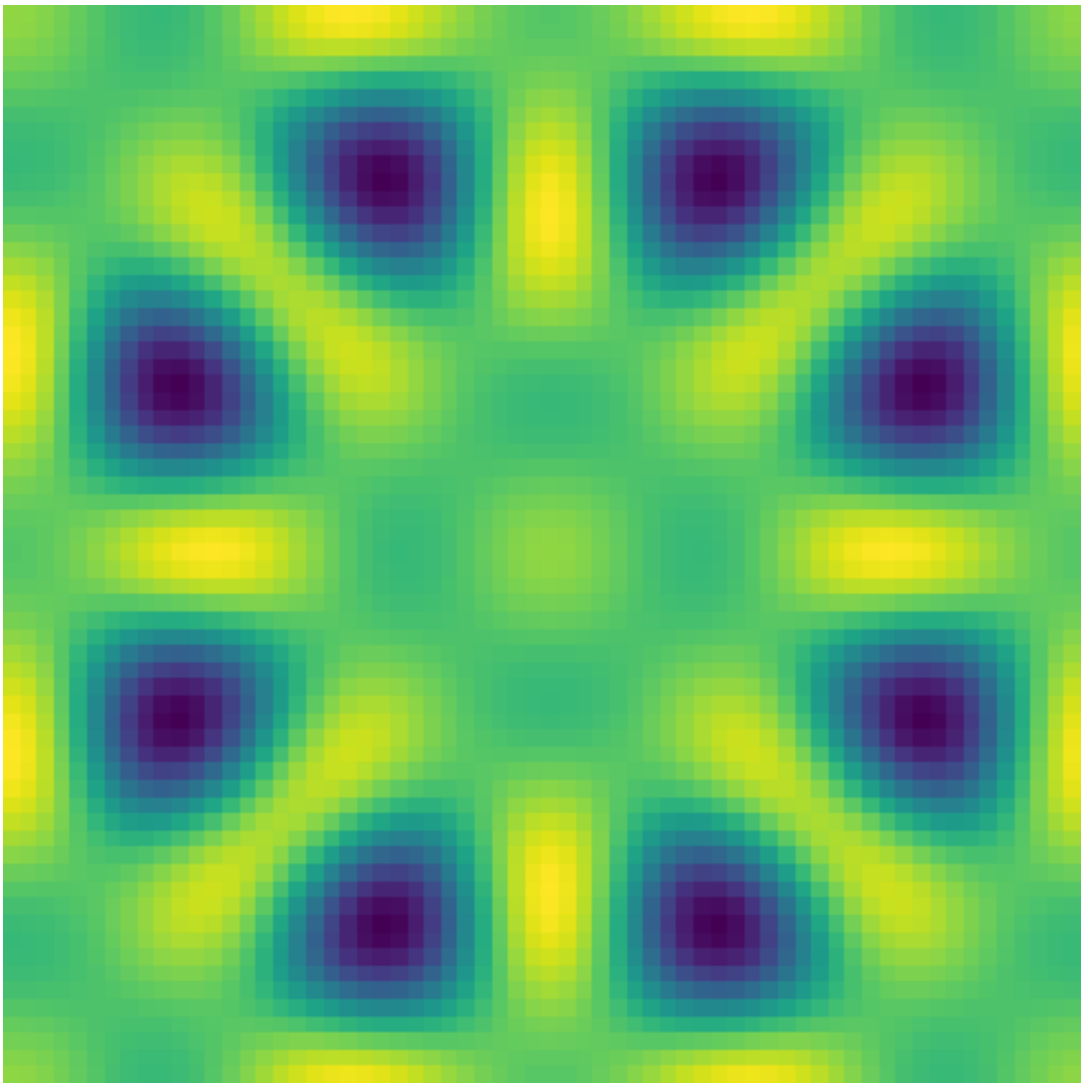

Figure 4.6. $F_{AB}$ plot over a unit cell for a desired $\boldsymbol{p} = (0.16, 0.34)$. The colormap goes from dark blue (lowest values) to light yellow (highest values). $F_{AB}$ contains eight equal minima as intended, horizontal, vertical, and diagonal mirror planes, as well as various four-fold rotation axes.

In cases where the goal is to minimize the free energy, and the equilibrium path is not of interest, the global dynamics equation

$$\frac{\partial n_i}{\partial t} = -\frac{\delta F}{\delta n_i} + \frac{1}{V}\int_V \frac{\delta F}{\delta n_i} d\boldsymbol{r}, \tag{4.31}$$

can be used instead for computational efficiency [**80**].

## 4.3. Comparison to LGD Models

Like traditional PFC models [**91**], our model can also be mapped to phase-field models, namely Landau-Ginzburg-Devonshire models. In general, these models are of the form

$$F = \int_V [f_{bulk}(\boldsymbol{p}) + f_{grad}(\nabla \boldsymbol{p}) + f_{elast}(\epsilon) + f_c(\boldsymbol{p}, \epsilon) + f_{elec}(\boldsymbol{p}, \boldsymbol{E})] d\boldsymbol{r} \tag{4.32}$$

where $f_{bulk}$ is the bulk free energy density, $f_{grad}$ is the energy due to gradients in the polarization, $f_{elast}$ is the contribution from the strain tensor $\epsilon$, $f_c$ is the coupling energy between the polarization and strain fields, and $f_{elec}$ is the electrical energy density as a result of the electric field $\boldsymbol{E}$ [**48**]. Mapping our PFC model to a LGD model is of interest because LGD parameters have been calculated for real materials [**44**, **92**, **93**], and consequently, this is a possible method for PFC parameters fitting. The derivation of the LGD model from the PFC model of Eq. (4.4) is discussed below, and the analytic results from a three amplitude approximation are found in Appendix D.

### 4.3.1. Bulk Energy

The bulk, or Landau-Devonshire, free energy is derived in the same manner as discussed in Section 4.2.1.2. Three-dimensional Landau-Devonshire potentials used practically for modeling perovskites are either sixth- or eighth-order [**94**, **95**], and the PFC model automatically gives the correct symmetries for the bulk energy regardless of the order of the

expansion. To sixth-order, the free energy of a perovskite is

$$f_{bulk} = \frac{1}{2}\alpha(p_x^2 + p_y^2) + \frac{1}{4}[\gamma_{11}(p_x^4 + p_y^4) + \gamma_{12}p_x^2 p_y^2] + \frac{1}{6}[\omega_{111}(p_x^6 + p_y^6) + \omega_{112}(p_x^4 p_y^2 + p_x^2 p_y^4)]. \tag{4.33}$$

### 4.3.2. Gradient Energy

In LGD models for perovskites, the two-dimensional gradient term is

$$f_{grad} = \frac{1}{2}g_{11}\left(\frac{\partial p_x}{\partial x}^2 + \frac{\partial p_y}{\partial y}^2\right) + g_{12}\frac{\partial p_x}{\partial x}\frac{\partial p_y}{\partial y} + g_{44}\left(\frac{\partial p_x}{\partial y}^2 + \frac{\partial p_y}{\partial x}^2\right). \tag{4.34}$$

Although many authors include a fourth gradient coefficient [**92**, **96**, **97**], two of the coefficients are degenerate [**46**, **98**].

The gradient coefficients in our model are calculated by imagining that $n_A$ is fixed, and the polarization gradients are due to the offset $\Delta\boldsymbol{r}$ between the sublattices in Eq. (4.14) being a slowly varying function of position. The strained reciprocal lattice vectors, $\boldsymbol{q}^{str}$, are defined in terms of the Jacobian of $\Delta\boldsymbol{r}$ (the displacement gradient tensor in the language of elasticity), $\mathfrak{u}$, and the unstrained reciprocal lattice vectors $\boldsymbol{q}$. Namely,

$$\boldsymbol{q}^{str} = (\mathfrak{u} + \mathcal{I})^{-1} \cdot \boldsymbol{q}, \tag{4.35}$$

where $\mathcal{I}$ is the identity matrix. If the strained wavevectors are used in Eq. 4.14, the difference in free energy from the unstrained state will solely be due to the two-point correlation function of the strained component. Upon Taylor expanding to second-order,

this free energy difference is exactly Eq. (4.34) where

$$g_{11} = -q_1^2 \sum_{i=1}^{3} |A_i|^2 \hat{C}''_{BB}(q_i)$$

$$g_{12} = g_{44} = -q_1^2 |A_2|^2 \hat{C}''_{BB}(q_2). \tag{4.36}$$

This method for calculating the gradient coefficients is similar to how elastic constants were originally calculated for a single component PFC model [**51**]. It was later discovered that this method for calculating elastic constants is incorrect since the average density changes when the system is strained [**75**, **79**]. This critique could also be leveled against this method of calculating the gradient coefficients. However, because the electrostriction coefficients for this model are approximately zero (see sec. 4.3.3), density changes as a function of polarization can be ignored.

### 4.3.3. Elastic Energy

In addition to the free energies due to polarizations, there are also free energies due to elastic strain. For a material with cubic symmetry, the elastic energy in two dimensions is

$$f_{elast} = \frac{1}{2} c_{11} (\epsilon_{xx}^2 + \epsilon_{yy}^2) + c_{12} \epsilon_{xx} \epsilon_{yy} + 2 c_{44} \epsilon_{xy}^2. \tag{4.37}$$

The elastic constants are derived in the manner suggested by Wang *et al.* [**79**], except the anisotropic variations of the amplitudes are neglected for simplicity. In order to avoid issues with the stresses inherent in the undeformed state affecting the elastic constants, the

system pressure is set to zero in the calculations. Namely, a linear term $\int_V \beta(n_A + n_B)d\boldsymbol{r}$ is added to the free energy, Eq. (4.1), and $\beta$ is then solved so the system pressure is zero.

In real materials, in addition to the purely elastic strain, the $f_c$ energy couples the polarization and strain fields. Namely, there are terms of the form $-\lambda_{ijkl}\epsilon_{ij}p_k p_l$, where $\lambda$ is the electrostrictive constant tensor [**48**]. The result of these terms are that the spontaneous polarization causes a plastic strain so that the unit cell shape changes. For example, $PbTiO_3$ undergoes a cubic $\rightarrow$ tetragonal transition when polarization occurs. Indeed, numerical simulations of the polarization process verifies a square $\rightarrow$ rectangular transition. However, this phenomenon, unlike in real systems, is very small. Using the coefficients in Table 4.1 for example, the unit cell distortion $c/a \simeq 1.0003$. Because the distortion is so small, the electrostriction constants are approximated as zero in this work.

The free energy due to the electrical energy density, $f_{elec}$, found by solving an electrostatic equation is also in theory important [**44**,**46**,**48**,**93**,**99**,**100**]. For simplicity however, the path of early phase-field models is followed [**92**,**96**,**101**], and the inclusion of this term in the PFC model is left for future work. Ignoring the electrical energy density is the limit of high dielectric constant.

## 4.4. Applications

### 4.4.1. Phase Transitions

As a method for comparing the full numerical model to the analytic LGD theory, a $\langle 10 \rangle$ displacive phase transition was examined near the critical temperature. As predicted by fourth-order Landau theory [**89**], the displacive phase transition is second-order. As can be seen in Fig. 4.7, the numerical and analytical results match closely. This check can

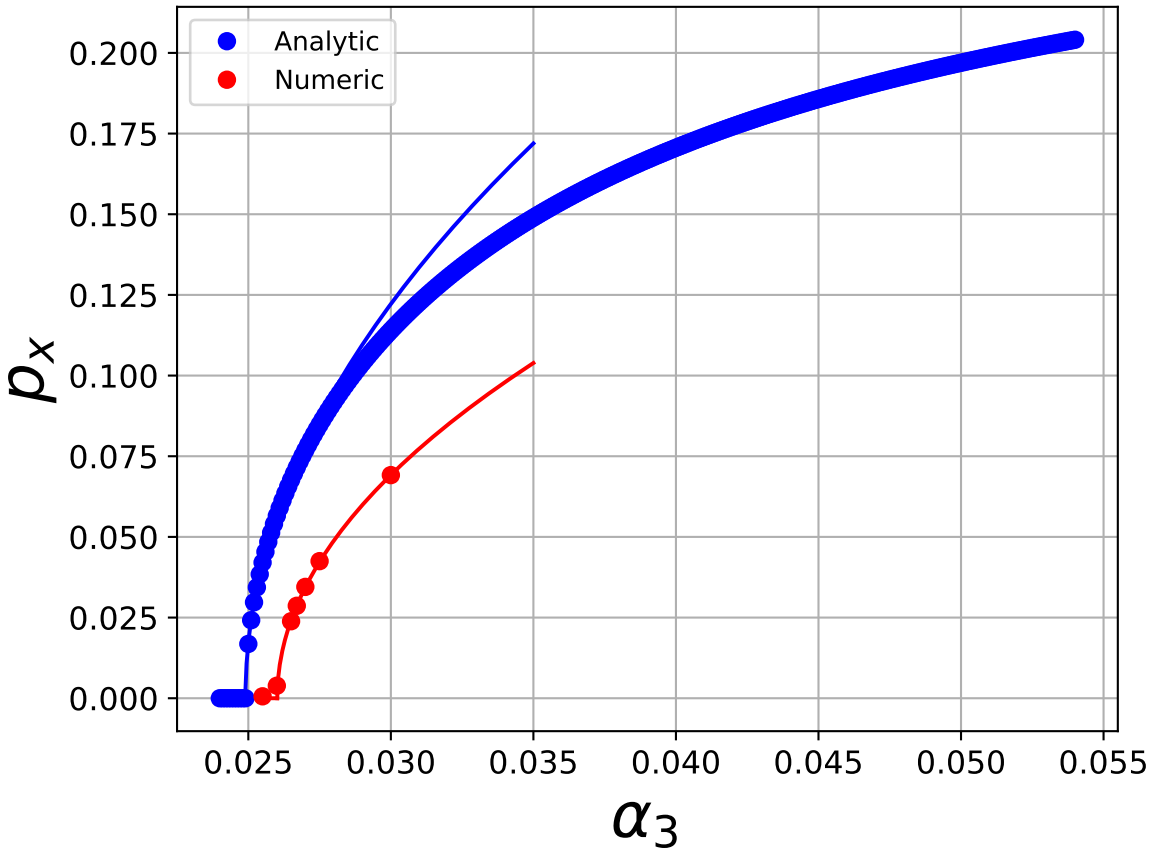


Figure 4.7. Second-order phase transition calculated numerically and analytically.

be thought of as a verification of the Landau-Devonshire [Eq. (4.33)] portion of the free energy. The parameters for Fig. 4.7 and the rest of the applications sections are in Table 4.1.

### 4.4.2. Domain Walls

As a method for comparing the polarization gradient coefficients in our numerical model to the analytic LGD theory, an isolated domain wall was numerically modeled. The system was tested numerically in a $64 \times 2$ domain with periodic boundary conditions and domain

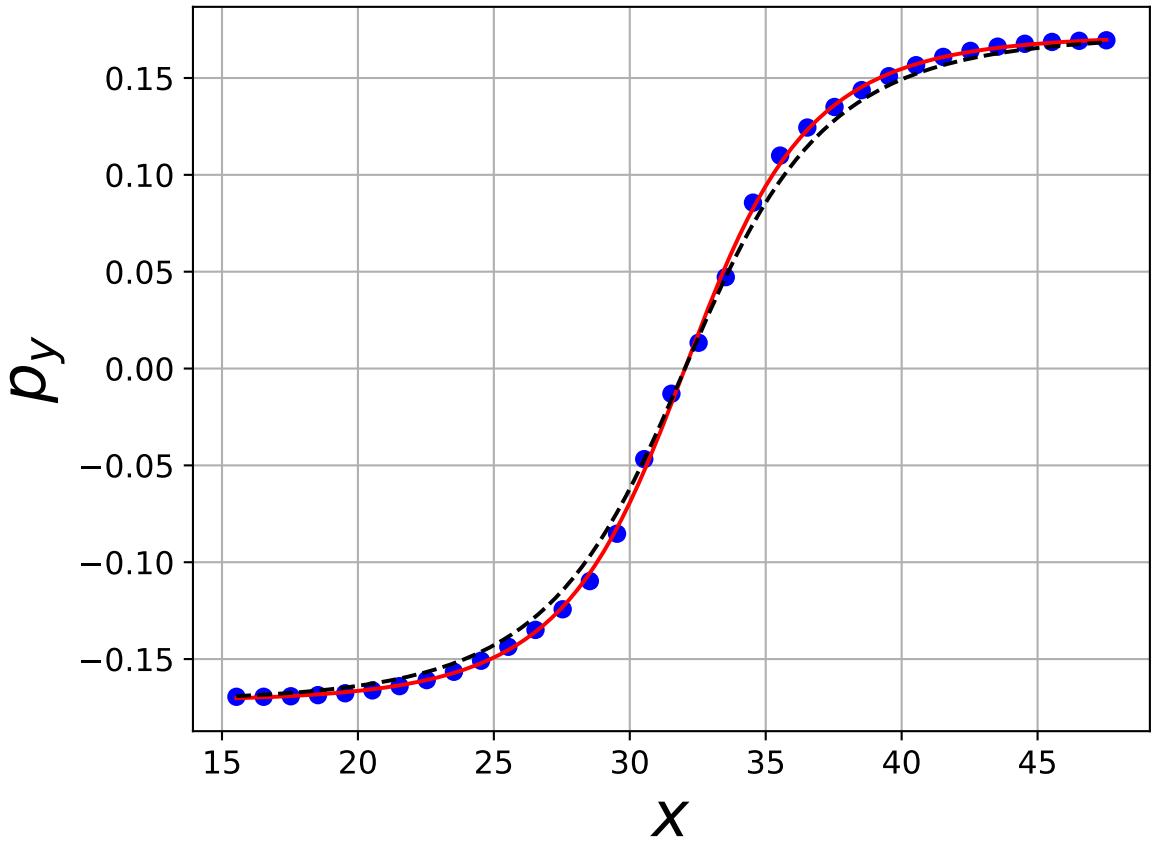


Figure 4.8. Polarization in the $y$ direction across an Ising wall. The points are the numerically calculated values, the red line is a fit to Eq. (4.38) with $\xi = 7.26$, and the dashed line is the analytically calculated $\xi = 8.23$ width.

walls at the center and edges of system. The process for calculating the polarizations is described in Appendix E. Compared with the Cahn-Hilliard equation, many more types of domain walls are possible in our system, including $\uparrow\downarrow$, $\uparrow\rightarrow$, and $\rightarrow\leftarrow$ boundaries. In the case of the $\uparrow\downarrow$ walls simulated, known as Ising walls [**102**], the math reduces to the

one-dimensional case. For a sixth-order bulk free energy, the analytic profile is

$$p_y(x) = p_0 \frac{\sinh\left(\frac{x - x_0}{\xi}\right)}{\left[C + \sinh^2\left(\frac{x - x_0}{\xi}\right)\right]^{1/2}}, \tag{4.38}$$

where

$$\xi = \frac{1}{2p_0}\sqrt{\frac{g_{44}}{C(120\omega_{111}p_0^2 + 3\Gamma_{11})}} \tag{4.39}$$

measures the interface width and $C$ measures the contribution of the sixth-order bulk energy term (the typical fourth-order tanh profile occurs when $C = 1$) [**103**]. By fitting the results of the numerical domain wall to Eq. (4.38), $\xi$ and $C$ were calculated, and their values were used to make a semi-numeric estimate of $g_{44}$. Namely, the value of $p_0$ from a numerical bulk polarization equilibration, $A_1$, $A_2$, and $A_3$ from a numerical bulk unpolarized state equilibration, and $\omega_{111}$ and $\Gamma_{11}$ from the LGD model, were combined with $\xi = 7.26$ and $C = 0.41$ from Ising wall simulation to yield $g_{44} = 0.19$. In comparison, the expression for $g_{44}$ from the LGD model (Appendix D) is $g_{44} = 0.24$, reasonably similar. This implies that the approximations made in the gradient coefficient calculation are somewhat reasonable.

### 4.4.3. Quadrijunctions

In "traditional" systems, such as soap froths and single phase grain structures, quadrijunctions (junctions where four domain walls meet) are thermodynamically unstable and split into trijunctions [**104**, **105**]. However, Cahn showed in the context of an Ising-type stripe formation model on a discrete, square lattice with two-components that weak first and

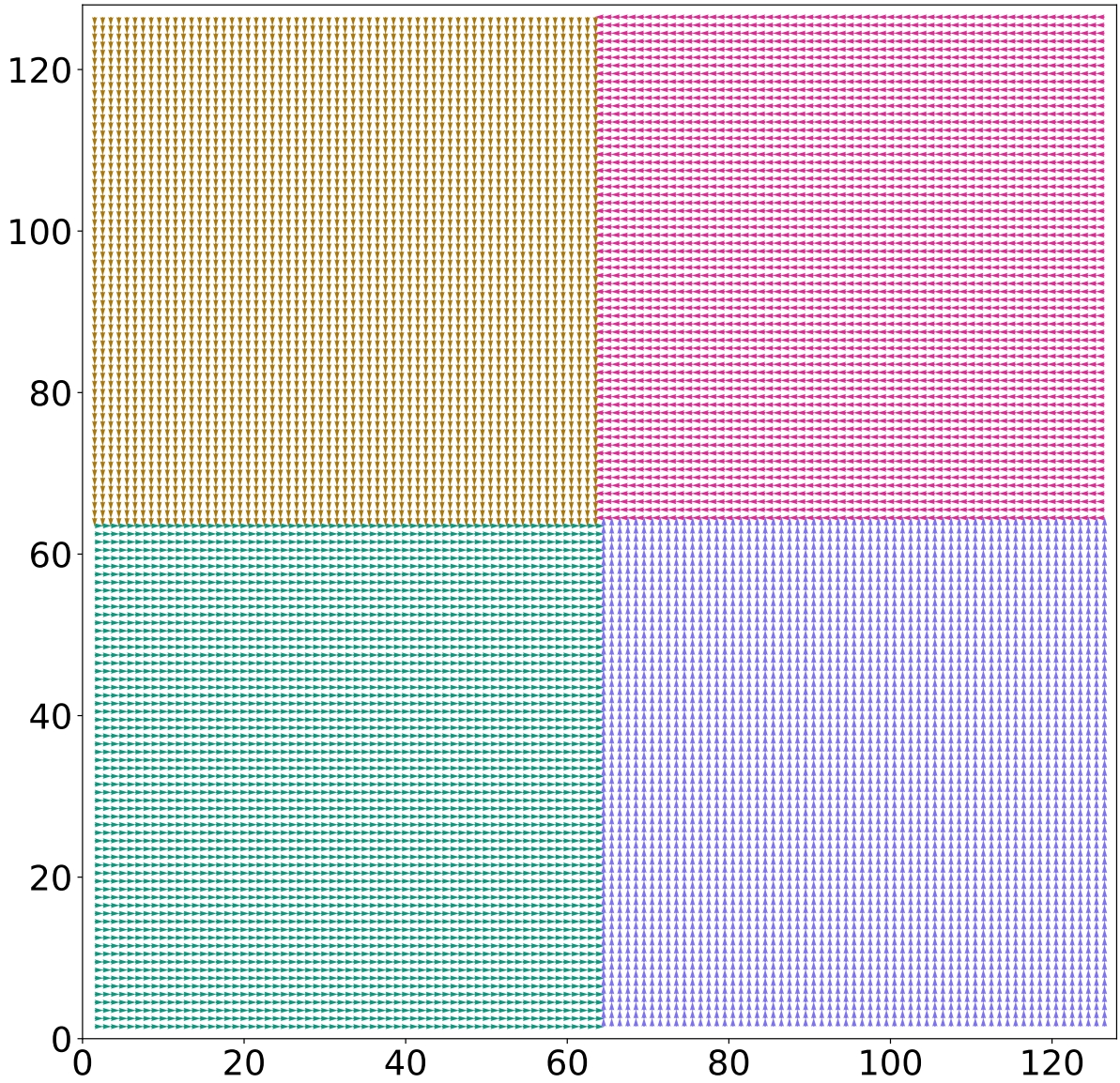


Figure 4.9. The initial condition, with head-to-tail quadrijunctions at the corners and center, and head-to-head quadrijunctions at the midpoints of the sides. The colors denote the four different polarization directions: [10], [01], [$\bar{1}$0], and [0$\bar{1}$]. The white regions are domain boundaries, and the axes are labeled in units of the lattice constant.

strong second neighbor interactions stabilized quadrijunctions [**105**]. Although quadrijunctions have not been studied using LGD models to the authors' knowledge, it was

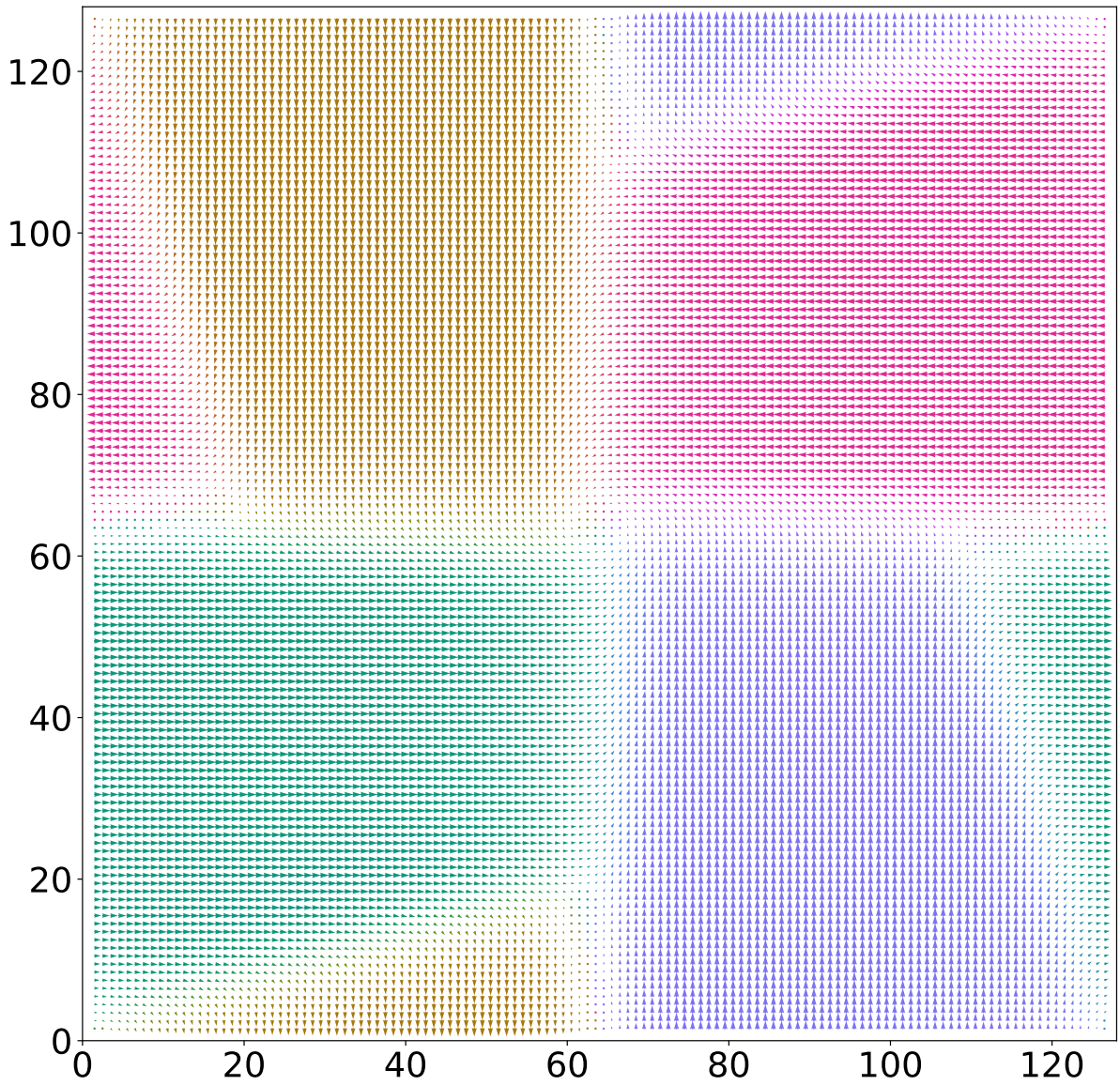


Figure 4.10. The system a short simulated time afterward Fig. 4.9. The head-to-tail quadrijunctions remain stable, but the head-to-head quadrijunctions have decomposed into two trijunctions.

thought that the DPFC model might stabilize quadrijunctions since like in Cahn's Ising model, there are four possible domains.

This hypothesis was confirmed by simulating a periodic domain with clockwise quadrijunctions ($\begin{smallmatrix}\uparrow & \rightarrow \\ \leftarrow & \downarrow\end{smallmatrix}$) at the system's center and corners and head-to-head quadrijunctions ($\begin{smallmatrix}\uparrow & \leftarrow \\ \rightarrow & \downarrow\end{smallmatrix}$) at the edges (Fig. 4.9). The head-to-head quadrijunctions quickly decomposed into trijunctions, but the clockwise junctions remained stable (Fig. 4.10). This is somewhat surprising, as although head-to-head boundaries do not exist in real systems, this is attributed to an excess charge accumulation at the interface, and our model lacks explicit electrostatics terms [**103**].

### 4.4.4. Domain Coarsening with Dislocations

Although it is possible to simulate polarization domains through LGD models [**48**], it is challenging to study the interaction of polarizations with dislocations and grain boundaries using LGD models or traditional atomistic methods. In contrast, this is easy using the phase-field crystal model.

As an illustrative example, domain coarsening across a low-angle symmetric grain boundary was simulated. First, the low-angle boundary was initialized by using a plane wave expansion in the form of Eq. (4.5) for $n_i$, and the standard method was implemented for calculating the dimensions of the periodic grains [**80**]. The maxima of the $n_B$ plane wave expansion were then located. A random number from a multivariable normal distribution was subsequently generated and added to the stored position for the maxima. The plane wave version of $n_B$ was then discarded, and a new $n_B$ that is the sum of multivariable Gaussians created, with each Gaussian centered on a moved maxima. In this way, a system was generated such that the polarization in each unit cell was random.

This system was then run using dynamics of Eq. (4.30), and the results are in Fig. 4.11 – Fig. 4.13. The central line of dislocations clearly impedes the motion of the central [10] domain. Additionally, the $[0\bar{1}]$ region on the left grows downward, despite this increasing the amount of interface, and it is thought this occurs because the two interfaces it creates is lower in energy than the single one is destroys. Neither of these behaviors are motion by mean curvature.

## 4.5. Summary

Although this model successfully incorporates polarization transitions, it lacks a few features true of real perovskites. When real perovskites undergo a $\langle 10 \rangle$ polarization, it simultaneously undergoes a cubic $\rightarrow$ tetragonal transition. The ratio $c/a = 1.18$ in $PbTiO_3$ [**106**]. In the DPFC model, a square $\rightarrow$ rectangular transition occurs during polarization, but the ratio is extremely small. Further, the DPFC model has long range interactions through elasticity, but there are no long range electrostatic contributions as in Seymour's model [**51**]. Lastly, in this model, it is not possible to alter the polarization gradient coefficients independent of the elastic constants. These improvements are left for future work.

What this model does well is introduces a simple and computationally efficient way to begin incorporating displacive ferroelectricity into the PFC model. It is possible to compare this model to LGD models and get qualitatively reasonable results. Phenomena that would be very challenging otherwise, such as the interaction of dislocations with grain boundaries, can begin to be studied. Given a suitable simple cubic model, the model could also be used to simulate perovskites in three dimensions. The model could

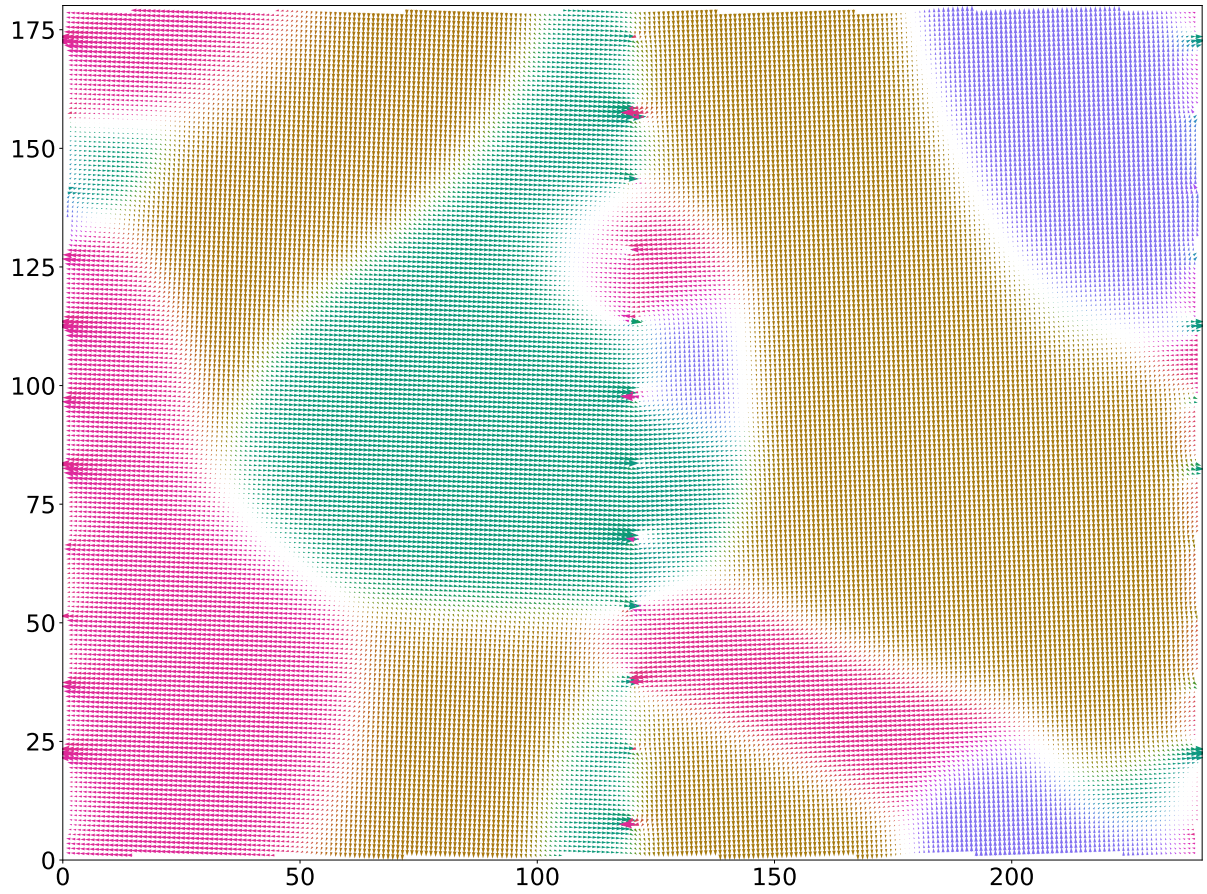


Figure 4.11. Polarization domain coarsening across a 3.8° tilt grain boundary at 9000 timesteps. The color scheme and units are the same as for Fig. 4.9. The dislocations are recognizable as the line of strangely colored points down the middle and edges of the figures. The dislocations impede the domain boundary motion of the central [10] domain. Further, the $[0\bar{1}]$ region on the left side grows during the simulation, despite this growth increasing the amount of boundary. The reason for this is hypothesized to be because $\leftarrow$ $\rightarrow$ interfaces are higher energy than $\leftarrow\downarrow$ and $\downarrow\rightarrow$ interfaces. Thus, domain motion is not simply reduction of mean curvature.

also be extended to more complex displacive transitions, such those accomplished through octahedral rotations in $SrTiO_3$ [**95**]. Additionally, the ideas introduced through creating "generic" polarization begins the conversation about how one might model truly complex materials, such as metal-organic frameworks, using the phase-field crystal method.

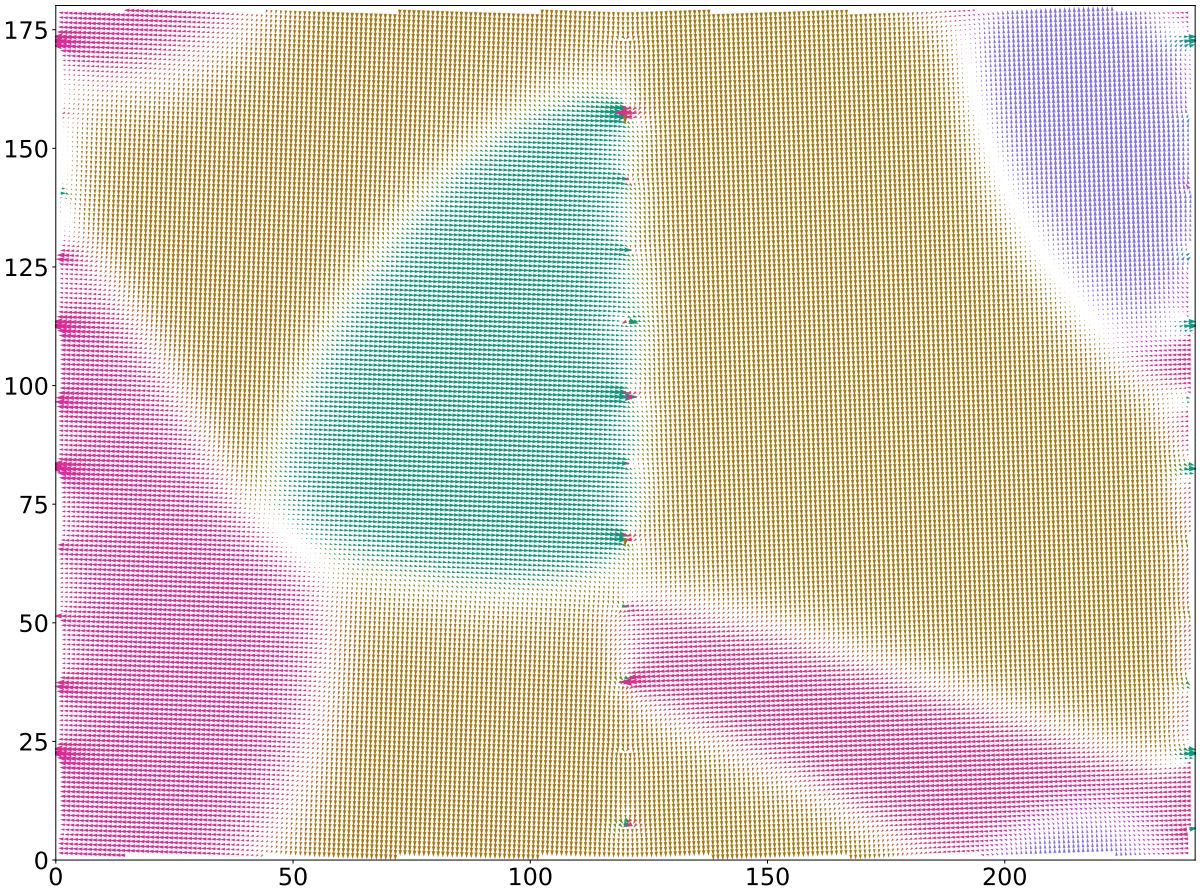


Figure 4.12. Polarization domains at 23000 timesteps.

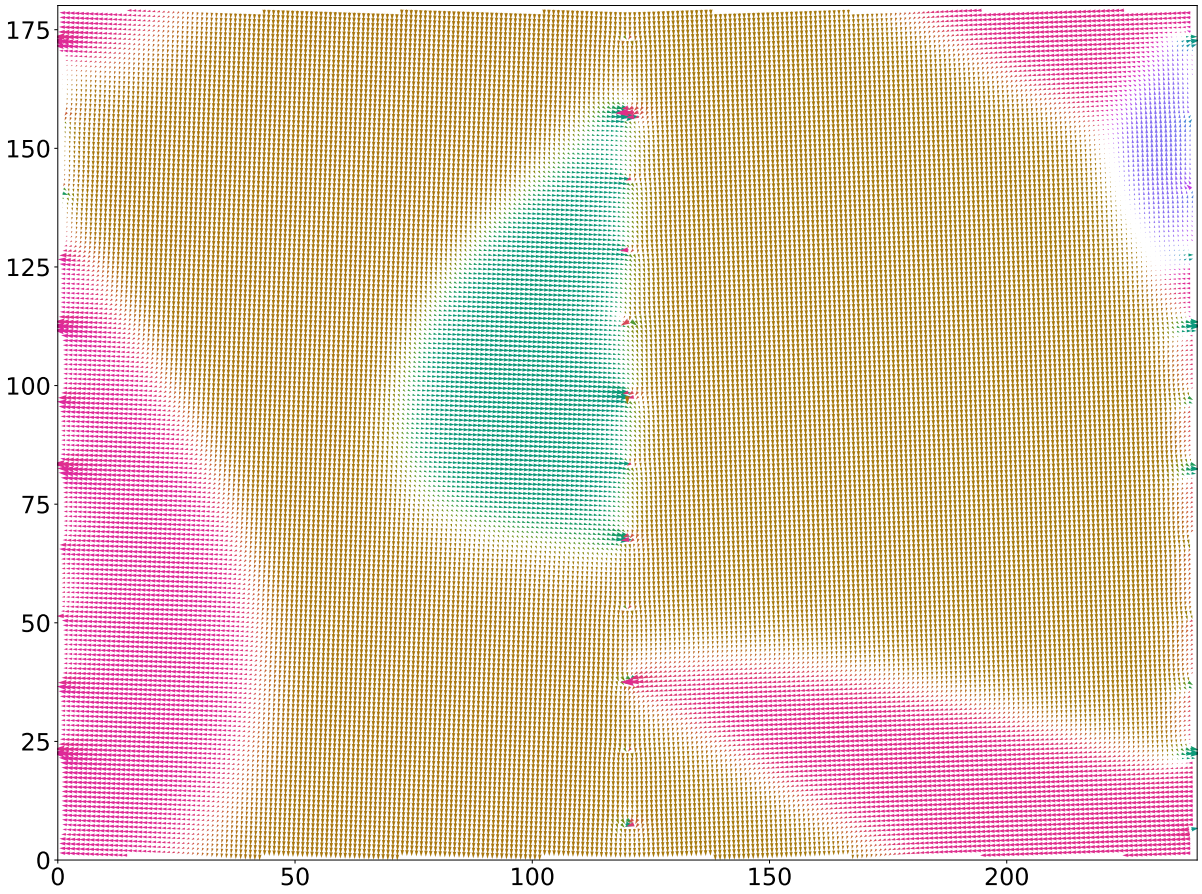


Figure 4.13. Polarization domains at 48000 timesteps.

CHAPTER 5

# Conclusion

The fundamental paradigm of materials science states that the processing of a material determines its structure, and its structure determines its properties. However, predicting and understanding the relationship between processing and structure is difficult. Although experimental methods can examine an existing material's structure, accurate computational models can be quite useful for probing problems that are intractable experimentally, as well as for making predictions.

Unfortunately, typical modeling methods are limited by an inherent coupling between the spatial resolution of the model and the timescale of simulation. For example, traditional molecular dynamics has high spatial resolution, tracking each individual atom, but existing computational hardware normally limits simulation times to the order of nanoseconds. Continuum models are able to span the timescales of actual processing conditions, but they do not contain the spatial resolution necessary for understanding processes that depend on atomistic details.

This thesis focused on one particular methodology that is able to simulate crystalline materials with atomistic resolution on much longer timescales than molecular dynamics. This method, the phase-field crystal method, has been limited by the small number of crystal symmetries it can handle. The thesis greatly expands the number of crystal structures that can be examined by the phase-field crystal model.

In Chapter 2, a PFC model was developed for sublattice ordering and studying order-disorder phase transitions. The free energy for this model was inspired by classical density functional theory, and the chapter describes a systematic method for developing PFC potentials for different ordered crystals. Using the B2 compound as an example, first- and second-order and phase transition were demonstrated, consistent with different types of materials. This investigation also uncovered that the typical expression for temperature dependence in the XPFC model was incorrect, and the correct temperature dependence was clarified. Finally, the model made an interesting prediction that dislocations slow the movement of domain boundaries in these materials.

Chapter 3 developed a systematic technique for creating a new set of single component PFC models, this time using a rotationally invariant three-point correlation function. This method produced a wide array of energy-minimizing crystal structures, from simple cubic and diamond cubic, to graphene layers and disordered $CaF_2$. As an illustration of the utility of this method, the first PFC model with a perovskite structure as the minimum free energy state was created.

Although this model for the perovskite structure was a free energy minimum, it does not demonstrate ferroelectricity, a technologically relevant feature of many perovskites. With the aim of better understanding how to model ferroelectricity in the PFC model, Chapter 4 developed a square two-component two-dimensional PFC model that spontaneously undergoes displacive phase transitions. The mechanism for controlling displacive transitions is discussed in detail, and the model is compared to Landau-Ginzburg-Devonshire (LGD) theories for ferroelectrics. The model also predicts stable quadrijunctions and pinning of domain wall evolution by dislocation cores.

Although much of this work was theoretical and parameter values from real materials were never used, it lays the foundation for future projects in the phase-field crystal community. For example, there are many future directions for the displacive transition topic. For one, it should properly be extended to three dimensions. Both $PbTiO_3$ and $BaTiO_3$ experience polarization states similar to the two-dimensional case explored, so this could be a natural extension. Additionally, all the displacive transitions explored in this work occurred in vectorial directions, and the phase transitions only caused insignificant changes to the crystal's unit cell. In actual systems, other types of displacive transitions are possible. For example, in $SrTiO_3$ the displacive transition involves octahedral rotations. The unit cell also changes dramatically in shape during the phase transition.

This polarization model also does not include any electrostatic terms, clearly important in perovskites. This could perhaps be accomplished by including fields that track the concentration of electrons and holes, so that the charge density could be computed and thereby the polarization and electric potential. In addition to the intrinsic electric potential, future work ought to include the effects of external electric fields.

A final suggested extension for this thesis is to examine defect structures. While this thesis largely focused on equilibrium structures for the new class of materials, it is in fact the defects that are usually of interest. Edge and screw dislocations for crystal structures including $L1_0$, perovskite, and graphene layers could be studied. Their movement and formation in chemical deposition growth is incompletely understood and could benefit from phase-field crystal studies.

# References

[1] Yoshio Waseda. *The Structure of Non-Crystalline Materials: Liquids and Amorphous Solids*. McGraw-Hill, 1980.

[2] Stefano Piana, Kresten Lindorff-Larsen, and David E Shaw. Atomic-level description of ubiquitin folding. *Proceedings of the National Academy of Sciences of the United States of America*, 110(15):5915–20, 2013.

[3] Y. Mishin, M. Asta, and Ju Li. Atomistic modeling of interfaces and their impact on microstructure and properties. *Acta Materialia*, 58(4):1117–1151, feb 2010.

[4] W. J. Boettinger, J. a. Warren, C. Beckermann, and A. Karma. Phase-Field Simulation of Solidification. *Annual Review of Materials Research*, 32(1):163–194, aug 2002.

[5] K. R. Elder, Mark Katakowski, Mikko Haataja, and Martin Grant. Modeling Elasticity in Crystal Growth. *Physical Review Letters*, 88(24):245701, jun 2002.

[6] K. R. Elder, Nikolas Provatas, Joel Berry, Peter Stefanovic, and Martin Grant. Phase-field crystal modeling and classical density functional theory of freezing. *Physical Review B*, 75(6):064107, feb 2007.

[7] Yashwant Singh. Density-functional theory of freezing and properties of the ordered phase. *Physics Reports*, 207(6):351–444, 1991.

[8] Kuo-An Wu and Alain Karma. Phase-field crystal modeling of equilibrium bcc-liquid interfaces. *Physical Review B*, 76(18):184107, nov 2007.

[9] A. Jaatinen, C. V. Achim, K. R. Elder, and T. Ala-Nissila. Thermodynamics of bcc metals in phase-field-crystal models. *Physical Review E*, 80(3):031602, sep 2009.

[10] A Jaatinen and T Ala-Nissila. Extended phase diagram of the three-dimensional phase field crystal model. *Journal of Physics: Condensed Matter*, 22(20):205402, may 2010.

[11] Kuo-An Wu, Ari Adland, and Alain Karma. Phase-field-crystal model for fcc ordering. *Physical Review E*, 81(6):061601, jun 2010.

[12] F Igloi, G Kahl, and J Hafner. The freezing of simple liquid metals: density functional approach to the structural stability of the crystalline phase. *Journal of Physics C: Solid State Physics*, 20(12):1803–1813, apr 1987.

[13] Michael Greenwood, Nikolas Provatas, and Jörg Rottler. Free energy functionals for efficient phase field crystal modeling of structural phase transformations. *Physical Review Letters*, 105(4):045702, feb 2010.

[14] Michael Greenwood, Jörg Rottler, and Nikolas Provatas. Phase-field-crystal methodology for modeling of structural transformations. *Physical Review E*, 83(3):031601, mar 2011.

[15] S. K. Mkhonta, K. R. Elder, and Zhi-Feng Huang. Exploring the Complex World of Two-Dimensional Ordering with Three Modes. *Physical Review Letters*, 111(3):035501, jul 2013.

[16] S. K. Mkhonta, K. R. Elder, and Zhi-Feng Huang. Emergence of Chirality from Isotropic Interactions of Three Length Scales. *Physical Review Letters*, 116(20):205502, 2016.

[17] Jason Luce and Katsuyo Thornton. Parameterization of the Structural Phase Field Crystal (XPFC) model for the simulation of hexagonal close packed (HCP) grain boundary kinetics. 2018.

[18] V. W. L. Chan, N. Pisutha-Arnond, and K. Thornton. Phase-field crystal model for a diamond-cubic structure. *Physical Review E*, 91(5):053305, may 2015.

[19] N. Pisutha-Arnond, V. W L Chan, M. Iyer, V. Gavini, and K Thornton. Classical density functional theory and the phase-field crystal method using a rational function to describe the two-body direct correlation function. *Physical Review E - Statistical, Nonlinear, and Soft Matter Physics*, 87:1–14, 2013.

[20] Matthew Seymour and Nikolas Provatas. Structural phase field crystal approach for modeling graphene and other two-dimensional structures. *Physical Review B*, 93(3):035447, jan 2016.

[21] Yongmei M. Jin and Armen G. Khachaturyan. Atomic density function theory and modeling of microstructure evolution at the atomic scale. *Journal of Applied Physics*, 100(1):013519, jul 2006.

[22] Mykola Lavrskyi, Helena Zapolsky, and Armen G Khachaturyan. Quasiparticle approach to diffusional atomic scale self-assembly of complex structures: from disorder to complex crystals and double-helix polymers. *npj Computational Materials*, 2(1):15013, nov 2016.

[23] Zi-le Wang, Zhirong Liu, and Zhi-feng Huang. Angle-Adjustable Density Field Formulation for Modeling Crystalline Microstructures. pages 1–5.

[24] Petri Hirvonen, Mikko M. Ervasti, Zheyong Fan, Morteza Jalalvand, Matthew Seymour, S. Mehdi Vaez Allaei, Nikolas Provatas, Ari Harju, Ken R. Elder, and Tapio Ala-Nissila. Multiscale modeling of polycrystalline graphene: A comparison of structure and defect energies of realistic samples from phase field crystal models. *Physical Review B*, 94(3):035414, jul 2016.

[25] Michael Greenwood, Nana Ofori-Opoku, Jörg Rottler, and Nikolas Provatas. Modeling structural transformations in binary alloys with phase field crystals. *Physical Review B*, 84(6):064104, aug 2011.

[26] K. L. M. Elder, Matthew Seymour, M. Lee, M. Hilke, and Nikolas Provatas. Two-component structural phase-field crystal models for graphene symmetries. *Philosophical Transactions of the Royal Society A: Mathematical, Physical and Engineering Sciences*, 376(2113):20170211, feb 2018.

[27] Eli Alster, K. R. Elder, Jeffrey J. Hoyt, and Peter W. Voorhees. Phase-field-crystal model for ordered crystals. *Physical Review E*, 95(2):022105, feb 2017.

[28] Yunhao Huang, Jincheng Wang, Zhijun Wang, Junjie Li, and Can Guo. Description of order-disorder transitions based on the phase-field-crystal model. *Physical Review E*, 95(January):1–10, 2017.

[29] Doaa Taha, S. K. Mkhonta, K. R. Elder, and Zhi-feng Huang. Grain Boundary Structures and Collective Dynamics of Inversion Domains in Binary Two-Dimensional Materials. *Physical Review Letters*, 118(25):255501, jun 2017.

[30] Eli Alster, David Montiel, Katsuyo Thornton, and Peter W. Voorhees. Simulating complex crystal structures using the phase-field crystal model. *Physical Review Materials*, 1(6):060801, nov 2017.

[31] Joel Berry, Nikolas Provatas, Jörg Rottler, and Chad W. Sinclair. Phase field crystal modeling as a unified atomistic approach to defect dynamics. *Physical Review B*, 89(21):214117, jun 2014.

[32] Kuo-An Wu, Shang-Chun Lin, and Alain Karma. Two-mode Ginzburg-Landau theory of crystalline anisotropy for fcc-liquid interfaces. *Physical Review B*, 93(5):054114, 2016.

[33] Joel Berry, Nikolas Provatas, Jörg Rottler, and Chad W. Sinclair. Defect stability in phase-field crystal models: Stacking faults and partial dislocations. *Physical Review B*, 86(22):224112, dec 2012.

[34] Vahid Fallah, Andreas Korinek, Nana Ofori-Opoku, Nikolas Provatas, and Shahrzad Esmaeili. Atomistic investigation of clustering phenomenon in the Al-Cu system: Three-dimensional phase-field crystal simulation and HRTEM/HRSTEM characterization. *Acta Materialia*, 61(17):6372–6386, oct 2013.

[35] Vahid Fallah, Brian Langelier, Nana Ofori-Opoku, Babak Raeisinia, Nikolas Provatas, and Shahrzad Esmaeili. Cluster evolution mechanisms during aging in Al-Mg-Si alloys. *Acta Materialia*, 103(2016):290–300, 2016.

[36] Mikael C. Rechtsman, Frank H. Stillinger, and Salvatore Torquato. Self-assembly of the simple cubic lattice with an isotropic potential. *Physical Review E*, 74(2):021404, aug 2006.

[37] Mikael C. Rechtsman, Frank H. Stillinger, and Salvatore Torquato. Synthetic diamond and wurtzite structures self-assemble with isotropic pair interactions. *Physical Review E*, 75(3):031403, mar 2007.

[38] E. Edlund, O. Lindgren, and M. Nilsson Jacobi. Designing Isotropic Interactions for Self-Assembly of Complex Lattices. *Physical Review Letters*, 107(8):085503, aug 2011.

[39] Kobi Barkan, Michael Engel, and Ron Lifshitz. Controlled Self-Assembly of Periodic and Aperiodic Cluster Crystals. *Physical Review Letters*, 113(9):098304, aug 2014.

[40] Wan-Jian Yin, Ji-Hui Yang, Joongoo Kang, Yanfa Yan, and Su-Huai Wei. Halide perovskite materials for solar cells: a theoretical review. *J. Mater. Chem. A*, 3(17):8926–8942, 2015.

[41] D. Bi, W. Tress, M. I. Dar, P. Gao, J. Luo, C. Renevier, K. Schenk, Antonio Abate, Fabrizio Giordano, J.-P. Correa Baena, J.-D. Decoppet, S. M. Zakeeruddin, M. K. Nazeeruddin, M. Gra tzel, and A. Hagfeldt. Efficient luminescent solar cells based on tailored mixed-cation perovskites. *Science Advances*, 2(1):e1501170–e1501170, jan 2016.

[42] Zhi-Kuang Tan, Reza Saberi Moghaddam, May Ling Lai, Pablo Docampo, Ruben Higler, Felix Deschler, Michael Price, Aditya Sadhanala, Luis M. Pazos, Dan Credgington, Fabian Hanusch, Thomas Bein, Henry J. Snaith, and Richard H. Friend. Bright light-emitting diodes based on organometal halide perovskite. *Nature Nanotechnology*, 9(9):687–692, aug 2014.

[43] Boris A. Strukov and Arkadi P. Levanyuk. *Ferroelectric Phenomena in Crystals*. Springer Berlin Heidelberg, Berlin, Heidelberg, 1998.

[44] John Mangeri, Yomery Espinal, Andrea Jokisaari, S. Pamir Alpay, Serge Nakhmanson, and Olle Heinonen. Topological phase transformations and intrinsic size effects in ferroelectric nanoparticles. *Nanoscale*, 9(4):1616–1624, 2017.

[45] Shi Liu, Ilya Grinberg, and Andrew M. Rappe. Intrinsic ferroelectric switching from first principles. *Nature*, 534(7607):360–363, 2016.

[46] J. Hlinka and P. Márton. Phenomenological model of a 90 domain wall in BaTiO3-type ferroelectrics. *Physical Review B*, 74(10):104104, sep 2006.

[47] P. Marton, I. Rychetsky, and J. Hlinka. Domain walls of ferroelectric BaTiO3 within the Ginzburg-Landau-Devonshire phenomenological model. *Physical Review B*, 81(14):144125, apr 2010.

[48] Long-qing Chen. Phase-Field Method of Phase Transitions/Domain Structures in Ferroelectric Thin Films: A Review. *Journal of the American Ceramic Society*, 91(6):1835–1844, jun 2008.

[49] Niloufar Faghihi, Nikolas Provatas, K. R. Elder, Martin Grant, and Mikko Karttunen. Phase-field-crystal model for magnetocrystalline interactions in isotropic ferromagnetic solids. *Physical Review E*, 88(3):032407, sep 2013.

[50] Niloufar Faghihi, Simiso Mkhonta, Ken R Elder, and Martin Grant. Magnetic islands modelled by a phase-field-crystal approach. *The European Physical Journal B*, 91(3):55, mar 2018.

[51] Matthew Seymour, F. Sanches, Ken Elder, and Nikolas Provatas. Phase-field crystal approach for modeling the role of microstructure in multiferroic composite materials. *Physical Review B*, 92(18):184109, nov 2015.

[52] William H. Beamer and Charles R. Maxwell. The Crystal Structure of Polonium. *The Journal of Chemical Physics*, 14(9):569–569, sep 1946.

[53] Neil W. Ashcroft and David N. Mermin. *Solid State Physics*. Cengage Learning, India, 2014.

[54] C. Wolverton and V. OzoliÅĘš. Entropically Favored Ordering: The Metallurgy of Al2Cu Revisited. *Physical Review Letters*, 86(24):5518–5521, jun 2001.

[55] K Gschneidner Jr., A Russell, A Pecharsky, J Morris, Z Zhang, T Lograsso, D Hsu, C H Lo, Y Ye, A Slager, and D Kesse. A family of ductile intermetallic compounds. *Nat Mater*, 2(9):587–591, 2003.

[56] J. Zou and C. L. Fu. Structural, electronic, and magnetic properties of 3d transition-metal aluminides with equiatomic composition. *Physical Review B*, 51(4):2115, 1995.

[57] L.G. Zhang, G.X. Huang, H.Y. Qi, B.R. Jia, L.B. Liu, and Z.P. Jin. Thermodynamic assessment of the CuâĂŞDy binary system. *Journal of Alloys and Compounds*, 470(1-2):214–217, 2009.

[58] Annick Loiseau. The role of interfaces and domain boundaries in order-disorder transitions. *Current Opinion in Solid State & Materials Science*, 1:369–377, 1996.

[59] D. Le Floc'h, A Loiseau, Ch Ricolleau, C Barreteau, R Caudron, F Ducastelle, and J. M. Pénisson. Critical behavior of antiphase boundaries in fe3al close to the do3 –> b2 phase transition. *Physical Review Letters*, 81(11):2272–2275, sep 1998.

[60] Nikolas Provatas and K. R. Elder. *Phase-Field Methods in Material Science and Engineering*. Wiley-VCH, 2010.

[61] Zhi-Feng Huang, K. R. Elder, and Nikolas Provatas. Phase-field-crystal dynamics for binary systems: Derivation from dynamical density functional theory, amplitude equation formalism, and applications to alloy heterostructures. *Physical Review E*, 82(2):021605, aug 2010.

[62] Jeffrey J. Hoyt. *Phase Transformations*. McMaster Innovation Press, Hamilton, 2010.

[63] B. D. Cullity and S. R. Stock. *Elements of X-Ray Diffraction*. Pearson, 3 edition, 2013.

[64] Charles Kittel. *Introduction to Solid State Physics*. John Wiley & Sons, Inc, 8 edition, 2005.

[65] Donald A. McQuarrie. *Statistical Mechanics*. University Science Books, Sausalito, 1 edition, 2000.

[66] David Chandler. *Introduction to Modern Statistical Mechanics*. Oxford University Press, New York, 1 edition, 1987.

[67] Kuo-An Wu and Peter W. Voorhees. Stress-induced morphological instabilities at the nanoscale examined using the phase field crystal approach. *Physical Review B*, 80(12):125408, sep 2009.

[68] Nana Ofori-Opoku, Vahid Fallah, Michael Greenwood, Shahrzad Esmaeili, and Nikolas Provatas. Multicomponent phase-field crystal model for structural transformations in metal alloys. *Physical Review B*, 87(13):134105, apr 2013.

[69] Vahid Fallah, Nana Ofori-Opoku, Jonathan Stolle, Nikolas Provatas, and Shahrzad Esmaeili. Simulation of early-stage clustering in ternary metal alloys using the phase-field crystal method. *Acta Materialia*, 61(10):3653–3666, 2013.

[70] Bernadine A Jugdutt and Nikolas Provatas. *Calculating the role of composition in the anisotropy of the solid-liquid interface via phase field crystal theory.* Master's thesis, McGill University, 2014.

[71] James E. Saal, Scott Kirklin, Muratahan Aykol, Bryce Meredig, and C. Wolverton. Materials design and discovery with high-throughput density functional theory: The open quantum materials database (OQMD). *JOM*, 65(11):1501–1509, 2013.

[72] C. Wolverton and V. Ozolins. First-principles aluminum database: Energetics of binary Al alloys and compounds. *Physical Review B*, 73(14):144104, apr 2006.

[73] Bernadine A. Jugdutt, Nana Ofori-Opoku, and Nikolas Provatas. Calculating the role of composition in the anisotropy of solid-liquid interface energy using phase-field-crystal theory. *Physical Review E*, 92(4):042405, oct 2015.

[74] Ikuo Ohnuma, Hirotoshi Enoki, Osamu Ikeda, Ryosuke Kainuma, Hiroshi Ohtani, Bo Sundman, and Kiyohito Ishida. Phase equilibria in the Fe-Co binary system. *Acta Materialia*, 50(2):379–393, 2002.

[75] N. Pisutha-Arnond, V. W L Chan, K. R. Elder, and K. Thornton. Calculations of isothermal elastic constants in the phase-field crystal model. *Physical Review B*, 87(1):014103, jan 2013.

[76] Robert Spatschek and Alain Karma. Amplitude equations for polycrystalline materials with interaction between composition and stress. *Physical Review B*, 81(21):214201, jun 2010.

[77] T. Castan and A. Planes. Elastic constants of bcc shape-memory binary lloys: Effect of the configurational ordering. *Physical Review B*, 38(12):7959–7965, 1988.

[78] G. M. McManus. Elastic Properties of Beta-CuZn. *Physical Review*, 129(5):2004–7, 1963.

[79] Zi-Le Wang, Zhi-Feng Huang, and Zhirong Liu. Elastic constants of stressed and unstressed materials in the phase-field crystal model. *Physical Review B*, 97(14):144112, apr 2018.

[80] Jesper Mellenthin, Alain Karma, and Mathis Plapp. Phase-field crystal study of grain-boundary premelting. *Physical Review B*, 78(18):184110, 2008.

[81] P. K. Galenko, F. Iunes Sanches, and K. R. Elder. Traveling wave profiles for a crystalline front invading liquid states: Analytical and numerical solutions. *Physica D: Nonlinear Phenomena*, 308(2015):1–10, 2015.

[82] NIST. Spherical and Spheroidal Harmonics, 2017.

[83] M. I. Aroyo, editor. *International Tables for Crystallography*, volume A. International Union of Crystallography, Chester, England, dec 2016.

[84] S. Alexander and J. McTague. Should All Crystals Be bcc? Landau Theory of Solidification and Crystal Nucleation. *Physical Review Letters*, 41(10):702–705, sep 1978.

[85] Mohammad Mahdi Tavakoli, Leilei Gu, Yuan Gao, Claas Reckmeier, Jin He, Andrey L. Rogach, Yan Yao, and Zhiyong Fan. Fabrication of efficient planar perovskite solar cells using a one-step chemical vapor deposition method. *Scientific Reports*, 5(1):14083, nov 2015.

[86] Edwin J. Schwalbach, J. A. Warren, Kuo-An Wu, and Peter W. Voorhees. Phase-field crystal model with a vapor phase. *Physical Review E*, 88(2):023306, aug 2013.

[87] Gabriel Kocher and Nikolas Provatas. New Density Functional Approach for Solid-Liquid-Vapor Transitions in Pure Materials. *Physical Review Letters*, 114(15):155501, 2015.

[88] Raffaele Resta. Quantum-Mechanical Position Operator in Extended Systems. *Physical Review Letters*, 80(9):1800–1803, mar 1998.

[89] Serge Galam. Irrelevant variables, Landau expansions, and cubic anisotropy. *Physical Review B*, 31(3):1554–1558, feb 1985.

[90] Henri Cohen. Introduction to Diophantine Equations. In *Number Theory*, pages 1–8. Springer New York, New York, NY, dec 2007.

[91] Nigel Goldenfeld, Badrinarayan P. Athreya, and Jonathan A. Dantzig. Renormalization group approach to multiscale simulation of polycrystalline materials using

the phase field crystal model. *Physical Review E - Statistical, Nonlinear, and Soft Matter Physics*, 72(2):1–4, 2005.

[92] Y. L. Li, S. Y. Hu, Z. K. Liu, and L. Q. Chen. Phase-field model of domain structures in ferroelectric thin films. *Applied Physics Letters*, 78(24):3878–3880, jun 2001.

[93] Hong-Liang Hu and Long-Qing Chen. Ferroelectric Domain Formation. *Journal of American Ceramic Society*, 81(1998):492–500, 1998.

[94] David Vanderbilt and Morrel H. Cohen. Monoclinic and triclinic phases in higher-order Devonshire theory. *Physical Review B - Condensed Matter and Materials Physics*, 63(9):1–9, 2001.

[95] K. M Rabe, Ch. H. Ahn, J. M M. Triscone, M Dawber, and C Lichtensteiger. *Physics of Ferroelectrics*, volume 105 of *Topics in Applied Physics*. Springer Berlin Heidelberg, Berlin, Heidelberg, 2007.

[96] Shinji Nambu and Djuniadi A. Sagala. Domain formation and elastic long-range interaction in ferroelectric perovskites. *Physical Review B*, 50(9):5838–5847, 1994.

[97] John Mangeri, Yomery Espinal, Andrea Jokisaari, S. Pamir Alpay, Serge Nakhmanson, and Olle Heinonen. Topological phase transformations and intrinsic size effects in ferroelectric nanoparticles. 2017.

[98] Wenwu Cao. Constructing Landau-Ginzburg-Devonshire Type Models for Ferroelectric Systems Based on Symmetry. *Ferroelectrics*, 375(1):28–39, dec 2008.

[99] Y. L. Li, S. Y. Hu, Z. K. Liu, and L. Q. Chen. Effect of electrical boundary conditions on ferroelectric domain structures in thin films. *Applied Physics Letters*, 81(3):427–429, 2002.

[100] Byounghak Lee, Serge M. Nakhmanson, and Olle Heinonen. Strain induced vortex-to-uniform polarization transitions in soft-ferroelectric nanoparticles. *Applied Physics Letters*, 104(26), 2014.

[101] Y. L. Li, S. Y. Hu, Z. K. Liu, and L. Q. Chen. Effect of substrate constraint on the stability and evolution of ferroelectric domain structures in thin films. *Acta Materialia*, 50(2):395–411, 2002.

[102] Rakesh K Behera, Chan-Woo Lee, Donghwa Lee, Anna N Morozovska, Susan B Sinnott, Aravind Asthagiri, Venkatraman Gopalan, and Simon R Phillpot. Structure and energetics of 180 domain walls in PbTiO3 by density functional theory. *Journal of Physics: Condensed Matter*, 23(17):175902, 2011.

[103] B. Meyer and David Vanderbilt. Ab initio study of ferroelectric domain walls in PbTiO 3. *Physical Review B*, 65(10):104111, mar 2002.

[104] E.A. Holm, D.J. Srolovitz, and J.W. Cahn. Microstructural evolution in two-dimensional two-phase polycrystals. *Acta Metallurgica et Materialia*, 41(4):1119–1136, apr 1993.

[105] J.W. Cahn and E.S. Van Vleck. On the co-existence and stability of trijunctions and quadrijunctions in a simple model. *Acta Materialia*, 47(18):4627–4639, dec 1999.

[106] Avni Jain, Jeffrey R. Errington, and Thomas M. Truskett. Inverse design of simple pairwise interactions with low-coordinated 3D lattice ground states. *Soft Matter*, 9(14):3866, 2013.

[107] Nicola A. Spaldin. A beginner's guide to the modern theory of polarization. *Journal of Solid State Chemistry*, 195(2012):2–10, nov 2012.

[108] Raffaele Resta. Polarization in Kohn-Sham density-functional theory. *The European Physical Journal B*, 91(6):100, jun 2018.

[109] Matthew Seymour. *Study of Multi-Point Interactions in PFC Models for Complex Structural Transformations*. PhD thesis, McGill University, 2017.

APPENDIX A

# Complex Crystal Structure Parameters

The parameters for all the crystal structures of Chapter 3 are detailed in Table A.1. The abbreviation *DC* refers to diamond cubic, SH to simple hexagonal, SC to simple cubic, GL to graphene layers, and $X_3$ to the structure of the $X$ component of the $ABX_3$ perovskite/anti-perovskite structure. The asterisk denotes that for graphene layers, $\alpha_0$ was changed from $-1/2$, inconsistent with the $P_l$ calculation. This change was motivated by the fact that the graphene layers structure is the inverse (negative peaks) of simple hexagonal. The correlation function parameters are defined by the equations

$$\hat{C}_2(k) = A_0 e^{-\frac{k^2}{2\sigma^2}} + \max_i (A_i e^{-\frac{(k-q_i)^2}{2\sigma^2}}) \tag{A.1}$$

and

$$\hat{R}(k) = \max_j (A_j e^{-\frac{(k-r_j)^2}{2\sigma^2}}). \tag{A.2}$$

For perovskite, nearly all parameters are the same as for the single components listed in Table A.1. The only changes are that for $B$, $A_1 = 0.95$, $A_2 = 0.93$, and $\beta = 0.95$. Additionally, $Z = 0.05$.

Table A.1. Table of parameter values for different crystal structures, with parameter definitions defined by Eq. (A.1) and Eq. (A.2).

| | **DC** | **SH** | **SC** | **GL** | **$CaF_2$** | **$X_3$** |
|---|---|---|---|---|---|---|
| $A_0$ | - | - | - | - | $-5$ | - |
| $A_1$ | 1.0 | 1.0 | 1.0 | 1.0 | 0.9 | 0.95 |
| $A_2$ | - | 0.99 | 0.98 | 0.99 | 1.05 | 0.95 |
| $A_3$ | - | 0.98 | - | 0.98 | - | 1.0 |
| $A_4$ | - | - | - | - | - | 0.98 |
| $q_1$ | $2\pi$ | $2\pi$ | $2\pi$ | $2\pi$ | $2\pi\sqrt{3/8}$ | $2\pi$ |
| $q_2$ | - | $3\pi/\sqrt{8}$ | $2\pi\sqrt{2}$ | $3\pi/\sqrt{8}$ | $2\pi$ | $2\pi\sqrt{2}$ |
| $q_3$ | - | $2\pi\sqrt{41/32}$ | - | $2\pi\sqrt{41/32}$ | - | $2\pi\sqrt{3}$ |
| $q_4$ | - | - | - | - | - | $4\pi$ |
| $r_1$ | $2\pi$ | $2\pi$ | $2\pi$ | $2\pi$ | $2\pi\sqrt{3/8}$ | $2\pi$ |
| $r_2$ | - | $3\pi/\sqrt{8}$ | $2\pi\sqrt{2}$ | $3\pi/\sqrt{8}$ | - | - |
| $r_3$ | - | $2\pi\sqrt{41/32}$ | - | $2\pi\sqrt{41/32}$ | - | - |
| $\beta$ | 1.3 | 1.0 | 1.0 | 1.0 | 0.8 | 1.3 |
| $\sigma$ | 0.1 | 0.1 | 0.1 | 0.1 | 0.1 | 0.1 |
| $\frac{2\alpha_l}{2l+1}$ | $P_l(\frac{1}{3})$ | $P_l(-\frac{13}{17})$ | $P_l(0)$ | $-P_l(-\frac{13}{17})$ | $P_l(\frac{1}{3}) - P_l(-\frac{1}{3})$ | $-P_l(0)$ |
| $\alpha_0$ | $1/2$ | $1/2$ | $1/2$ | $-1/6^*$ | - | $-1/2$ |
| $\alpha_1$ | $1/2$ | $-39/34$ | - | $39/34$ | 1 | - |
| $\alpha_2$ | $-5/6$ | $545/578$ | $-5/4$ | $-545/578$ | - | $5/4$ |
| $\alpha_3$ | $-77/54$ | $1001/9826$ | - | $-1001/9826$ | $-77/27$ | - |
| $\alpha_4$ | - | $-\frac{241911}{167042}$ | $\frac{27}{16}$ | $\frac{241911}{167042}$ | - | $-27/16$ |
| $\alpha_5$ | - | - | - | - | $11/3$ | - |
| $\alpha_7$ | - | - | - | - | $-605/243$ | - |
| $\alpha_9$ | - | - | - | - | $-\frac{9101}{19683}$ | - |
| $\alpha_{11}$ | - | - | - | - | $\frac{229057}{59049}$ | - |
| $\alpha_{13}$ | - | - | - | - | $-\frac{353807}{59049}$ | - |
| $a_1$ | $\sqrt{3}$ | $2/\sqrt{3}$ | 1 | $2/\sqrt{3}$ | $\sqrt{8}$ | 1 |
| $a_2$ | $\sqrt{3}$ | 2 | 1 | 2 | $\sqrt{8}$ | 1 |
| $a_3$ | $\sqrt{3}$ | $4\sqrt{2}/3$ | 1 | $4\sqrt{2}/3$ | $\sqrt{8}$ | 1 |

APPENDIX B

# Proof that $\mathbf{C^{(lm)}}$ is real

To prove $C^{(lm)}(r, \hat{\mathbf{r}})$ is real, use a plane wave expansion

$$e^{i\boldsymbol{k}\cdot\boldsymbol{r}} = 4\pi \sum_{l=0}^{\infty} \sum_{m=-l}^{l} i^l j_l(kr) Y_{lm}(\hat{\mathbf{k}}) Y_{lm}(\hat{\mathbf{r}}) \tag{B.1}$$

where $j_l$ are the spherical Bessel functions. Consequently,

$$C^{(lm)}(r, \hat{\mathbf{r}}) = \left(\frac{1}{2\pi}\right)^3 (-i)^l \sqrt{\frac{4\pi}{2l+1}} \beta \int R(k) Y_{lm}(\hat{\mathbf{k}}) e^{i\boldsymbol{k}\cdot\boldsymbol{r}} d\boldsymbol{k} \tag{B.2}$$

$$= Y_{lm}(\hat{\mathbf{r}}) \left(\frac{1}{2\pi}\right)^3 \sqrt{\frac{4\pi}{2l+1}} \beta 4\pi \int_0^{\infty} R(k) j_l(kr) k^2 dk \tag{B.3}$$

by orthogonality of spherical harmonics. Eq. B.3 is real since $Y_{lm}$, $R$, and $j_l$ are real.

APPENDIX C

# Connecting displacement to polarization

What is the connection between the displacement, $\delta$, and the polarization? Two approaches are suggested.

## C.1. Electrostatics Method

This method ties the polarization vector to the displacement vector through comparing the electric energy from a macroscopic electric field to the energy from a microscopic electric field. For a macroscopic system,

$$\epsilon_0 \nabla \cdot \boldsymbol{E} = -\nabla \cdot \boldsymbol{p}, \tag{C.1}$$

where $\epsilon_0$ is the vacuum permittivity. If a one-dimensional polarization is considered of the form

$$p_x = p_0 \cos(Qx), \tag{C.2}$$

then

$$E_{\text{macro}} = -p_0 \cos(Qx)/\epsilon_0, \tag{C.3}$$

where $E_x$ is the macroscopic electric field and the divergence free electric field is ignored. The energy density associated with this electric field per period is

$$u_{\text{macro}} = \frac{\epsilon_0}{2}\int_s^{s+\lambda} E_{\text{macro}}^2 dx = \frac{\pi}{2\epsilon_0 Q}p_0^2, \tag{C.4}$$

where $\lambda = 2\pi/Q$.

Now consider the PFC microscopic case. Assume the charge density

$$\rho_e = e(\rho_A - \rho_B) = e\rho_{A0}(n_A - n_B), \tag{C.5}$$

where $\rho_e$ is the charge density and $e$ is the electron charge. Furthermore, consider a charge distribution such that

$$n_A = A\cos(qx) \text{ and } n_B = A\cos(q(x - \pi/q - d)) \text{ and } d = d_0\cos(Qx). \tag{C.6}$$

If $q \gg Q$ and $d_0 \ll a$, Gauss's law

$$\nabla \cdot \boldsymbol{E} = \rho_e/\epsilon_0 \tag{C.7}$$

can be analytically solved for the electric field. If it is assumed that

$$u_{\text{macro}} = \frac{\epsilon_0}{2}\int_s^{s+\lambda}[E_{\text{micro}}(d_0) - E_{\text{micro}}(d_0 = 0)]^2 dx \tag{C.8}$$

then to leading order in $d_0$,

$$|p_0| = Ae\rho_{A0}|d_0|/\sqrt{2}. \tag{C.9}$$

## C.2. Modern Theory of Polarization

An alternative approach is inspired by the Modern Theory of Polarization [**107**]. This approach requires a little more preliminary discussion.

### C.2.1. Circular Mean

Given $N$ real numbers, the mean is typically defined as

$$\bar{x} \equiv \frac{1}{N}\sum_{j=1}^{N} x_j \tag{C.10}$$

in the discrete case and

$$\bar{x} \equiv \frac{1}{a}\int_0^a x\mathcal{P}(x)dx \tag{C.11}$$

in the continuous case, where $\mathcal{P}(x)$, the probability density function for $x$, is nonzero only in the interval $[0, a]$. However, these definitions cause problems when calculating the means of angles. For most purposes, it makes more sense for the mean of 0° and 360° to not be 180°, the result of Eq. (C.10), but rather 0° or 360°. Consequently, the circular mean is defined as

$$\bar{\theta} \equiv \mathrm{Im}\ln\sum_{j=1}^{N} e^{i\theta_j}. \tag{C.12}$$

This equation takes angles, converts them to Cartesian coordinates on the unit circle, calculates the average of these points, and then calculates the angle for that Cartesian

point. In the continuous case,

$$\bar{\theta} = \operatorname{Im} \ln \int_s^{s+2\pi} e^{i\theta} \mathcal{P}(\theta) d\theta, \tag{C.13}$$

where $s$ is any real number. The circular mean is multivalued since angles themselves are not uniquely defined.

### C.2.2. Polarization

The circular mean is useful for calculating means of other periodic fields, not just angles. The dipole moment of a finite system is

$$\boldsymbol{P} = \int_V \boldsymbol{r} \rho_e(\boldsymbol{r}) d\boldsymbol{r} \tag{C.14}$$

where $\boldsymbol{P}$ the dipole moment and $\rho_e$ is the charge density. In a charge system with periodic boundary conditions however, Eq. (C.14) results in a dipole moment per unit cell that depends on the origin. In 1d, this means that if

$$p_{\text{incorrect}} = \frac{1}{a} \int_s^{s+a} x \rho_e(x) dx, \tag{C.15}$$

then the polarization, $p$, is a function of the origin $s$. This $s$ dependence is a result of the lack of periodicity of $x$, and Eq. (C.13) is origin independent on the other hand since $e^{i\theta}$ is periodic.

Although simply substituting the complex exponential for $x$,

$$p_{\text{incorrect}} = \int_s^{s+a} e^{i\frac{2\pi x}{a}} \rho_e(x) dx \tag{C.16}$$

gives an origin independent result, it does not match traditional polarization calculations [**107**]. This is because $\rho_e(x)$ is not a probability density function, so the example of Eq. (C.13) is not being followed. Drawing inspiration from this idea though, in the modern theory of polarization [**88**, **108**] the polarization is defined as

$$p = \frac{e}{2\pi}\mathrm{Im}\ln\int e^{i\frac{2\pi}{a}(\sum_l^N Z_l x_l - \sum_j^M x_j)}|\psi(\boldsymbol{x})|^2 d\boldsymbol{x} \tag{C.17}$$

where $e$ is the electron charge, $N$ is the number of nuclei, $M$ is the number of electrons, $eZ_l$ is the charge of nucleus $l$, $\psi$ is the $(N+M)$-particle wavefunction, and $\boldsymbol{x} = (x_1, \ldots, x_{N+M})$.

In our model, there are positively and negatively charged ions. Thus, we let

$$p = \frac{e}{2\pi}\mathrm{Im}\ln\int_s^{s+a}\int_s^{s+a} e^{iq(x_A - x_B)}|\psi(x_A, x_B)|^2 dx_A dx_B, \tag{C.18}$$

where $A$ is assumed to have positive charge and $B$ negative. It seems reasonable to guess that

$$|\psi(x_A, x_B)|^2 = \mathcal{P}(x_A, x_B) = \frac{\rho_A(x_A)}{a\bar{\rho}_A}\frac{\rho_B(x_B)}{a\bar{\rho}_B} \tag{C.19}$$

since then $\int \mathcal{P}(x_A, x_B)dx_A dx_B = 1$. Thus,

$$p = \frac{e}{2\pi}\mathrm{Im}\ln\int_s^{s+a} e^{iqx_A}\rho_A(x_A)dx_A \int_s^{s+a} e^{-iqx_B}\rho_B(x_B)dx_B. \tag{C.20}$$

### C.2.3. Delta Functions

Let's confirm that Eq. (C.20) gives the correct result in the case of point charges. In this case,

$$\rho_A = \rho_{A0}\delta\Big(x - \frac{a}{4}\Big) \tag{C.21}$$

$$\rho_B = \rho_{B0}\delta\Big(x - \frac{3a}{4} - d\Big), \tag{C.22}$$

so

$$p = e\Big(\frac{1}{2} - \frac{d}{a} + n\Big),\ n \in \mathbb{Z}. \tag{C.23}$$

This is exactly the polarization lattice calculated using conventional methods [**107**]. Choosing the $n = 0$ branch,

$$\Delta p = \Big(\frac{e}{2} - \frac{ed}{a}\Big) - \frac{e}{2} = -\frac{ed}{a}. \tag{C.24}$$

### C.2.4. PFC Polarization

In this case, $\rho_i = \rho_{i0}(n_i + 1)$. If $n_i$ are the same as defined in Eq. (C.6) except $d$ is a constant, then

$$p = \frac{e}{2\pi}\mathrm{Im}\ln\frac{A^2\pi^2}{q^2}e^{2\pi i(-d/a+1/2)}. \tag{C.25}$$

If $A \neq 0$, then

$$\Delta p = -\frac{ed}{a} \tag{C.26}$$

as before. However, if $A = 0$, the polarization is undefined since the $\ln 0$ is undefined. In 2d, each polarization component is defined the same as in 1d, and

$$p_i = \frac{e}{2\pi} \mathrm{Im} \ln \int e^{iqx_{i,A}} \rho_A(\boldsymbol{x}_A) d\boldsymbol{x}_A \int e^{-iqx_{i,B}} \rho_B(\boldsymbol{x}_B) d\boldsymbol{x}_B. \tag{C.27}$$

Using the three mode square approximation,

$$\Delta \boldsymbol{p} = -\frac{e\boldsymbol{d}}{a}, \tag{C.28}$$

unless $A_1 = 0$, in which case the polarization is undefined.

APPENDIX D

# LGD Parameters

| Variable | Expression |
|---|---|
| $\alpha$ | $-2q_1^2\tilde{Q}^2\Big[6\alpha_4A_1^4 - A_1^2(\alpha_2 + 20\alpha_4A_2^2 + 32\alpha_4A_3A_2 - 4\alpha_3A_3 + 40\alpha_4A_3^2) + 2\Big(6\alpha_4A_2^4 + A_2^2(\alpha_2 + 4A_3(4\alpha_3 + 9\alpha_4A_3)) + 2A_3^2(\alpha_2 + 6\alpha_4A_3^2)\Big)\Big]$ |
| $\gamma_{11}$ | $\frac{1}{3}q_1^4\tilde{Q}^4\Big[12\alpha_4A_1^4 - A_1^2\Big(\alpha_2 + 4(11\alpha_4A_2^2 + 32\alpha_4A_3A_2 - 7\alpha_3A_3 + 58\alpha_4A_3^2)\Big) + 2\Big(24\alpha_4A_2^4 + A_2^2(\alpha_2 + 204\alpha_4A_3^2 + 40\alpha_3A_3) + 8A_3^2(\alpha_2 + 12\alpha_4A_3^2)\Big)\Big]$ |
| $\gamma_{12}$ | $4q_1^4\tilde{Q}^4\Big[8\alpha_4A_2^4 + A_2^2(\alpha_2 - 16\alpha_4A_1^2 + 8\alpha_3A_3 + 76\alpha_4A_3^2) + 4A_1^2A_2(\alpha_3 - 6\alpha_4A_3) + 2\alpha_4(A_1^2 - 4A_3^2)^2\Big]$ |
| $\omega_{111}$ | $-\frac{1}{60}q_1^6\tilde{Q}^6\Big[36\alpha_4A_1^4 - A_1^2\Big(\alpha_2 + 4(35\alpha_4A_2^2 + 128\alpha_4A_3A_2 - 31\alpha_3A_3 + 430\alpha_4A_3^2)\Big) + 2\Big(96\alpha_4A_2^4 + A_2^2(\alpha_2 + 4A_3(34\alpha_3 + 399\alpha_4A_3)) + 32A_3^2(\alpha_2 + 36\alpha_4A_3^2)\Big)\Big]$ |
| $\omega_{112}$ | $\frac{1}{3}q_1^4\tilde{Q}^6\Big[12\alpha_4A_1^4 - A_1^2\Big(\alpha_2 + 4(11\alpha_4A_2^2 + 32\alpha_4A_3A_2 - 7\alpha_3A_3 + 58\alpha_4A_3^2)\Big) + 2\Big(24\alpha_4A_2^4 + A_2^2(\alpha_2 + 204\alpha_4A_3^2 + 40\alpha_3A_3) + 8A_3^2(\alpha_2 + 12\alpha_4A_3^2)\Big)\Big]$ |

| | |
|---|---|
| $c_{11}$ | $2\left[\alpha_2 + A_1^2\left(-4\alpha_4 + \frac{b_1 q_1^2}{\sigma_1^2} + 4\right) + A_2^2\left(12\alpha_4 + \frac{b_2 q_1^2}{\sigma_2^2} + 4\right) + 1\right]$ |
| $c_{12}$ | $\frac{2A_2^2 b_2 q_1^2}{\sigma_2^2}$ |
| $c_{44}$ | $2\alpha_2 - 8\alpha_4 A_1^2 + 24\alpha_4 A_2^2 + 24\alpha_4 A_3^2 + \frac{2A_2^2 b_2 q_1^2}{\sigma_2^2} + 8A_1^2 + 8A_2^2 + 8A_3^2 + 2$ |
| $g_{44}$ | $\frac{A_2^2 b_2 q_1^2 \tilde{Q}^2}{\sigma_2^2}$ |
| $g_{12}$ | $\frac{A_2^2 b_2 q_1^2 \tilde{Q}^2}{\sigma_2^2}$ |
| $g_{11}$ | $q_1^2 \tilde{Q}^2\left(\frac{A_1^2 b_1}{\sigma_1^2} + \frac{A_2^2 b_2}{\sigma_2^2} + \frac{A_3^2 b_3}{\sigma_3^2}\right)$ |

APPENDIX E

# Calculating Polarizations

Polarizations were calculated for numerical simulations as follows. First, the maxima of $n_A$ and $n_B$ were calculated by fitting to a quadratic paraboloid, as described in Ref. [**86**]. These maxima were interpreted as the atomic positions. Then for each $B$ atom, the four nearest $A$ atoms were calculated. The displacement vector was defined to be the vector from the centroid of these four $A$ atoms to $B$. Note that under this definition, the polarization vector is still calculated for $B$ atoms located at dislocations, but the results are spurious. This is the origin of the off-colored regions at the dislocations in Fig. 4.10.

APPENDIX F

# Calculating Analytical Models

Both as a method for brainstorming new PFC models and as a method for understanding existing ones, analytical expressions for the free energy are often quite useful. Although the results of these expansions are given in the previous chapters, this section will provide some practical advice for doing these calculations. The crucial fact is that

$$\frac{1}{V}\int_{\text{unit cell}} e^{i\boldsymbol{q}\cdot\boldsymbol{r}}d\boldsymbol{r} = \delta_{\boldsymbol{q},\boldsymbol{0}}. \tag{F.1}$$

if $\boldsymbol{q}$ is a reciprocal lattice vector of the unit cell. Consequently, given an expression like

$$\int_V \left(\sum_j A_j e^{i\boldsymbol{q}_j\cdot\boldsymbol{r}}\right)^m d\boldsymbol{r} \tag{F.2}$$

one only needs to find the number of sums $\boldsymbol{q}_1+...+\boldsymbol{q}_m = 0$ in order to evaluate the integral, since the sum of reciprocal lattice vectors is a reciprocal lattice vector. A slightly more general example is

$$\int_V \sum_j A_j e^{i\boldsymbol{q}_j\cdot\boldsymbol{r}} \sum_k B_k e^{i\boldsymbol{q}_k\cdot\boldsymbol{r}} ... d\boldsymbol{r} \tag{F.3}$$

where the set of vectors $\{\boldsymbol{q}_j\}$, $\{\boldsymbol{q}_k\}$, etc. could be different. However, the method for evaluating the integrals is the same.

Although this reduces the problem of calculating an integral to a combinatorics problem, this problem is often not feasible to solve by hand. Further, a naive computational solution is often too slow. For example, if $m = 3$, a straightforward algorithm is

```
# Simple Solution
# qList_i is the set of {q_j} vectors
count = 0
for q1 in qList_1:
    for q2 in qList_2:
        for q3 in qList_3:
            if q1+q2+q3 == 0:
                count += 1
```

which is often too slow. A brute force vectorized solution in Python for three-dimensional vectors is

```
sums = qList_1[None,None,:,:] + qList_2[None,:,None,:] + qList_3[:,None,None,:]
count = (sums.reshape(-1,qList_1.shape[1])==0).all(1).sum()
```

which is considerably faster. An alternative approach is to utilize the polynomial manipulation tools of Mathematica. This approach is discussed in Appendix A of Ref. [**109**].